Raman Spectroscopy of High Salinity Brines and Ices

Daniel P. Mason*[1] and Megan E. Elwood Madden[1]

[1]School of Geosciences, University of Oklahoma, 100 E Boyd St., Norman, OK, USA

*corresponding author: danmason@unm.edu

Abstract:

Raman spectroscopy is an ideal tool to analyze the geochemistry and mineralogy of heterogenous mixtures of solids, liquid, and gases in situ, while maintaining planetary protection protocols. Here we characterize saturated $CaCl_2$, $MgCl_2$, $MgSO_4$, Na_2SO_4, NaCl, and $NaClO_4$ brines, as well as ultrapure water, and mixed $MgSO_4$-NaCl, $MgSO_4$-$NaClO_4$, Na_2SO_4-NaCl, Na_2SO_4-$NaClO_4$, and NaCl-$NaClO_4$ brines from 200 K to 295 K to determine how changes in temperature affect spectral signatures of planetary analogue brines. The resulting reference dataset can be used to interpret spectra from future samples analyzed in situ on planetary bodies. Sulfate and perchlorate brines produced clear, distinct peaks associated with each polyatomic anion. While chloride brines did not produce anion peaks, subtle changes were observed in the OH-stretching region, suggesting changes to the molecular water vibration states due to complexation. Solid-liquid phase transitions were clearly observed in each of the solutions using both 785 nm (red) and 532 nm (green) excitation lasers, particularly in the OH-stretching region between 3000-4000 cm^{-1} with the 532 nm laser. Differences observed in the spectra of frozen sulfate brines suggest that cooling rates may influence the hydration state and/or crystallinity of the solid magnesium and sodium- sulfate salts. These experiments and the resulting spectral library will allow future researchers to use Raman spectroscopy to look for in situ melting, freezing, evaporation, and deliquescence as well as identify the composition of high salinity brines and their frozen products in a range of planetary environments, including permafrost and recurring slope lineae on Mars, potential ice and salt-rich regolith on asteroids such as Ceres, and ice shells and possible seeps or geysers on icy moons and other bodies.

1. Introduction:

As planetary scientists and astrobiologists continue to explore and investigate Mars, icy moons, and other planetary bodies in search of habitable environments, the widespread presence and potential role of salts in generating and maintaining liquid water at or near the surface has gained increasing interest. While pure water has a triple point at 273 K and 611 Pa, adding salt reduces both the temperature and the vapor pressure necessary to sustain liquid water. Observations of sulfate, chloride, and perchlorate salts on Mars suggest that they may play an important role in generating and maintaining liquid water at or near the surface, since pure liquid water is not stable on the surface of Mars for extended periods of time (Bargery et al. 2011).

While pure liquid water is highly unlikely at the surface of Mars today due to both the cold temperatures (Chevrier and Rivera-Valentin 2012) and low pressures, surface water was likely present on Mars during the Noachian (Bargery et al. 2011), as evidenced by erosional features, including possible paleo-shorelines (Clifford and Parker 2001) that suggest that large portions of the planet were flooded by an ocean (Solomon et al. 2005). Sulfate and chloride deposits from the Hesperian also suggest aqueous activity, while most of the surface water likely remained frozen through much of the Amazonian (Carr and Head 2010). Significant evidence suggests that liquid water at Mars' surface began to disappear at or before the Noachian/Hesperian boundary through evaporation to the atmosphere (with some subsequently lost to space), chemical weathering of soil forming hydrated minerals, and/or freezing to form ice within mid- to high-latitude permafrost or at the poles (Squyres 1984).

While the surface of modern Mars is largely cold and dry, it is possible that Mars has small-scale flows of transient liquid water on its surface today. Indeed, recurring slope lineae (RSL), defined as "narrow dark features that incrementally lengthen down steep low-albedo slopes when temperatures are warm, subsequently fade, and reoccur annually" (Stillman and Grimm 2018) can be found on Martian hillsides that often have a slope greater than 25° (Horne 2018). RSL are transient in nature and recur cyclically-- either over the course of the Martian day or over the course of the year (Stillman et al. 2016). They are often found in the lower and mid-latitudes of Mars, within about 25 degrees of the equator, with some at higher latitudes upwards of 30 -35° (Dundas et al. 2013). Some researchers have proposed that RSL form from dry sediment flows (Edwards and Piqueux 2016; Schmidt et al. 2017), while others suggest that they are formed by groundwater seeps or deliquescence (McEwen et al. 2015; Chevrier and Rivera-Valentin 2012; Horne 2018, Abotalib and Heggy 2019).

If recurring slope lineae are aqueous in origin, they are likely highly saline (Table 2), as salts not only depress the freezing point of water, but can also decrease the evaporation rate, allowing metastable liquid to persist for longer periods of time (Hanley et al. 2012). Perchlorate, sulfate, and chloride salts have all been found by numerous missions to Mars (Massé et al. 2015) and may be indicative of the transient presence of liquid water at various locations (Chevrier and Rivera-Valentin 2012). The *Phoenix* lander, for example, has directly detected perchlorate salts-- and may have even detected liquid brine-- in the higher latitudes of Mars (McEwen et al. 2011; Chevrier et al. 2009). Even with salts depressing the freezing point of water, surface temperatures on Mars are generally low enough to freeze brines, ranging from 130 K to 290 K (Bargery et al. 2011). Therefore, RSL may contain mixtures of salt, liquid brine, and ice.

Liquid water in the outer solar system is also likely exists as high salinity brines, protected from evaporation and freezing by ice crusts on Europa, Enceladus, Titan, and perhaps other icy bodies including Ganymede and Pluto (Sohl et al. 2010). Preliminary evidence of salts and hydrated mineral phases on Ceres (Bland et al. 2016), as well as similar phases in altered chondritic meteorites (Zolensky et al. 1999), suggest brines may also affect the near-surface mineralogy of some asteroids. Therefore, if we "follow the water" on other potentially habitable planetary bodies in our Solar System, including Ceres, Europa, Titan, and Enceladus, we will likely find a high salinity brine. Solutes observed in high salinity brines may provide key clues to determine the geochemical conditions, including habitability of the environments in which they are found, both on Earth and other planets (Hallsworth et al. 2007; Yakimov et al. 2015; Stevenson et al. 2015).

Raman spectroscopy is an ideal tool to investigate heterogenous, multi-phase materials remotely. Raman spectroscopy uses the interaction of light with compounds to identify the composition of materials. When photons interact with molecules, a small percentage of the interactions are inelastic, producing light with a slightly different wavelength than the incident photon. Using a laser as the excitation source allows systematic measurement of this change in wavelength by plotting the number of photons produced with different wavelengths in the form of a Raman spectrum (Edwards et al. 2005; Lohumi et al. 2017). The peaks within the spectra are characteristic of different molecules and phases; therefore, Raman spectroscopy can be used to measure both solutes in solution (McGraw et al. 2018) and phase changes, including different hydration states (Wang et al. 2006).

For example, the spectra of sulfate salts dissolved in water have several notable peaks at low wavenumbers (Figure 1) with an intense peak due to S-O bonds in the sulfate anion observed at 982 cm^{-1}; sodium sulfate also displays minor peaks around 456 cm^{-1}, 613 cm^{-1}, and 1112 cm^{-1} (Figure 1), while magnesium sulfate has peaks at 451 cm^{-1}, 617 cm^{-1}, 1113 cm^{-1} (see Table A1). Similarly, perchlorate brines produce indicative peaks at 461 cm^{-1}, 626 cm^{-1}, and 938 cm^{-1}. The O-H bending peak for water is also clearly observed in all of the liquid brines using both the 532 nm and 785 nm lasers (Wang et al. 2004). Additional water peaks are also present at higher wavenumbers due to O-H stretching, including peaks at ~3210 cm^{-1} and 3420 cm^{-1} (Duričković et al. 2011; Yang et al. 2019) are also clearly observed in spectra produced by a 532 nm green laser source.

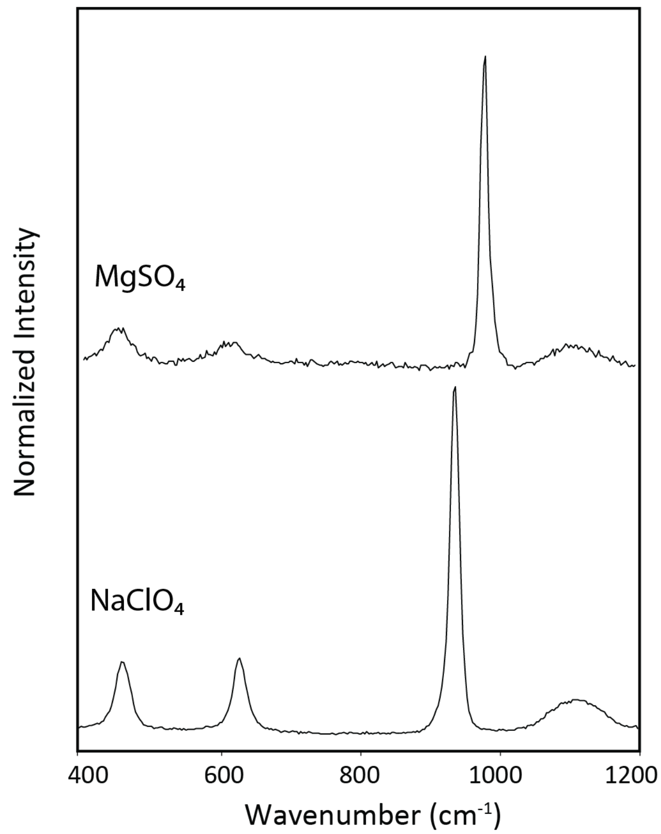

Figure 1: The primary peak for sulfate is observed at 982 cm^{-1}, while the primary peak for perchlorate is observed at 938 cm^{-1}. Secondary peaks are also observed in both sulfate and perchlorate brines as described in the text. Both spectra were collected with a 532 nm excitation source.

This research aims to determine the Raman spectra of sulfate, chloride, and perchlorate brines, frozen brines (ice + salts), and ice-brine mixtures, over a range of Mars-analogue temperatures (200-295 K). Using this technique, we aim to develop a Raman spectral library of ice-brine systems to prepare for upcoming Raman analyses on Mars (Rull et al. 2017; Wiens et al. 2017; Beegle et al. 2015), as well as other planetary bodies including icy moons, asteroids, and comets.

Methods:

Raman spectra were acquired using a Renishaw inVia High Resolution Raman microscope and spectrometer from 200-295 K using a Linkam THMS600 temperature-controlled stage. We used both a 785 nm and a 532 nm laser (45 watts each, Renishaw) at 1% laser power in streamline mode to gather data, using a 50x objective along with a 1200 l/cm grating. We collected data from twelve different solutions: ultrapure water, $CaCl_2$, $MgCl_2$, $MgSO_4$, Na_2SO_4, NaCl, and $NaClO_4$ endmember brines, and $MgSO_4$-NaCl, $MgSO_4$-$NaClO_4$, Na_2SO_4-NaCl, and Na_2SO_4-$NaClO_4$, NaCl-$NaClO_4$ mixed brines. We made the endmember brines by saturating 18MΩ ultrapure water with each reagent grade salt at 295 K. Mixed brines were composed of a 50/50 volumetric mixture of the respective saturated endmember brines. We collected spectra from a 0.4 mL sample of brine placed within a quartz crucible within the Linkam heating/cooling stage. We focused the laser just below the surface of the liquid or focused the laser on the surface of the ice/solids once the brines froze. As we warmed the samples and the ice began to melt, we collected spectra from both liquid and solid areas of the sample, determined by the texture of the surface observed with the optical microscope. In cases when we could not discern the phase(s) present, we used the Raman spectra to characterize the physical state of the sample.

We collected spectra over three different spectral ranges-- an extended scan between 100-4500 cm^{-1}, as well as two static spectra: one focused on low wavenumbers from 100-1000 cm^{-1} (centered at 700 cm^{-1} and for the 785 nm laser, and 1450 cm^{-1} for the 532 nm laser), and one focused on higher wavenumbers from 3000-4000 cm^{-1} (centered between 3250 cm^{-1} and 3450 cm^{-1} for both lasers). Collecting three different scans over the low and high wavenumber regions allowed for increased spectral resolution while also surveying a wide spectral range. While the spectral resolution for both the static and extended scans is theoretically 1 cm^{-1}, there is significantly more noise in the extended scans, making it more difficult to accurately determine peak positions. We collected data with each laser individually. First, we collected all three spectral ranges at 295 K, then lowered the temperature to 200 K at a rate of 100 K/min and proceeded to collect extended spectra from 100-4500 cm^{-1} at 10 K increments until the sample was 5 K below the melting point of the respective solution being tested (Table 2). We then collected extended spectra at 1 K increments until the temperature was ~5 K above the melting point of the solution. During these smaller temperature adjustments around the melting point, the temperature changed at a rate of at least 20 K/min. We warmed the sample from 200 K after complete freezing to reliably observe the melting temperature as liquids may remain metastable even at substantial undercooling (Toner et al. 2014).

Once we collected extended spectra around the melting point, we lowered the temperature back to 200 K to re-freeze the sample and collected a static spectrum from 100-1000 cm^{-1} for 100 seconds and repeated the same temperature path used for the extended spectra. This process was repeated once more to collect static spectra from 3000-4000 cm^{-1}. Finally, we raised the temperature back to 295 K, where we again collected static spectra at both low and high wavenumbers, as well as an extended spectra to see if there were any changes that occurred during the repeated freezing and thawing cycles. The entire process took four to five hours to complete for each laser and solution. We used a new subsample of brine when we changed lasers to minimize possible changes in composition due to evaporation, sublimation, or deliquescence.

We used the WiRE 4.1 software to process and analyze the spectra. We removed cosmic gamma rays using the "zap" function. We also used WiRE to subtract the baseline, by fitting a curve through fixed points at the base of the spectrum and treating it as a fourth order polynomial. We normalized the intensity range from 0 to 1 for each spectrum based on the maximum peak to maintain consistency between all spectra. Curve fits were also completed in WiRE for spectra of interest to determine peak centers, widths, and heights.

2. Results:

Sulfate and perchlorate brines produce easily identifiable, distinct spectra; however, only subtle differences (Figure 2) were observed when we compared spectra collected from the chloride brines with that of ultrapure water (UPW).

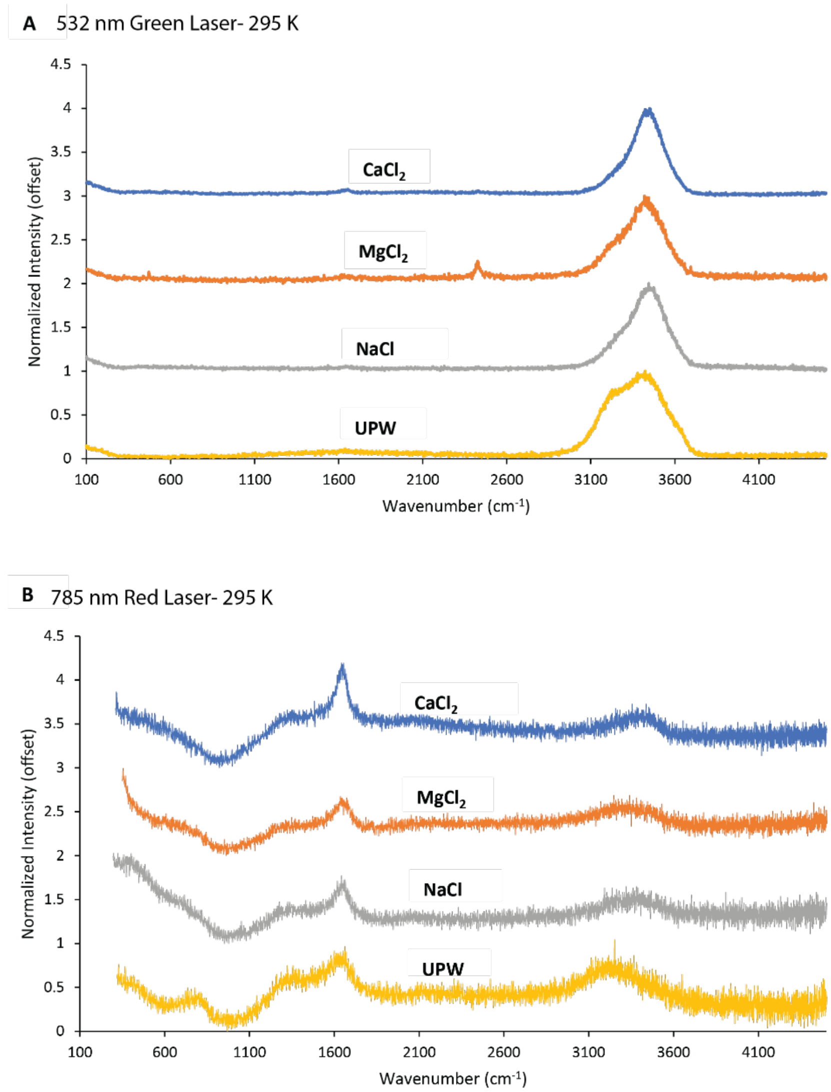

Figure 2: Chloride brines produce spectra similar to ultrapure water when analyzed with either the 532 nm (A) or the 785 nm (B) lasers. However, the addition of salts results in shifts in the OH-stretching peaks observed between 3050 cm^{-1} *and 3450 cm*$^{-1}$ *due to complexation affects. Note: the peak observed around 2400 cm*$^{-1}$ *in the magnesium chloride spectra collected with the 532 nm laser is an artifact of fluorescent lighting and is not indicative of magnesium chloride.*

The 1644 cm^{-1} OH-bending peak in water was observed in spectra collected with both the 532 nm and 785 nm lasers, with peak centers ranging from 1615 cm^{-1} to 1680 cm^{-1} (Table 1), in agreement with values previously derived in the literature (Martinez-Uriartem et al. 2014). However, the OH-stretch bands observed at 3000-3500 cm^{-1} are much more intense than the lower wavenumber OH-bending bands in the spectra collected with the 532 nm laser (Figures 2 and 3). The symmetric OH-stretch peak (Duričković et al. 2011; Yang et al. 2019) shifted to higher wavenumbers in the brines (in some cases by ~50 cm^{-1}) compared to the peak observed in UPW (3204.9 cm^{-1} with the 532 nm laser). Similarly, the peak position of the higher wavenumber asymmetric OH-stretch peak (Duričković et al. 2011) also shifted to higher wavenumbers in the brines (up to 20 cm^{-1}) compared to the peak position observed in UPW (3430.6 cm^{-1} with the 532 nm laser).

Table 1: Curve fits of specific bands/peaks for each of the spectra in Figure 2.

OH-bend Peak 532 nm (~1644 cm^{-1})					**OH-bend Peak 785 nm (~1644 cm^{-1})**				
	Centre	*Width*	*Height*	*Area*		*Centre*	*Width*	*Height*	*Area*
$CaCl_2$, 295 K	1644.7	78.0	0.04	4.62	*$CaCl_2$, 295 K*	1641.3	150.0	0.09	19.06
$MgCl_2$, 295 K	1649.6	163.2	0.03	4.41	*$MgCl_2$, 295 K*	1630.8	187.6	0.06	16.80
NaCl, 295 K	1647.9	81.4	0.02	1.96	*NaCl, 295 K*	1637.5	119.0	0.06	8.96
UPW, 295 K	1682.5	779.1	0.05	37.69	*UPW, 295 K*	1615.0	250.0	0.10	39.15

OH-stretch Peak 532 nm (~3200 cm^{-1})					**OH-stretch Peak 785 nm (~3200 cm^{-1})**				
	Centre	*Width*	*Height*	*Area*		*Centre*	*Width*	*Height*	*Area*
$CaCl_2$, 295 K	3233.1	158.3	0.17	37.14	*$CaCl_2$, 295 K*	3249.9	250.0	0.02	5.49
$MgCl_2$, 295 K	3221.3	203.4	0.26	82.97	*$MgCl_2$, 295 K*	3245.0	250.0	0.04	14.90
NaCl, 295 K	3255.8	189.3	0.21	51.65	*NaCl, 295 K*	3250.0	247.7	0.02	7.23
UPW, 295 K	3204.9	218.0	0.48	139.39	*UPW, 295 K*	3215.0	250.0	0.09	33.70

OH-stretch Peak 532 nm (~3400 cm^{-1})					**OH-stretch Peak 785 nm (~3400 cm^{-1})**				
	Centre	*Width*	*Height*	*Area*		*Centre*	*Width*	*Height*	*Area*
$CaCl_2$, 295 K	3442.1	217.6	0.91	223.87	*$CaCl_2$, 295 K*	3424.3	160.3	0.02	5.18
$MgCl_2$, 295 K	3434.3	247.8	0.80	232.75	*$MgCl_2$, 295 K*	3431.9	258.7	0.07	19.11
NaCl, 295 K	3451.8	227.8	0.91	271.07	*NaCl, 295 K*	3431.9	200.0	0.02	6.39
UPW, 295 K	3430.6	299.0	0.85	269.38	*UPW, 295 K*	3417.3	224.9	0.03	8.90

Both sulfate and perchlorate anions produced prominent peaks observed in the spectra produced by both the 532 nm and 785 nm lasers (Figure 3), as well as several other minor peaks indicative of these two brines. The main sulfate peak is centered at 982 cm^{-1}, while the main perchlorate peak is centered around 938 $\pm$ 2 cm^{-1}. Therefore, polyatomic anions produce distinct Raman peaks at different wavenumbers.

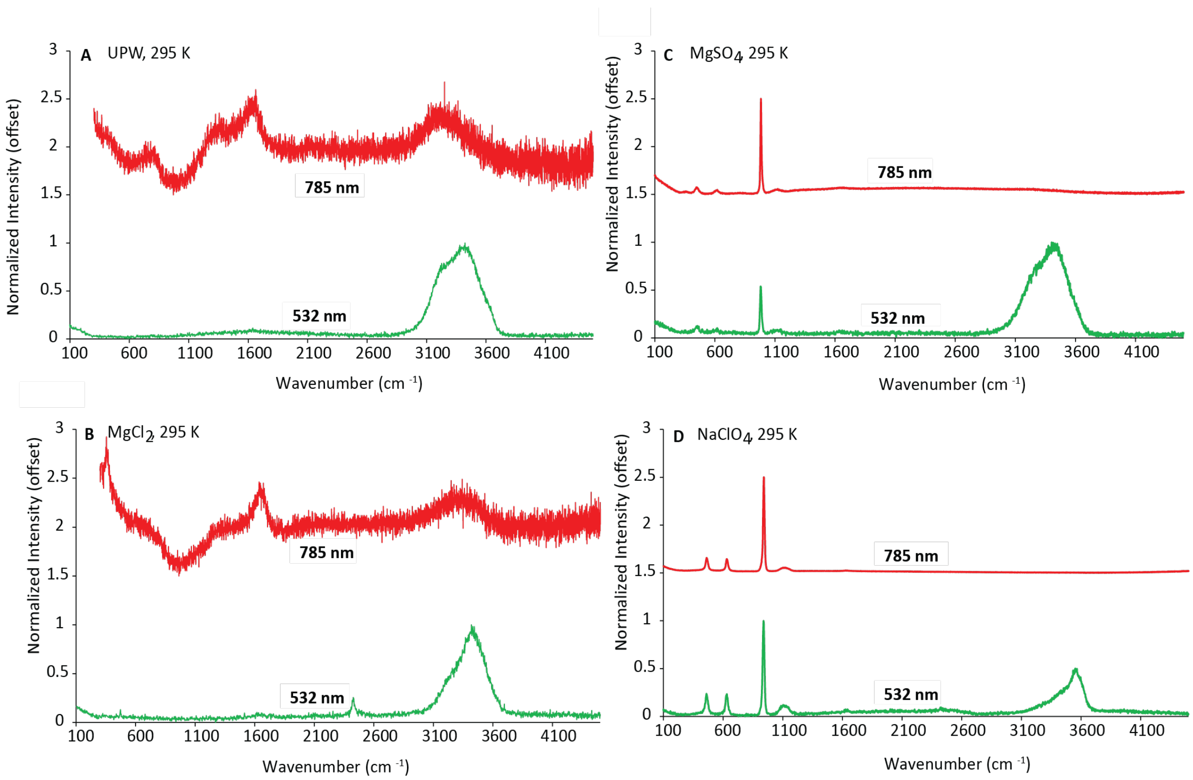

Figure 3: Spectra of A) ultrapure water (UPW), B) $MgCl_2$, C) $MgSO_4$ and D) $NaClO_4$ brines at 295 K with both the 785 nm and 532 nm lasers. Note: the peak observed around 2400 cm^{-1} in the $MgCl_2$ brine spectra collected with the 532 nm laser is an artifact from fluorescent lighting and

is not indicative of the brine. The water peals observed in the UPW and $MgCl_2$ brine spectra collected with the 785nm laser are of relatively low intensity, resulting a noisier signal.

In addition, the location, intensity, and shape of some peaks change distinctly with temperature and may be used to differentiate between liquid brines and ices. The specific peak positions associated with the ice, salts, and liquid solutions are outlined in the appendix in Table A1. As temperatures increased from 200 K the samples melted and we visibly observed the change from a solid to a liquid state using the optical microscope. In most cases, the solutions melted within $\pm$ 2 K of the melting points reported in the literature (Table 2). The two notable exceptions to this are $CaCl_2$ (antarcticite—$CaCl_2$*$6H_2O$), which we observed melting at 219 K (the melting point reported in the literature is 4 K higher, at 223 K) and the mixed $MgSO_4$-NaCl brine, whose constituent endmembers have melting points of 270 K and 250 K, respectively, but whose 50/50 mixture melted at 236 K, similar to-- but still 4 K lower than-- the reported melting temperature for $MgCl_2$ at 240 K (Table 2).

Table 2: Melting Points of Brines

Brine	***Observed Melting T (K) [this study]***	***Eutectic T (K) [from literature]***	***Weight % salt in saturated brine***	***Moles of salt/kg H_2O***
$CaCl_2$	*218-219*	*223[c]*	*30.50*	*3.95*
NaCl-$NaClO_4$	*232-233*	-----	-----	-----
$MgSO_4$-$NaClO_4$	*234*	-----	-----	-----
Na_2SO_4-$NaClO_4$	*235-236*	-----	-----	-----
$NaClO_4$	*235-237*	*238.9[d]*	*52.00*	*8.85*
$MgSO_4$-NaCl	*236-237*	-----	-----	-----
$MgCl_2$	*239-240*	*240.2[d]*	*21.00*	*2.79*

Na_2SO_4-NaCl	*250-251*	*251[c]*	-----	-----
NaCl	*251-252*	*251[c]*	*23.30*	*5.20*
		251.9[d]		
$MgSO_4$	*270-271*	*269[c] ;269.4[d] **	*16.50*	*1.64*
Na_2SO_4	*271-272*	*271[b] ;271.8[b] **	*4.15*	*0.30*
Ultrapure water	*274*	*273.2[a]*	*0.00*	*0.00*

[a]Chevrier and Rivera-Valentin 2012; [b]Lewis et al. 2010; [c]Möhlmann and Thomsen 2011; [d]Toner et al. 2014

**hydrated salt phase present*

3.1 Frozen Brine

The spectra collected at 200 K from all the frozen brines and ultrapure water ice look markedly different from the spectra collected from the corresponding liquids at 295 K, using both the 532 nm and 785 nm lasers. For example, in both the $MgCl_2$ and ultrapure water experiments, distinct peaks appear at low wavenumbers (<800 cm^{-1}) when the temperature is 200 K (Figure 4). While these peaks are much more apparent with the 785 nm laser, they are also present in the spectra collected with the 532 nm laser. A similar change can be observed in the OH-stretching peak observed at ~3200 cm^{-1} collected with the 532 nm laser for each of the brines shown in Figure 5. When each brine is liquid, a broad, asymmetric peak appears at the higher wavenumbers of each spectra. When these brines are frozen into ice, the spectra contains several separate sharp peaks (Figure 5). The spectra produced from both the sodium perchlorate endmember brine and the various sodium perchlorate mixtures includes a very intense peak at ~3600 cm^{-1}, a peak that appears to be unique within frozen perchlorate brine. Numerous peaks are also seen throughout the mid-range wavenumbers (Figure 6) using both the 532 nm and 785 nm lasers, indicative of differences in brine composition, temperature, and excitation wavelengths.

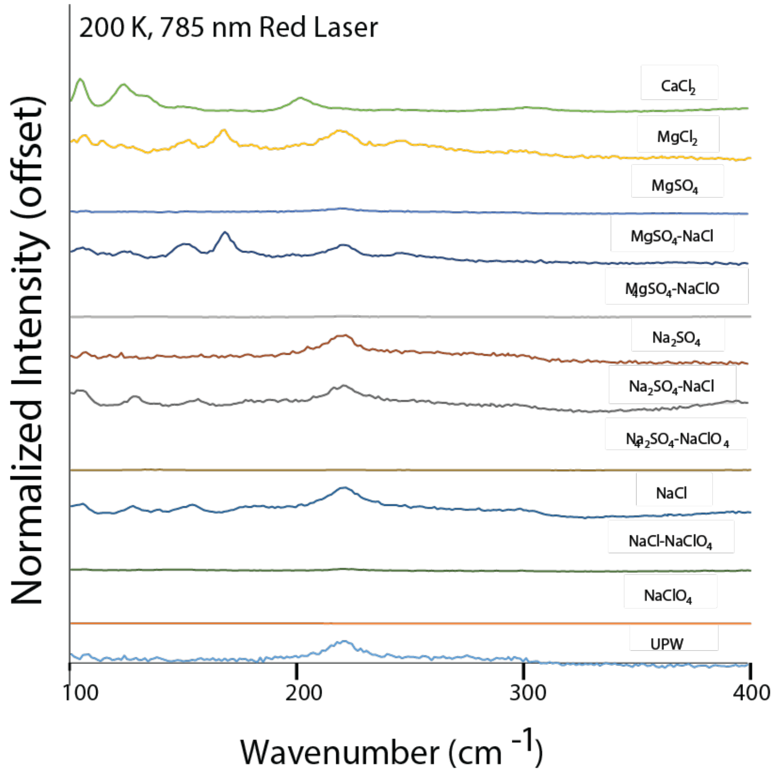

Figure 4: The lower wavenumber range of the extended spectra of all twelve solutions, collected at 200 K using the 785 nm red laser.

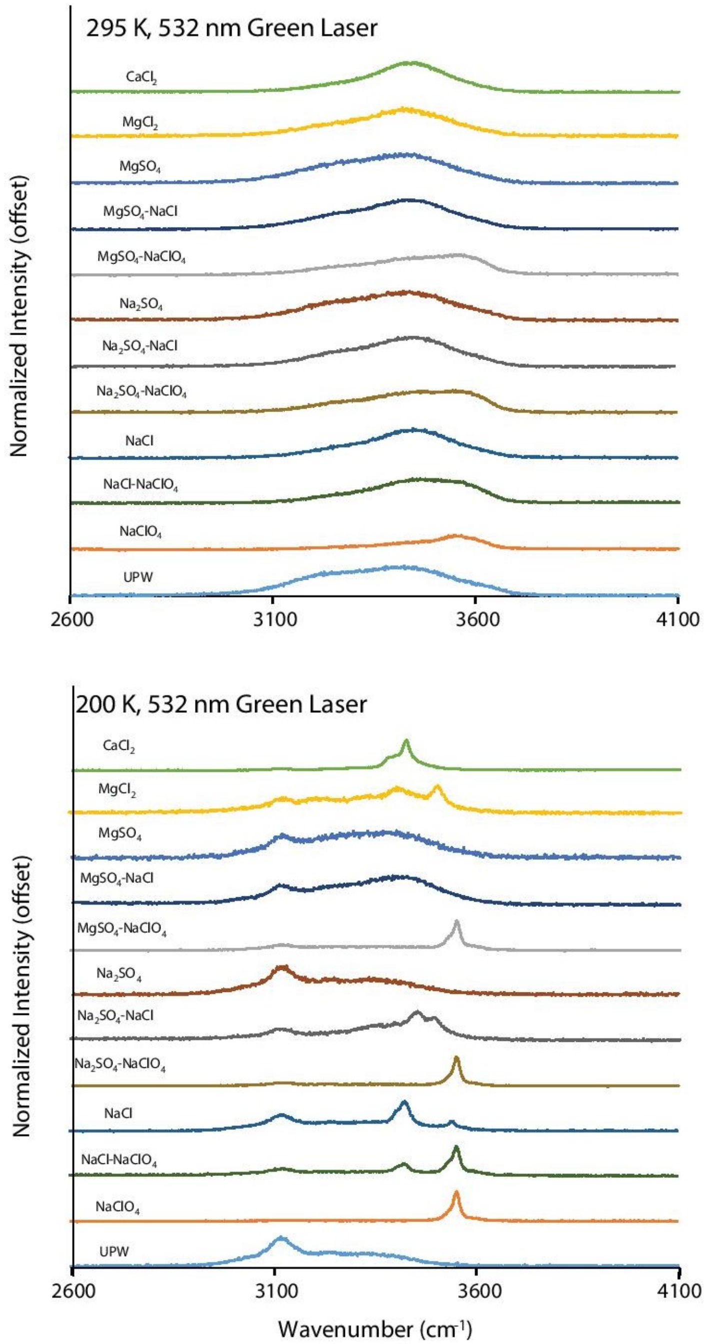

Figure 5: The OH-stretching band range of the extended spectra of all twelve solutions at both 295 K and 200 K, using the 532 nm green laser. Distinct peaks appear when the brines are frozen.

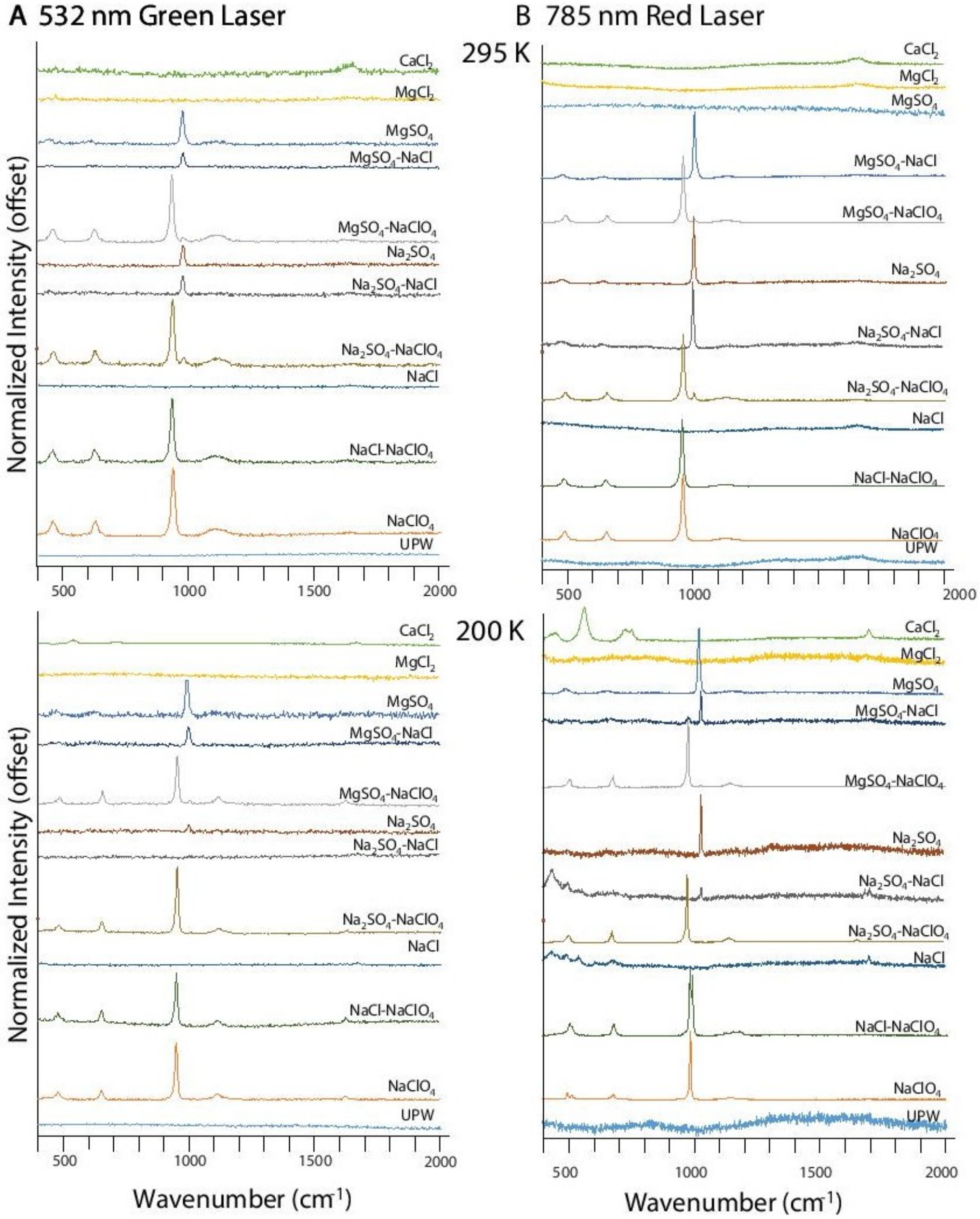

Figure 6: The mid-wavenumber range (400 cm^{-1} to 2000 cm^{-1}) of the extended spectra of all twelve solutions, using both the 532 nm green and 785 nm red lasers at both 295 K and 200 K. Peak positions and intensities vary based on the temperature, composition, and to a lesser extent, excitation wavelength.

3.2 Partial Melting

We observed both solid and liquid present in the sample simultaneously for each of the twelve solutions tested. In some cases, such as $CaCl_2$ (Figures 7A) and $NaClO_4$ (Figure 7B) brines, spectra indicative of both frozen and liquid brine were observed several degrees above the initial melting point.

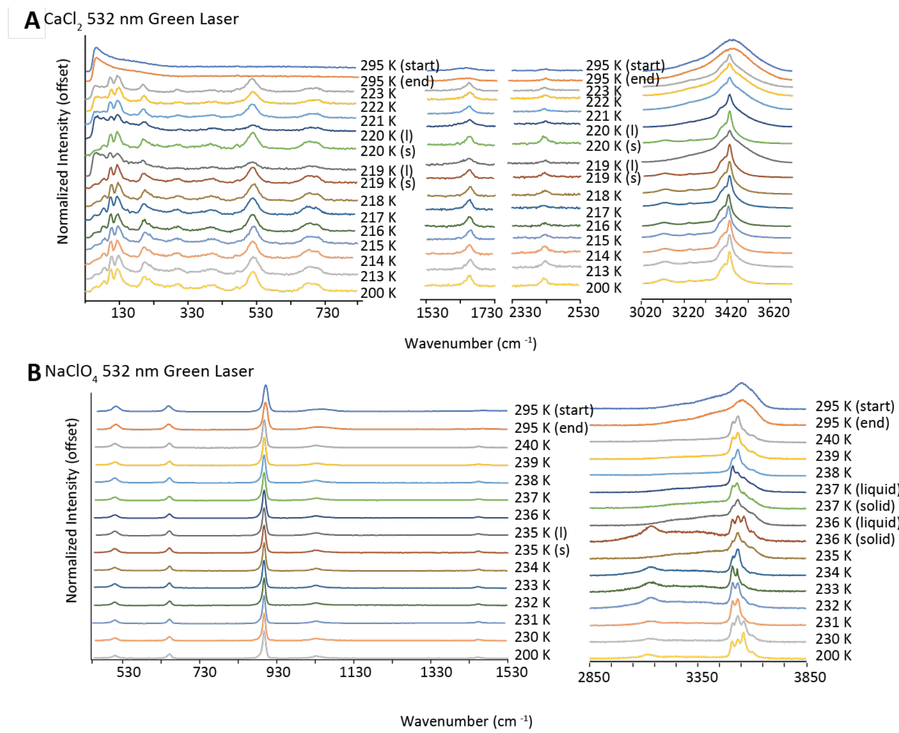

Figure 7: The partial melting of both $CaCl_2*6H_2O$ and $NaClO_4$ can be seen near their respective melting points, with multiple spectra taken at the same temperature.

3.3 Mixed Brines:

We observed clear differences in the shape and position of the OH-stretching band peaks at ~3400 cm^{-1} in the spectra collected from the endmember brines with the 532 nm laser (Figure 8). For example, at 295 K, the peak maximum is observed at 3438 cm^{-1} in saturated endmember $MgSO_4$ brine and 3453 cm^{-1} in saturated endmember NaCl. In the mixed $MgSO_4$-NaCl solution, the peak maximum is observed at an intermediate wavenumber-- 3443 cm^{-1}. This averaging or shifting of peak positions in the ~3400 cm^{-1} OH-stretching band region was also observed in the frozen mixed brines. At 200 K, the OH-stretching peak maximizes at 3370 cm^{-1} in the frozen $MgSO_4$ endmember brine (similar to either epsomite—$MgSO_4$*7H_2O—or meridianiite—$MgSO_4$*11H_2O [Wang et al. 2006, Elif Genceli et al. 2009]), while it maximizes at 3424 cm^{-1} in the frozen NaCl, indicative of hydrohalite—NaCl*2H_2O (Thomas et al. 2017; Baumgartner and Bakker 2010) endmember brine. The peak maximum for the $MgSO_4$-NaCl mixed brine is observed at an intermediary position of 3406 cm^{-1}.

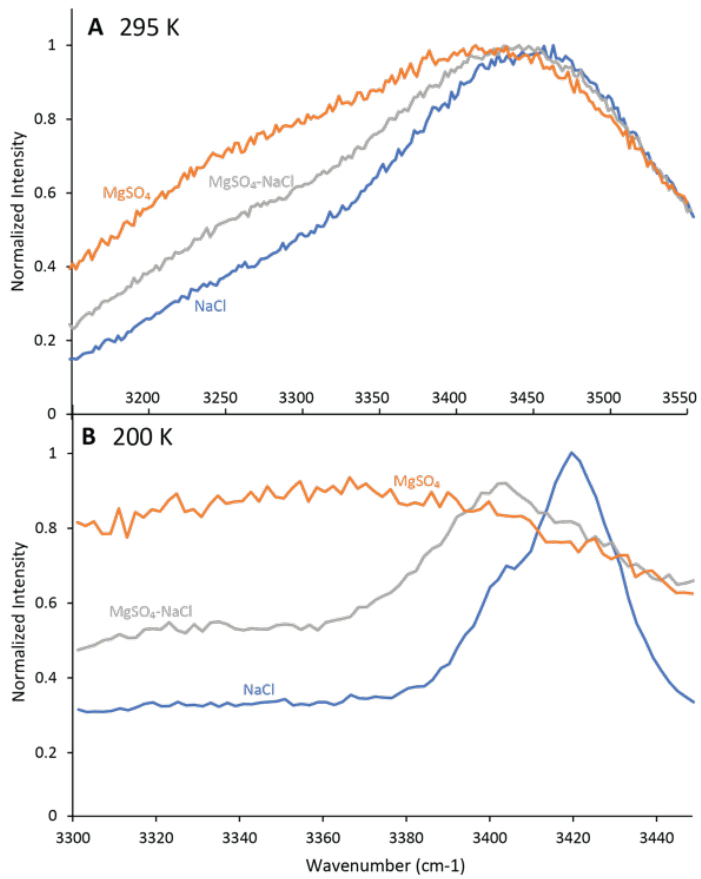

Figure 8: Spectral shifts in the OH-stretching band between $MgSO_4$, NaCl, and $MgSO_4$-NaCl solutions at 295 K (A) and at 200 K (B) observed with the 532 nm laser.

However, a different pattern is observed in mixed sulfate-perchlorate brines (Figures 9A and 9B). Minor sulfate peaks appear at approximately 460 cm^{-1}, 611 cm^{-1}, 1095 cm^{-1} and 1133 cm^{-1} (Wang et al. 2006) when the endmember $MgSO_4$ brine is solid, and at 451 cm^{-1}, 617 cm^{-1}, and 1113 cm^{-1} (Wang et al. 2006) when $MgSO_4$ brine is liquid; minor perchlorate peaks appear at approximately 461 cm^{-1}, 626 cm^{-1}, and 1095 cm^{-1} in the liquid endmember $NaClO_4$ brine (Nebgen et al. 1965). In the experiments where sulfate and perchlorate brines are mixed (Figure 9; Table 3), peaks are observed between 460 cm^{-1} to 465 cm^{-1} and 620 cm^{-1} to 637 cm^{-1}, respectively (regardless of temperature). The peak positions are more consistent with what would be expected of perchlorate peaks than sulfate peaks. The third peak, observed at ~1115 cm^{-1} when the mixed brine is liquid, shifts to ~1100 cm^{-1} when the brine is frozen. This peak shift during freezing is similar to the pattern observed in the endmember sulfate brines and is not observed in the endmember perchlorate brine.

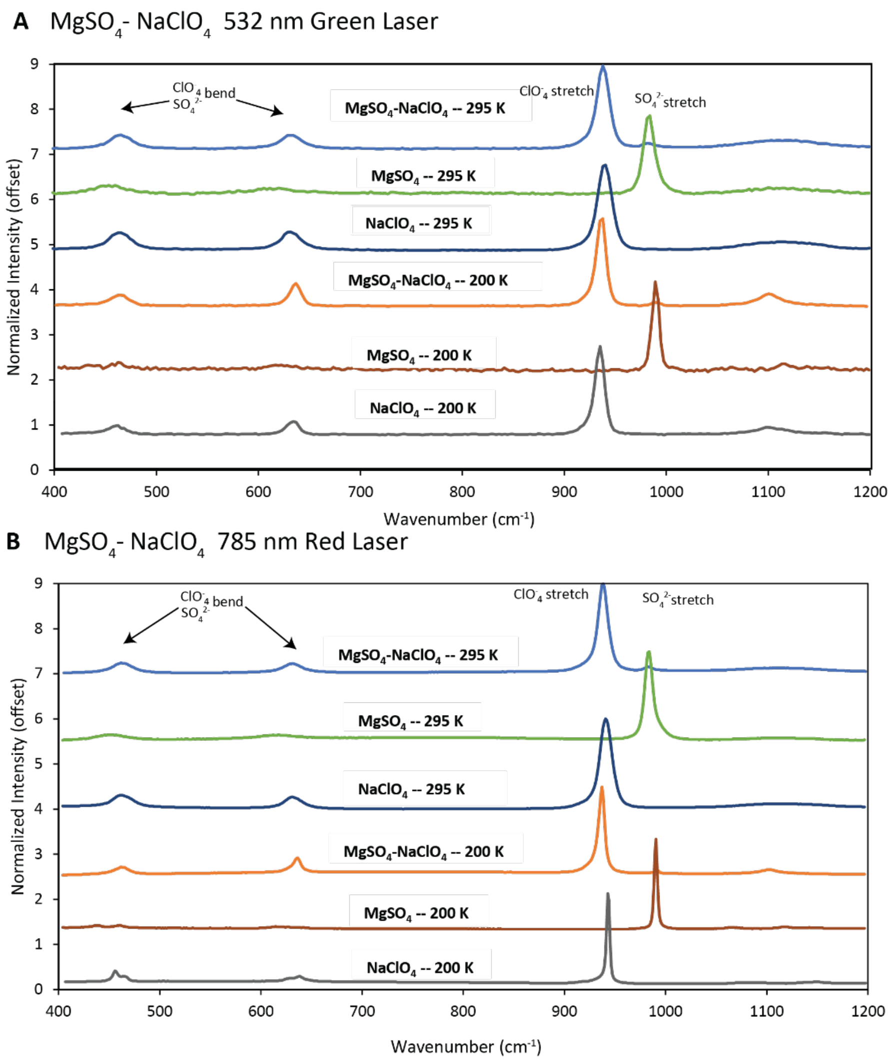

Figure 9: Minor peaks in sulfate-perchlorate mixed brines. While the two lower peaks more closely align with the perchlorate peak positions regardless of temperature, the higher ~1110 cm^{-1} peak is more consistent with sulfate, as it shifts significantly during freezing.

Table 3: 532 nm green and 785 nm red wavelength curve fit data for $MgSO_4$, $MgSO_4$-$NaClO_4$, and $NaClO_4$ spectra between 400 cm^{-1} and 1200 cm^{-1} at both 200 K and 295 K (Figure 9).

		SO_4/ClO_4 bend (~450 cm^{-1}), 532 nm				SO_4/ClO_4 bend (~450 cm^{-1}), 785 nm			
Brine	**T (K)**	*Centre*	*Width*	*Height*	*Area*	*Centre*	*Width*	*Height*	*Area*
$MgSO_4$	200	457.73	0.95	0.69	0.87	437.37	25.37	0.03	1.16
$MgSO_4$	200	--	--	--	--	460.00	16.52	0.02	0.45
$MgSO_4$	295	453.42	40.73	0.08	3.62	451.48	32.22	0.05	2.05
$MgSO_4$-$NaClO_4$	200	464.09	31.55	0.14	6.91	462.53	20.00	0.13	4.24
$MgSO_4$-$NaClO_4$	295	464.59	27.91	0.16	6.42	462.72	32.57	0.11	5.82
$NaClO_4$	200	460.27	20.40	0.09	3.00	456.15	10.02	0.10	1.31
$NaClO_4$	200	--	--	--	--	466.17	14.02	0.06	1.20
$NaClO_4$	295	463.91	26.90	0.20	8.41	462.60	24.21	0.14	5.25
		SO_4/ClO_4 bend (~620 cm^{-1}), 532 nm				**SO_4/ClO_4 bend (~620 cm^{-1}), 785 nm**			
Brine	**T (K)**	*Centre*	*Width*	*Height*	*Area*	*Centre*	*Width*	*Height*	*Area*
$MgSO_4$	200	623.14	28.64	0.04	1.66	620.00	54.12	0.02	1.80
$MgSO_4$	295	615.58	51.84	0.06	4.65	632.36	140.58	0.04	9.29
$MgSO_4$-$NaClO_4$	200	636.15	18.11	0.26	7.39	622.00	20.00	0.09	2.77
$MgSO_4$-$NaClO_4$	200	--	--	--	--	636.84	10.00	0.19	3.04
$MgSO_4$-$NaClO_4$	295	631.91	21.66	0.15	5.24	631.36	40.00	0.10	6.27
$NaClO_4$	200	633.58	15.13	0.14	2.69	629.08	14.69	0.04	0.80
$NaClO_4$	200	--	--	--	--	640.10	22.03	0.05	1.43
$NaClO_4$	295	631.56	22.30	0.21	6.89	631.66	18.32	0.12	3.01
		ClO_4 symmetric stretch (~940 cm^{-1}), 532 nm				**ClO_4 symmetric stretch (~940 cm^{-1}), 785 nm**			
Brine	**T (K)**	*Centre*	*Width*	*Height*	*Area*	*Centre*	*Width*	*Height*	*Area*
$MgSO_4$-$NaClO_4$	200	936.03	11.48	1.03	17.54	936.54	8.65	0.95	12.89
$MgSO_4$-$NaClO_4$	295	937.87	14.51	0.91	17.79	937.99	12.16	1.01	19.20
$NaClO_4$	200	934.61	11.38	0.98	15.15	921.20	14.69	0.02	0.44
$NaClO_4$	200	--	--	--	--	943.90	1.34	1.00	1.76
$NaClO_4$	295	939.52	16.77	0.95	20.40	940.89	14.18	1.00	19.36
		SO_4 symmetric stretch (~990 cm^{-1}), 532 nm				**SO_4 symmetric stretch (~990 cm^{-1}), 785 nm**			
Brine	**T (K)**	*Centre*	*Width*	*Height*	*Area*	*Centre*	*Width*	*Height*	*Area*
$MgSO_4$	200	989.48	8.38	0.98	10.12	990.22	3.71	1.01	5.05
$MgSO_4$	295	983.10	13.17	0.87	15.45	983.46	10.13	0.96	13.09
$MgSO_4$-$NaClO_4$	200	990.91	1.18	0.37	0.63	991.11	15.00	0.08	1.86
$MgSO_4$-$NaClO_4$	295	983.18	8.66	0.03	0.27	984.43	10.00	0.07	1.16
		SO_4/ClO_4 asymmetric stretch (~1100 cm^{-1}), 532 nm				**SO_4/ClO_4 asymmetric stretch (~1100 cm^{-1}), 785 nm**			
Brine	**T (K)**	*Centre*	*Width*	*Height*	*Area*	*Centre*	*Width*	*Height*	*Area*
$MgSO_4$	200	1120.48	42.50	0.05	2.89	1065.34	12.30	0.01	0.27
$MgSO_4$	200	--	--	--	--	1118.42	16.69	0.02	0.41
$MgSO_4$	200	--	--	--	--	1145.00	273.90	0.01	4.48
$MgSO_4$	295	1114.78	79.69	0.05	4.57	1110.19	53.01	0.03	2.54
$MgSO_4$-$NaClO_4$	200	1100.90	35.86	0.16	8.99	1102.46	40.00	0.10	6.33
$MgSO_4$-$NaClO_4$	295	1113.49	66.38	0.07	6.21	1115.38	83.97	0.06	8.56
$NaClO_4$	200	1103.03	41.10	0.08	4.98	1082.11	61.19	0.01	0.97
$NaClO_4$	200	--	--	--	--	1119.80	60.00	0.07	6.31
$NaClO_4$	295	1113.84	78.79	0.08	6.77	1148.21	61.19	0.02	1.85

Mixed brines other than sulfate-perchlorate mixes (Figure 9, Figure 10A) also show distinct changes between their solid and liquid forms. For example, mixed brine behavior is observed in the sulfate-chloride brine mix (Figure 10B). The spectra collected from solid $MgSO_4$

brine at 200 K contains an OH-stretch band that maximizes around 3100 cm^{-1} when solid and a second OH-stretch band that maximizes around 3400 cm^{-1}. The solid NaCl (200 K) displays the same 3100 cm^{-1} OH-stretch band observed in the liquid, but it also contains a sharp peak just past 3400 cm^{-1}, as well as a smaller peak around 3550 cm^{-1}. Peaks similar to both endmembers are observed in the sulfate-chloride mixed brine, which-- in addition to showcasing the 3100 cm^{-1} peak found in both spectra—contains a peak around 3400 cm^{-1} (similar to the chloride) and a sharp peak at 3550 cm^{-1}, again similar to the chloride. The mixed brine is a combination of its two respective endmembers and components of both endmember compositions are observed to occur simultaneously in the mixed brine's spectra.

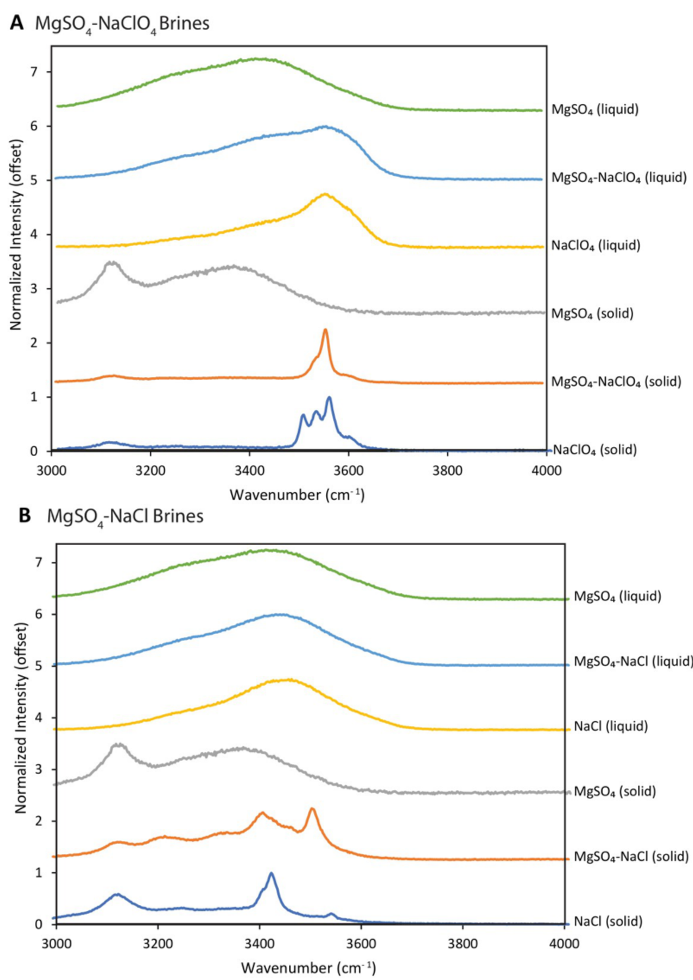

Figure 10: A comparison of spectra collected from both the solid and liquid phases of the $MgSO_4$-$NaClO_4$ (A) and the $MgSO_4$-NaCl (B) mixed brines using the 532 nm laser. The spectra of the mixed brines appear to be intermediary between the spectra of the endmember brines that contain just one solute.

3.4 Freezing Rates and Sulfate Peak Shift:

Differences in peak position between the frozen brine spectra were also observed when the brines were cooled at different rates. In the liquid brines, the sulfate peak is reliably observed at 982 cm^{-1}. When solid, the position of the peak shifts to higher wavenumbers. However, the exact position of the peak varies depending upon the rate of cooling (Figure 11A). Slower cooling rates (10 K/min and 5 K/min) resulted in greater peak shift during freezing, with the sulfate peak observed around 990 cm^{-1} in the frozen brine. More rapid cooling (100 K/min and 20 K/min) resulted in a smaller peak shift, with the sulfate peak in the frozen brine observed around 987 cm^{-1}. Within this bimodal distribution, slight shifts in the exact peak position are also apparent between samples (Figure 11B) cooled at the same rate. For example, $MgSO_4$ cooled at 100 K/min exhibited sulfate peaks at 985 cm^{-1}, 987 cm^{-1}, and 989 cm^{-1}, depending on the sample being tested.

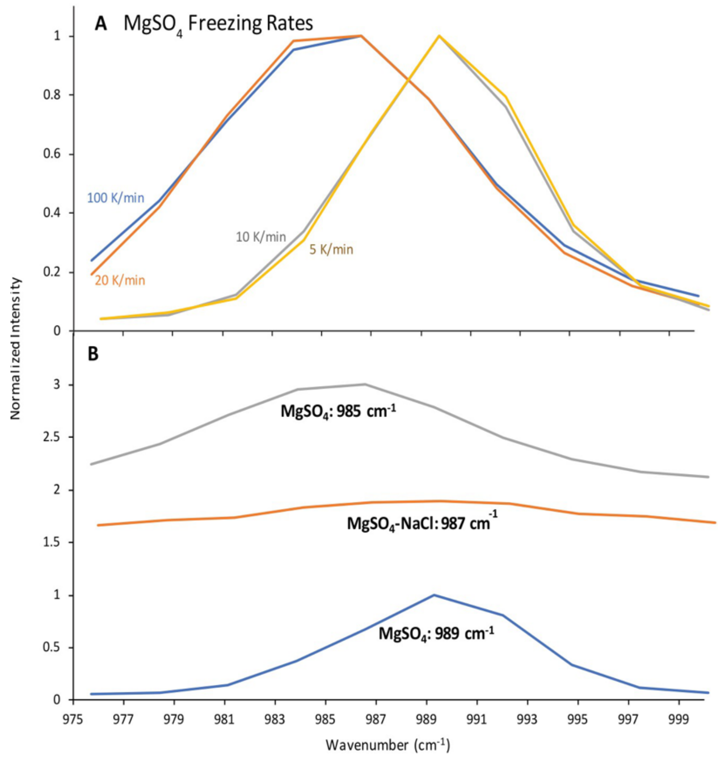

Figure 11: Peak position of the main sulfate peak in $MgSO_4$ brine using the 532 nm laser at 200 K can show A) a bimodal distribution of peak position with different freezing rates B) a slight shift in the sulfate peak position between various samples of frozen $MgSO_4$ brine at 200K after being cooled at a rate of 100 K/min.

3.5 Phase Change and Perchlorate Peak Shift:

The main perchlorate peak (938 cm^{-1}) also appears to shift slightly to higher wavenumbers during melting but returns to the lower wavenumber peak position at temperatures greater than 260 K (Figure 12). Both the 785 nm and 532 nm lasers showcased a repeatable shift in the perchlorate peak position of between 1 cm^{-1} and 3 cm^{-1}. For both lasers, this shift towards higher wavenumbers first occurred between 230 K and 235 K ($NaClO_4$ melting point: 235 K to 237 K

[Table 2]) as the sample was warming, and continued until 255 K to 260 K, whereupon the peak position shifted back down to slightly lower wavenumbers again. This trend was only observed during warming; the position of the perchlorate peak appears to be constant during cooling.

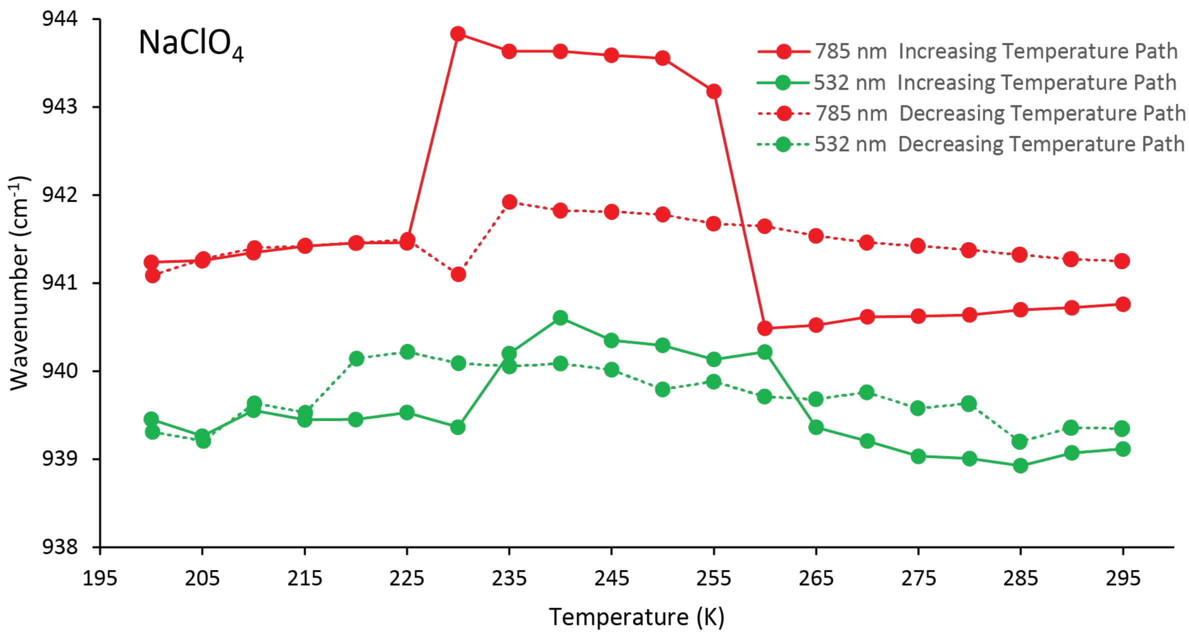

Figure 12: Peak position of the main perchlorate peak in $NaClO_4$ brine during both freezing and melting. The peak shifts position as the phase changes from solid to liquid during melting. This shift is noticeable with both lasers and lasts for approximately 20 K. This same trend does not occur during freezing.

3. Discussion:

Distinct peaks were observed in each spectra, with both the 532 nm and 785 nm lasers. Some differences were observed between the spectra due to the excitation wavelength of the laser (White, 2009). Certain materials are therefore best observed using a 785 nm excitation wavelength due to fluorescence, while others are better observed with a 532 nm due to increased excitation energy due to the inverse relationship between excitation wavelength and peak intensity (Harris et al. 2015; White, 2009). In our experiments, the 532 nm laser generally provided a greater number of identifiable peaks and a less noisy spectra, likely due to its higher frequency and greater excitation energy. In addition, the OH stretching peaks were also clearly observed between 3000 cm^{-1} and 3500 cm^{-1} in the spectra produced with the 532 nm laser, while OH-stretching bands produced by 785 nm excitation are observed at much higher wavenumbers and therefore require a much wider spectral range than employed in this study (White, 2009). However, if brines are observed in the presence of organic materials, a 785 nm or larger wavelength may be needed to decrease fluorescence (Wei et al. 2015).

While distinct peaks indicative of anion chemistry were observed in the sulfate and perchlorate brines, no additional distinct peaks were observed in the chloride brines due to the lack of covalent bonds. However, subtle differences were observed in the spectra, particularly in the area near the OH-stretching region in spectra collected with the 532 nm laser (Figure 5). This suggests that sulfate and perchlorate brines can be readily identified through Raman analyses. Liquid chloride brines may be more difficult to discern. However, if freezing/melting is observed, the composition of the brine could be estimated based on the melting temperature and shifts in the spectra based on the mineralogy of the solid phase (Table 2).

As the brines melt or freeze, the spectra change significantly during the shift between solid ice to liquid brine. This is due both to the differing vibrations of the O-H bonds present in both solid ice and liquid brine (Duričković et al. 2011) as a result of lower energy, as well as to the continued presence of hydrogen bonding as the samples solidify into ice (Duričković et al. 2011), resulting in a decrease of the asymmetric stretching of bonds. However, not all peaks change during melting (see Table A1). While some, such as the main sulfate peak (Figure 11) have notable shifts due to changes in temperature and freezing rate and others-- such as the

~3120 cm^{-1} to 3150 cm^{-1} peak in water ice-- appear much more intense when the sample is solid versus liquid, many other peaks either shift only very slightly or not at all because of changes in temperature. For example, the minor sulfate peaks of both sodium and magnesium sulfates shift <10 cm^{-1}, and in many cases <5 cm^{-1}, during melting (Tables A6 through A9).

The presence of different cations also did not influence the spectral signature of the liquid brines when the anions were held constant. A prime example of this are the magnesium and sodium sulfate brines (Figure 6A). Despite the difference in cation chemistry, their spectra are nearly identical. Experiments from Fischer 2016 further validate this, as calcium perchlorate shows an almost identical Raman peak at 936 cm^{-1} to that of the sodium perchlorate we tested, despite being composed of a different cation. Results from Nuding et al. 2014 further demonstrate that the Raman peaks associated with calcium perchlorate are very similar to their sodium perchlorate counterparts. Similar to calcium perchlorate, magnesium perchlorate hexahydrate (Nikolakolas and Whiteway 2015; Primm et al. 2018) again produces almost identical peaks to that of sodium perchlorate at both low and high wavenumbers, despite being composed of a different cation.

Conversely, differences in anion composition result in significantly different spectra. For example, spectra of NaCl or $MgCl_2$, while similar to one another, are nonetheless markedly different than their respective sodium- or magnesium- sulfate counterparts. This holds true when data is gathered with either the 532 nm or the 785 nm laser at 295 K. While differences in spectra collected from brines with different cation chemistry were not observed in the 200 K sulfate brine data, slight changes in a few unique low wavenumber peaks were observed in the spectra of the chloride brines at 200 K using both lasers, likely due to the formation of new minerals including bischofite ($MgCl_2$*6H_2O) or hydrohalite (NaCl*2H_2O). Therefore, cations do not greatly affect the overall Raman spectra of liquid samples, but differences can arise due to the formation of different minerals as the brines freeze.

We also observed mixtures of solid and liquid at temperatures well above the freezing point, providing clear visual and spectral evidence of partial melting (Figure 7). Therefore, in addition to providing clues regarding the composition and salinity of the aqueous solutions formed via melting, Raman analyses carried out in situ on Mars could distinguish between liquid and frozen brines and could provide key information about past or present hydrologic processes, the extent of aqueous alteration, and/or the potential for habitability. In a similar manner, inclusions of liquid brine in an ice matrix at temperatures below the freezing point could also be characterized (Elif Genceli et al. 2007).

Most of the brines melted at or near the melting/freezing temperatures reported in the literature. However, antarcticite was observed melting 4 K below the melting point reported in the literature (Table 2). This may be due to microscopic pockets of metastable brine that stay liquid despite significant undercooling, allowing liquid to remain in the sample and expand during warming (Samson et al. 2003). However, such brine inclusions would have survived significant undercooling as we first lowered the temperature to 200 K, then collected spectra as the sample warmed in order to avoid such liquid metastability. Alternatively, there may also be subtle phase changes that occur below the melting point that give the visual impression of melting (Samson et al. 2003).

The frozen endmember brines also produced distinct spectra that were interpreted based on data available in the literature (Table A1). However, the spectra produced by the mixed brines are more complicated to interpret, as their spectra typically appear as either an additive mix of the spectra of their two endmember compositions or as an average of the two endmember spectra, where peaks shift to intermediate values. For example, the OH-stretching peak observed in the mixed $MgSO_4$-NaCl brine (Figure 8) maximizes at 3443 cm^{-1} when the brine is liquid, and 3406 cm^{-1} when the brine is solid. This is likely due to the formation of $MgCl_2$ complexes within the $MgSO_4$-NaCl mixed brine, as the ~3400 cm^{-1} peak of the mixed brine is at an almost identical location and is of a very similar intensity to the ~3400 cm^{-1} peak of the $MgCl_2$ endmember brine, both when the samples are liquid and solid.

Peak intensity is also variable within the mixed brines. In general, perchlorate peaks are more intense than sulfate peaks, as can be seen when comparing the main 938 cm^{-1} perchlorate peak with the main sulfate peak at 982 cm^{-1} (Figure 9). This may lead to signals from perchlorate anions overshadowing the signals from sulfate anions in mixed brines. For example, in the $MgSO_4$-$NaClO_4$ mixed brine, the ~460 cm^{-1} and ~620 cm^{-1} peaks (Figure 9) that are consistent with perchlorate are the only minor peaks that can be easily observed in this region, despite two sulfate peaks that also occur in this portion of the spectra in the $MgSO_4$ endmember brine. This is likely due the perchlorate peaks being more intense than the sulfate peaks and overshadowing the minor sulfate peaks.

However, the relative intensity of the peaks produced by the different anions does not explain the ~1110 cm^{-1} peak, which appears to shift from 1100 cm^{-1} when solid to 1115 cm^{-1} as the temperature rises and the brine melts. Both sulfate and perchlorate brines display peaks around 1100 cm^{-1} when solid, according to the literature (Wang et al. 2006; Nebgen et al.1965; see Table A1). Therefore, this shift might be due to the change in sulfate peak position due to freezing, as observed in the sulfate endmember brines.

This peak shift during melting/freezing was observed in all the sulfate-bearing brines, but the magnitude of the shift appears to vary with freezing rate (Figure 11), with a larger shift observed when the temperate decreases at a slower rate. The slightly different peak positions observed at different freezing rates may be due to different hydration states of the solid magnesium and sodium sulfate minerals that form (Ben Mabrouk et al. 2013; Wang et al. 2006; Elif Genceli et al. 2009) including meridianiite ($MgSO_4*11H_2O$, peak around 984-990 cm^{-1}), epsomite ($MgSO_4*7H_2O$, peak around 984cm^{-1}), and mirabilite ($Na_2SO_4*10H_2O$, peak around 988-990 cm^{-1}), as minerals with different hydration states have slightly different sulfate peak positions. Alternatively, the shift in peak position could be due to the formation of amorphous magnesium sulfate (Vaniman et al., 2004; Wang et al. 2006) in experiments with fast cooling rates. Therefore, the shift in peak position with cooling rate could be due to a change in the hydration state or crystallinity, with faster rates of temperature change fostering higher hydration states or amorphous phases with peaks at lower wavenumbers. Faster cooling rates could prevent crystals from nucleating or may cause numerous small crystals to nucleate at several locations within the sample, fostering largely heterogenous nucleation of the brine as it turns to ice (Zhang and Liu 2018; Cook and Hartel 2010). This increase in nucleation sites would allow the remaining water molecules more locations to bind with the sulfate, possibly leading to minerals with higher hydration states. Finally, the trend in sulfate peak position with cooling rate may also be due spatial variations in the mineralogy of the sample. We did not gather spectra from multiple locations of the same sample if the brine was completely frozen. However, small shifts in the sulfate peak position were observed when different subsamples were analyzed (985 cm^{-1} to 989 cm^{-1}) with the same cooling rate (Figure 11B). The shift in peak position could also be due to a systematic variation in the spectra produced by meridianiite whose peaks are reported around 984 cm^{-1} (Wang et al. 2006) to 990 cm^{-1} (Elif Genceli et al. 2007; Elif Genceli et al. 2009).

Interestingly, while we noted significant shifts in the sulfate peak position during freezing, we did not observe a similar magnitude of shift in the perchlorate peak position during freezing. Instead, the main perchlorate peak remains relatively fixed at approximately 938 cm^{-1}, regardless of the phase of the sample. This suggests that perchlorate anions do not interact as strongly with surrounding molecules, making them more immune to phase changes in the surrounding solution. Conversely, the shift in the sulfate peak suggests that sulfate ions are more strongly influenced by the surrounding water molecules in the hydration shell that forms in liquid aqueous solutions, making the sulfate spectra more sensitive to phase changes in the solution, as has also been observed in the Raman spectra of ion hydration shells (Wang et al. 2016).

However, a slight shift in peak position was observed in perchlorate samples during warming (Figure 12). This correlates to the shift in hydration state of sodium perchlorate from a mono- to di-hydrate form that occurs within this temperature range (Chevrier et al. 2009). Other hydration states are present but would not exist at Mars-relevant temperatures. The perchlorate Raman peak shifts to lower wavenumbers as the hydration state increases (Wu et al. 2016) due to differences in hydrogen bonding.

4.1 Implications for Mars:

We have demonstrated that Raman spectrometry can be an effective tool for identifying the composition of both liquid and frozen Mars analogue brines and that the technique can be used to monitor melting and freezing processes in situ. In addition, Raman spectrometry also has several other benefits for planetary exploration, as it does not require that a sample be crushed, pressed, mixed, or otherwise prepared before analysis (Chou and Wang 2017). Raman spectrometry can also analyze heterogenous samples quickly and without direct instrument contact with the sample, preventing instrument or sample contamination and maintaining planetary protection protocols. Therefore, Raman spectrometry would be an ideal technique to analyze permafrost, ices, brines, or RSL in situ on Mars, as it could determine the composition of the sample nondestructively at a distance. For example, the Mars 2020 mission will study the geology of Jezero Crater and look for potential biosignatures. The Raman spectrometer portion of the SuperCam instrument will collect Raman spectra while positioned several meters away from its target with both 1064 nm and 532 nm lasers (Wiens et al. 2017; Harris et al. 2015). The ExoMars mission, developed by the European Space Agency, will also work to determine the past or present habitability of Mars (Bost et al. 2015) as well as to determine local Martian mineralogy using a Raman instrument with a 532 nm laser (Moral et al. 2018; Rull et al. 2017). Other studies (Harris et al. 2015) have suggested that future missions include a 785 nm laser to tease out the most pertinent data from select elements and compounds on the Martian surface.

The addition of Raman spectrometers to rover instrument suites will allow both missions to analyze rocks and sediments, as well as any potential ice, salts, brines, or other mixed phases observed near the landing site. The ability to clearly identify the molecular composition of liquids or solids, including potential salts, will significantly expand our understanding of aqueous and permafrost processes on Mars-- including the modern water cycle. For example, the composition of the putative liquid observed on the *Phoenix* lander strut is still debated (Chevrier et al. 2009; McEwen et al. 2011). Had a Raman spectrometer been present on the lander, it would have been able to analyze the droplets as well as the ices that were uncovered during trenching (Rennó et al. 2009; Martínez and Renno 2013) to provide definitive spectral evidence of liquid water at the surface.

While these experiments demonstrate the utility of using Raman spectroscopy to analyze ices and brines on Mars and other planetary systems, additional variables not addressed in this study may influence Raman analyses on Mars. For example, differences in humidity (water vapor pressure) will influence the formative conditions of each brine, as well as hydrated salts that form via freezing or evaporation. Certain salts—such as epsomite—are more stable at higher relative humidity when more water is available (Vaniman et al. 2004), whereas other salts—such as kieserite or amorphous magnesium sulfate—are more stable at lower relative humidity (Wang et al. 2006).

While we did not investigate deliquescence directly in this study, models have suggested it may become humid enough to form brines through deliquescence at higher latitudes on Mars (Möhlmann and Thomsen 2011). An increase in humidity causes salts to become more hydrated (Wang et al. 2006; Chevrier et al. 2009), forming liquid brine from salt + water vapor. The Raman spectra of liquid water, even in high salinity brines, is unique, allowing planetary scientists to detect thin films of water forming as salts and soils adsorb water from the atmosphere (Boxe et al. 2012; Heinz et al. 2016). Similarly, this work did not directly investigate brine evaporation, which may also occur on Mars when temperatures exceed the melting point. However, previous studies have shown that evaporation rates observed in near-saturated Mars-analogue brines are much slower than those observed for liquid water at similar temperature and humidity conditions (Toner et al. 2014). Therefore, brines may persist as metastable liquids for extended periods of time when the temperature exceeds the triple point, even when the vapor pressure remains below the level needed for thermodynamic stability (Toner et al. 2014). Therefore, Raman analyses could prove useful for testing the multiple working hypotheses for RSL formation. For example, Raman analyses showing deliquescence during day-night or seasonal cycles would strongly support the deliquescence hypothesis, while the presence of sustained liquid would support the seep hypothesis. Anion chemistry in liquids observed at the surface can also provide clues as to the liquid source, as perchlorate salts are more likely to form at the surface due to photolytic reactions (Rao et al. 2012), while chlorides, sulfates, and bromides may be present both at the surface and at depth.

4.2 Implications for other planetary bodies

Results from this study could also be applied to future Raman studies of surface materials on icy moons including Europa, Enceladus, and Titan, as well as ice-rich asteroids and comets. Raman spectroscopy has also been shown to be an effective tool to determine both the presence of brines and the solubility of gasses in brines at Europa-relevant conditions (Bonales et al. 2014). Therefore, Raman spectroscopy could be an important tool for studying both ices and salts, as well as liquid seeps or geysers on the surface of Europa or Enceladus. Similarly, Raman spectroscopy could also be used to analyze near-surface materials including clathrates, ices, and brines in order to investigate possible cryovolcanism on Titan (Fortes et al. 2007).

4. Conclusions:

Our research demonstrates that Raman spectroscopy can accurately detect melting and freezing processes in brines, as well as discern brines with different chemical compositions as the peak locations and intensities present change depending upon the phase and chemical composition of the sample. Raman spectroscopy can also identify partial melting in brines, including calcium chloride and sodium perchlorate. While unique spectra were observed with both the 532 nm and 785 nm excitation sources, the 532 nm laser produced spectra with OH-stretching peaks within the spectral range observed, that proved useful for discerning melting/freezing, and showed subtle changes with the addition of chloride salts. Therefore, the

532 nm later is likely more useful for studying high salinity brines and their frozen products in planetary systems.

Brines containing a mix of two saturated endmembers were shown to have characteristics generally associated with each individual brine and in some cases produced intermediary peaks. Freezing rate may also affect anion peak positions, especially in sulfate brines. These findings are important for planetary geochemistry and planetary science, as they help to shed light on processes that may be occurring on Mars or other bodies where ices and brines are thought to be present. Gaining a more thorough understanding of how these brines behave under certain conditions therefore gives scientists deeper knowledge of planetary processes overall, pertaining not only to Martian processes like recurring slope lineae, but also to geysers, seeps, and other ice-brine interactions throughout the Solar System.

Data Availability: The data gathered during this research will be accessible as part of the Planetary Data System (PDS), hosted by Washington University in St. Louis, MO. Summary spectra and tables are also available in the supplementary materials.

Acknowledgements: This project was funded by NASA PDART grant 80NSSC18K0512. We appreciate early document reviews from K. Dee and S. Dulin. We thank both A. Rodriguez for his help with brine synthesis and development of Raman instrumentation protocols and N. Wood for his help in data processing. We would also like to thank the three anonymous reviewers and the Editor, Will Grundy, for providing constructive feedback that helped us improve this manuscript during the revision process.

Works Cited:

Abotalib, A. Z. and Heggy, E. (2019) ‘A deep groundwater origin for recurring slope lineae on Mars’, *Nature Geoscience*. Springer US, 12(4), pp. 235–241. doi: 10.1038/s41561-019-0327-5.

Bargery, A. S. *et al.* (2011) ‘A background to Mars exploration and research’, *Geological Society Special Publication*, 356, pp. 5–20. doi: 10.1144/SP356.2.

Baumgartner, M. and Bakker, R. J. (2010) ‘Raman spectra of ice and salt hydrates in synthetic fluid inclusions’, *Chemical Geology*, 275(1–2), pp. 58–66. doi: 10.1016/j.chemgeo.2010.04.014.

Beegle, L. W. *et al.* (2014) ‘SHERLOC: Scanning Habitable Environments With Raman & Luminescence for Organics & Chemicals, an Investigation for 2020’, *11th International GeoRaman Conference*, (2014), p. 5101. doi: doi:10.2307/3595008.

Ben Mabrouk, K. *et al.* (2013) ‘Raman study of cation effect on sulfate vibration modes in solid state and in aqueous solutions’, *Journal of Raman Spectroscopy*, 44(11), pp. 1603–1608. doi: 10.1002/jrs.4374.

Berg, R. W. (2018) ‘Raman detection of hydrohalite formation: Avoiding accidents on icy roads by deicing where salt will not work’, *Applied Spectroscopy Reviews*. Taylor & Francis, 53(6), pp. 503–515. doi: 10.1080/05704928.2017.1396540.

Bland, M. T. *et al.* (2016) ‘Composition and structure of the shallow subsurface of Ceres revealed by crater morphology’, *Nature Geoscience*, 9(7), pp. 538–542. doi: 10.1038/ngeo2743.

Bonales, L. J., Muñoz-Iglesias, V. and Prieto-Ballesteros, O. (2014) ‘Raman spectroscopy as a tool to study the solubility of CO_2 in magnesium sulphate brines: application to the fluids of Europa’s cryomagmatic reservoirs’, *European Journal of Mineralogy*, 25(5), pp. 735–743. doi: 10.1127/0935-1221/2013/0025-2312.

Bost, N. *et al.* (2015) ‘Testing the ability of the ExoMars 2018 payload to document geological context and potential habitability on Mars’, *Planetary and Space Science*. Elsevier, 108(2015), pp. 87–97. doi: 10.1016/j.pss.2015.01.006.

Boxe, C. S. *et al.* (2012) ‘Adsorbed water and thin liquid films on Mars’, *International Journal of Astrobiology*, 11(3), pp. 169–175. doi: 10.1017/S1473550412000080.

Carr, M. H. and Head, J. W. (2010) ‘Geologic history of Mars’, *Earth and Planetary Science Letters*. Elsevier B.V., 294(3–4), pp. 185–203. doi: 10.1016/j.epsl.2009.06.042.

Chevrier, V. F., Hanley, J. and Altheide, T. S. (2009) ‘Stability of perchlorate hydrates and their liquid solutions at the Phoenix landing site, mars’, *Geophysical Research Letters*, 36(10). doi: 10.1029/2009GL037497.

Chevrier, V. F. and Rivera-Valentin, E. G. (2012) ‘Formation of recurring slope lineae by liquid brines on present-day Mars’, *Geophysical Research Letters*, 39(21), pp. 1–5. doi: 10.1029/2012GL054119.

Chou, I. M. and Wang, A. (2017) ‘Application of laser Raman micro-analyses to Earth and planetary materials’, *Journal of Asian Earth Sciences*. Elsevier, 145(July), pp. 309–333. doi: 10.1016/j.jseaes.2017.06.032.

Clifford, S. M. and Parker, T. J. (2001) ‘The evolution of the Martian hydrosphere: Implications for the fate of a primordial ocean and the current state of the Northern plains’, *Icarus*, 154(1), pp. 40–79. doi: 10.1006/icar.2001.6671.

Cook, K. and Hartel, R. (2010). Crystallization in Ice Cream Production. Comprehensive Reviews in Food Science and Food Safety, 9, 213–222.

Dundas, C. M. *et al.* (2013) ‘Recurring slope lineae in equatorial regions of Mars’, *Nature Geoscience*. Nature Publishing Group, 7(1), pp. 53–58. doi: 10.1038/ngeo2014.

Duričković, I. *et al.* (2011) ‘Water-ice phase transition probed by Raman spectroscopy’, *Journal of Raman Spectroscopy*, 42(6), pp. 1408–1412. doi: 10.1002/jrs.2841.

Edwards, C. S. and Piqueux, S. (2016) ‘The water content of recurring slope lineae on Mars’, *Geophysical Research Letters*, 43(17), pp. 8912–8919. doi: 10.1002/2016GL070179.

Edwards, H. G. M. (2005) *Modern Raman spectroscopy—a practical approach. Ewen Smith and Geoffrey Dent. John Wiley and Sons Ltd, Chichester, 2005. Pp. 210. ISBN 0 471 49668 5 (cloth, hb); 0 471 49794 0 (pbk)*, *Journal of Raman Spectroscopy*. doi: 10.1002/jrs.1320.

Genceli, F. E. et al. (2007) ‘Crystallization and characterization of a new magnesium sulfate hydrate MgSO4 11H2O’, Crystal Growth and Design, 7(12), pp. 2460–2466. doi: 10.1021/cg060794e.

Elif Genceli, F. *et al.* (2009) ‘Meridianiite detected in ice’, *Journal of Glaciology*, 55(189), pp. 117–122. doi: 10.3189/002214309788608921.

Fischer, E. (2016) ‘Searching for brine on Mars using Raman spectroscopy’, 28(2016), pp. 181–195.

Fortes, A. D. *et al.* (2007) 'Ammonium sulfate on Titan: Possible origin and role in cryovolcanism', *Icarus*, 188(1), pp. 139–153. doi: 10.1016/j.icarus.2006.11.002.

Hallsworth, J. E. *et al.* (2007) 'Limits of life in MgCl2-containing environments: Chaotropicity defines the window', *Environmental Microbiology*, 9(3), pp. 801–813. doi: 10.1111/j.1462-2920.2006.01212.x.

Hanley, J. *et al.* (2012) 'Chlorate salts and solutions on Mars', *Geophysical Research Letters*, 39(8), pp. 2–6. doi: 10.1029/2012GL051239.

Harris, L. V. *et al.* (2015) 'Selection of portable spectrometers for planetary exploration: A comparison of 532 nm and 785 nm raman spectroscopy of reduced carbon in Archean cherts', *Astrobiology*, 15(6), pp. 420–429. doi: 10.1089/ast.2014.1220.

Heinz, J., Schulze-Makuch, D. and Kounaves, S. P. (2016) 'Deliquescence-induced wetting and RSL-like darkening of a Mars analogue soil containing various perchlorate and chloride salts', *Geophysical Research Letters*, 43(10), pp. 4880–4884. doi: 10.1002/2016GL068919.

Horne, D. J. (2018) 'Young, small-scale surface features in Meridiani Planum, Mars: A possible signature of recent transient liquid and gas emissions', *Planetary and Space Science*. Elsevier Ltd, 157(April), pp. 10–21. doi: 10.1016/j.pss.2018.04.012.

Lewis, A. E. *et al.* (2010) 'Design of a Eutectic Freeze Crystallization process for multicomponent waste water stream', *Chemical Engineering Research and Design*. Institution of Chemical Engineers, 88(9), pp. 1290–1296. doi: 10.1016/j.cherd.2010.01.023.

Lohumi, S., Kim, M. S., Qin, J., & Cho, B. K. (2017). Raman imaging from microscopy to macroscopy: Quality and safety control of biological materials. TrAC - Trends in Analytical Chemistry, 93, 183–198. https://doi.org/10.1016/j.trac.2017.06.002

Martínez, G. M. and Renno, N. O. (2013) ‘Water and brines on mars: Current evidence and implications for MSL’, *Space Science Reviews*, 175(1–4), pp. 29–51. doi: 10.1007/s11214-012-9956-3.

Martinez-Uriartem, L. *et al.* (2014) ‘REFERENCE RAMAN SPECTRA OF CaCl2.nH2O solids (n= 0, 2, 4, 6).’, *11th International GeoRaman Conference (2014)*, pp. 5–6.

Massé, M. *et al.* (2015) ‘Spectral evidence for hydrated salts in recurring slope lineae on Mars’, *Nature Geoscience*, 8(11), pp. 829–832. doi: 10.1038/ngeo2546.

McEwen, A. *et al.* (2015) ‘Recurring Slope Lineae on Mars : Atmospheric Origin ?’, *European Planetary Science Congress*, 10, pp. 10–11.

McEwen, A. S. *et al.* (2011) ‘Seasonal flows on warm Martian slopes’, *Science*, 333(6043), pp. 740–743. doi: 10.1126/science.1204816.

McGraw, L. E., McCollom, N. D. S., Phillips-Lander, C. M., & Elwood Madden, M. E. (2018). Measuring Perchlorate and Sulfate in Planetary Brines Using Raman Spectroscopy [Research-article]. ACS Earth and Space Chemistry, 2(10), 1068–1074. https://doi.org/10.1021/acsearthspacechem.8b00082

Möhlmann, D. and Thomsen, K. (2011) ‘Properties of cryobrines on Mars’, *Icarus*, 212(1), pp. 123–130. doi: 10.1016/j.icarus.2010.11.025.

Moral, A. G. *et al.* (2018) '49th Lunar and Planetary Science Conference 2018 (LPI Contrib. No. 2083) 2449.pdf Raman Laser Spectrometer for 2020 ExoMars Mission. Engineering and Qualification Model Capabilities and Future Activities', 2018(2083), pp. 4–5.

Narayanaswamy, P. K. (1948) 'The Raman Spectra of Water, Heavy Water and Ice'.

Nebgen, J. W., Mcelroy, A. D. and Klodowski, H. F. (1965) 'Raman and Infrared Spectra of Nitronium Perchlorate', *Inorganic Chemistry*, 4(12), pp. 1796–1799. doi: 10.1021/ic50034a030.

Nikolakakos, G. and Whiteway, J. A. (2015) 'Laboratory investigation of perchlorate deliquescence at the surface of Mars with a Raman scattering lidar', *Geophysical Research Letters*, 42(19), pp. 7899–7906. doi: 10.1002/2015GL065434.

Nuding, D. L. *et al.* (2014) 'Deliquescence and efflorescence of calcium perchlorate: An investigation of stable aqueous solutions relevant to mars', *Icarus*. Elsevier Inc., 243, pp. 420–428. doi: 10.1016/j.icarus.2014.08.036.

Primm, K. M. *et al.* (2018) 'The Effect of Mars-Relevant Soil Analogs on the Water Uptake of Magnesium Perchlorate and Implications for the Near-Surface of Mars', *Journal of Geophysical Research: Planets*, 123(8), pp. 2076–2088. doi: 10.1029/2018JE005540.

Rao, B. *et al.* (2012) 'Perchlorate production by photodecomposition of aqueous chlorine solutions', *Environmental Science and Technology*, 46(21), pp. 11635–11643. doi: 10.1021/es3015277.

Rennó, N. O. *et al.* (2009) ‘Possible physical and thermodynamical evidence for liquid water at the Phoenix landing site’, *Journal of Geophysical Research E: Planets*, 114(10), pp. 1–11. doi: 10.1029/2009JE003362.

Root, M. J. and Elwood Madden, M. E. (2012) ‘Potential effects of obliquity change on gas hydrate stability zones on Mars’, *Icarus*. Elsevier Inc., 218(1), pp. 534–544. doi: 10.1016/j.icarus.2011.12.024.

Rull, F. *et al.* (2017) ‘The Raman Laser Spectrometer for the ExoMars Rover Mission to Mars’, *Astrobiology*, 17(6–7), pp. 627–654. doi: 10.1089/ast.2016.1567.

Samson, I., Anderson, A. and Marshall, D. (eds) (2003) *Fluid Inclusions: Analysis and Interpretation*. Series Vol. Vancouver, British Columbia: Mineralogical Association of Canada.

Schmidt, F. *et al.* (2017) ‘Formation of recurring slope lineae on Mars by rarefied gas-triggered granular flows’, *Nature Geoscience*, 10(4), pp. 270–273. doi: 10.1038/ngeo2917.

Sohl, F. *et al.* (2010) ‘Subsurface water oceans on icy satellites: Chemical composition and exchange processes’, *Space Science Reviews*, 153(1–4), pp. 485–510. doi: 10.1007/s11214-010-9646-y.

Solomon, S. C. *et al.* (2005) ‘New perspectives on ancient Mars’, *Science*, 307(5713), pp. 1214–1220. doi: 10.1126/science.1101812.

Squyres, S. (1984) ‘The History of Water on Mars’, *Annual Review of Earth and Planetary Sciences*, 12(1), pp. 83–106. doi: 10.1146/annurev.earth.12.1.83.

Stevenson, A. *et al.* (2015) ‘Multiplication of microbes below 0.690 water activity: Implications for terrestrial and extraterrestrial life’, *Environmental Microbiology*, 17(2), pp. 257–277. doi: 10.1111/1462-2920.12598.

Stillman, D. E. and Grimm, R. E. (2018) ‘Two pulses of seasonal activity in martian southern mid-latitude recurring slope lineae (RSL)’, *Icarus*. Elsevier Inc., 302, pp. 126–133. doi: 10.1016/j.icarus.2017.10.026.

Stillman, D. E. *et al.* (2016) ‘Observations and modeling of northern mid-latitude recurring slope lineae (RSL) suggest recharge by a present-day martian briny aquifer’, *Icarus*. Elsevier Inc., 265, pp. 125–138. doi: 10.1016/j.icarus.2015.10.007.

Thomas, E. C. *et al.* (2017) ‘Composition and Evolution of Frozen Chloride Brines under the Surface Conditions of Europa’, *ACS Earth and Space Chemistry*, 1(1), pp. 14–23. doi: 10.1021/acsearthspacechem.6b00003.

Toner, J. D., Catling, D. C. and Light, B. (2014) ‘The formation of supercooled brines, viscous liquids, and low-temperature perchlorate glasses in aqueous solutions relevant to Mars’, *Icarus*. Elsevier Inc., 233, pp. 36–47. doi: 10.1016/j.icarus.2014.01.018.

Vaniman, D. T. *et al.* (2004) ‘Magnesium sulphate salts and the history of water on Mars’, *Nature*, 431(7009), pp. 663–665. doi: 10.1038/nature02973.

Wang, A. *et al.* (2006) ‘Sulfates on Mars: A systematic Raman spectroscopic study of hydration states of magnesium sulfates’, *Geochimica et Cosmochimica Acta*, 70(24), pp. 6118–6135. doi: 10.1016/j.gca.2006.05.022.

Wang, Y. *et al.* (2016) 'Ratiometric detection of Raman hydration shell spectra', *Journal of Raman Spectroscopy*, 47(10), pp. 1231–1238. doi: 10.1002/jrs.4940.

Wang, Z. *et al.* (2004) 'Vibrational substructure in the OH stretching transition of water and HOD', *Journal of Physical Chemistry A*, 108(42), pp. 9054–9063. doi: 10.1021/jp048545t.

Wei, D., Chen, S., & Liu, Q. (2015). Review of fluorescence suppression techniques in Raman spectroscopy. *Applied Spectroscopy Reviews*, *50*(5), 387-406.

White, S. N. (2009) 'Laser Raman spectroscopy as a technique for identification of seafloor hydrothermal and cold seep minerals', *Chemical Geology*, 259(3–4), pp. 240–252. doi: 10.1016/j.chemgeo.2008.11.008.

Wiens, R. C., Maurice, S., & Perez, F. R. (2017). The SuperCam remote sensing instrument suite for the Mars 2020 rover: A preview. Spectroscopy (Santa Monica), 32(5), 50–55.

Wu, Z., Wang, A. and Ling, Z. (2016) 'Spectroscopic study of perchlorates and other oxygen chlorides in a Martian environmental chamber', *Earth and Planetary Science Letters*. Elsevier B.V., 452, pp. 123–132. doi: 10.1016/j.epsl.2016.07.044.

Yakimov, M. M. *et al.* (2015) 'Microbial community of the deep-sea brine Lake Kryos seawater-brine interface is active below the chaotropicity limit of life as revealed by recovery of mRNA', *Environmental Microbiology*, 17(2), pp. 364–382. doi: 10.1111/1462-2920.12587.

Yang, D., Xiong, X. and Chen, W. (2019) 'Cryogenic raman spectroscopic studies on common Ore-forming Fluid Systems', *Minerals*, 9(6), pp. 1–14. doi: 10.3390/min9060363.

Zolensky, M. E. *et al.* (1999) ‘Asteroidal water within fluid inclusion-bearing halite in an H5 chondrite, Monahans (1998)’, *Science*, 285(5432), pp. 1377–1379. doi: 10.1126/science.285.5432.1377.

Zhang, Z. and Liu, X. Y. (2018) ‘Control of ice nucleation: Freezing and antifreeze strategies’, *Chemical Society Reviews*. Royal Society of Chemistry, 47(18), pp. 7116–7139. doi: 10.1039/c8cs00626a.

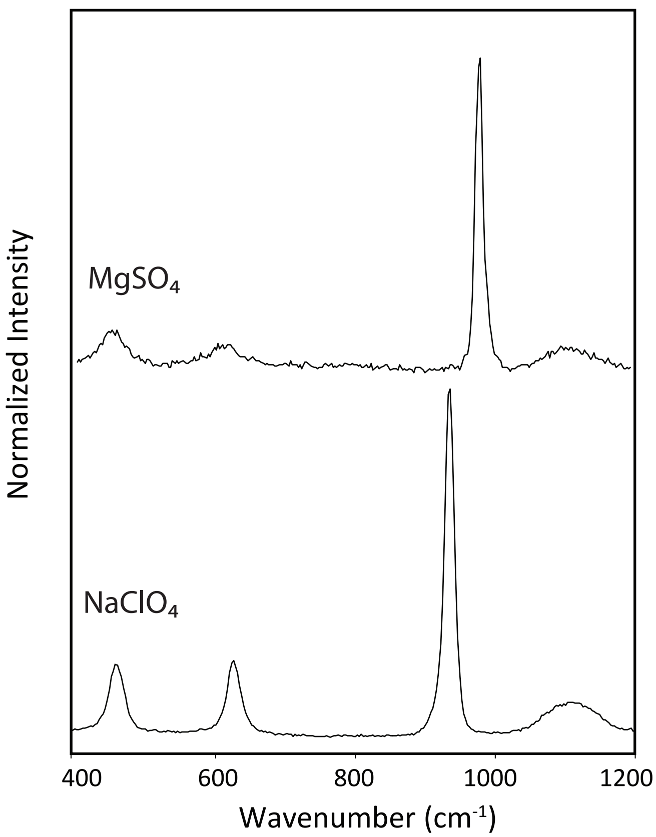

MgSO4
NaClO4
Normalized Intensity
400
600
800
1000
1200
Wavenumber (cm-1)

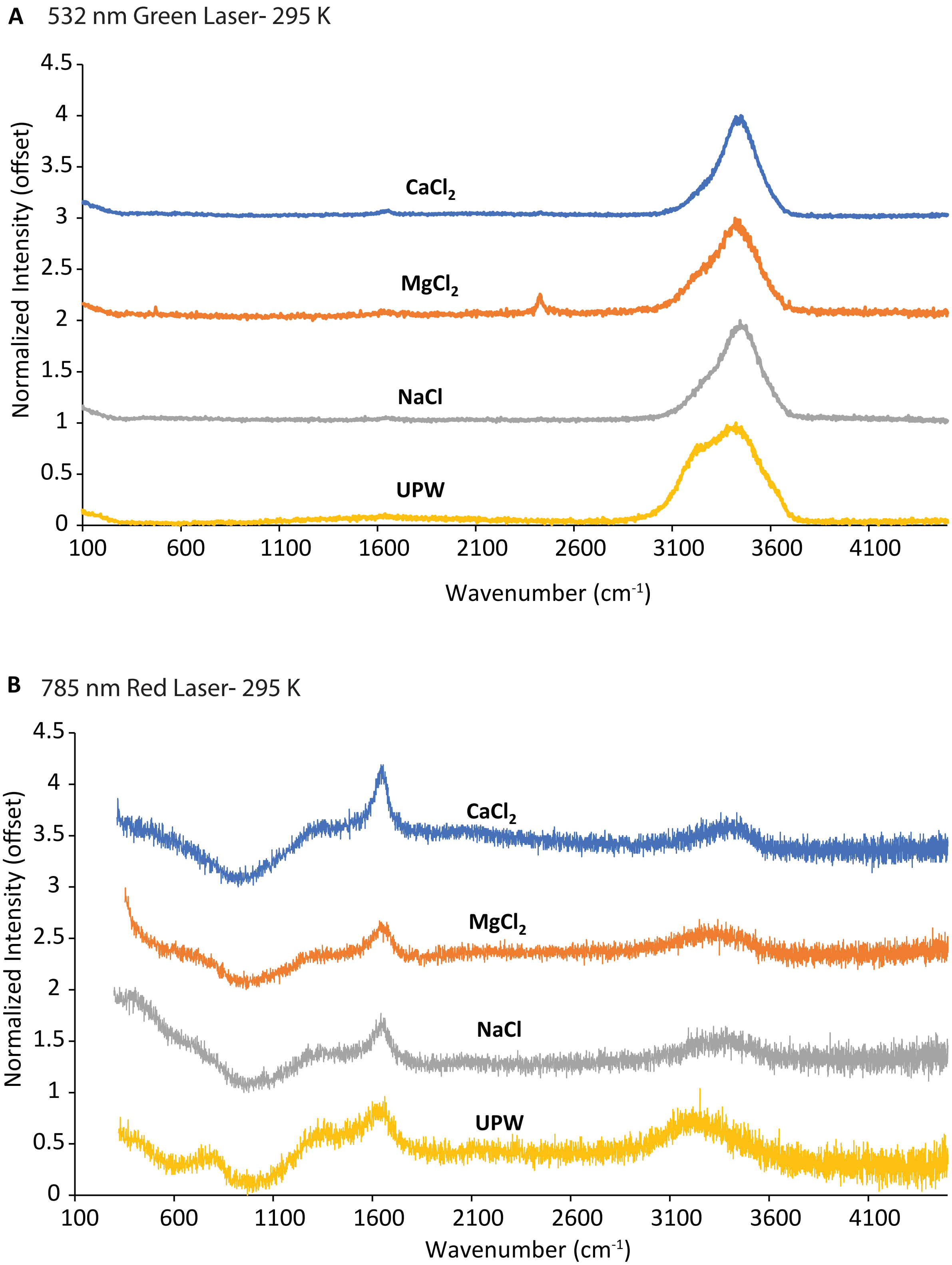
A 532 nm Green Laser- 295 K
CaCl2
MgCl2
NaCl
UPW
Normalized Intensity (offset)
Wavenumber (cm-1)
B 785 nm Red Laser- 295 K
CaCl2
MgCl2
NaCl
UPW
Normalized Intensity (offset)
Wavenumber (cm-1)

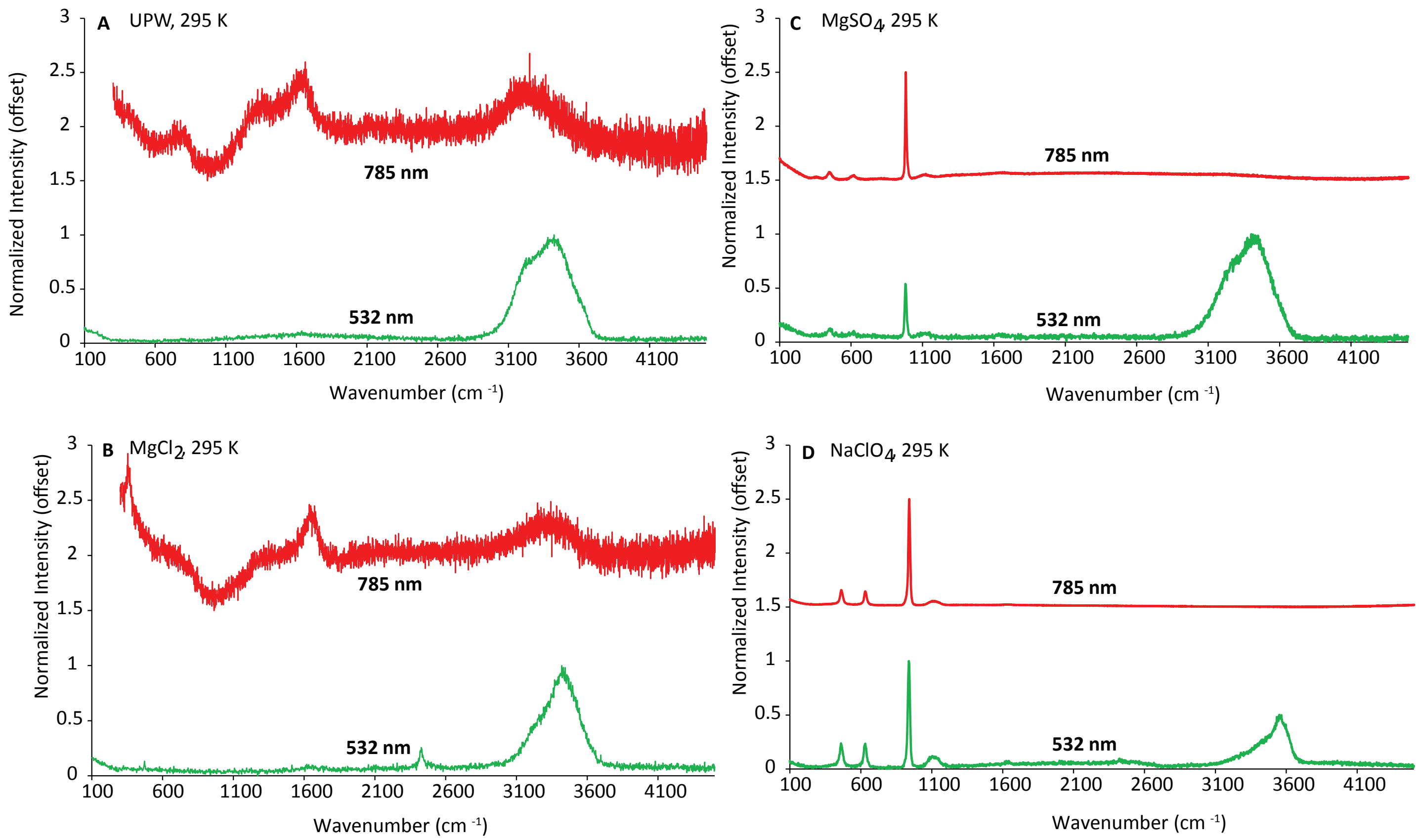
A UPW, 295 K
785 nm
532 nm
B MgCl2, 295 K
785 nm
532 nm
C MgSO4, 295 K
785 nm
532 nm
D NaClO4, 295 K
785 nm
532 nm
Normalized Intensity (offset)
Wavenumber (cm -1)
0 0.5 1 1.5 2 2.5 3
100 600 1100 1600 2100 2600 3100 3600 4100

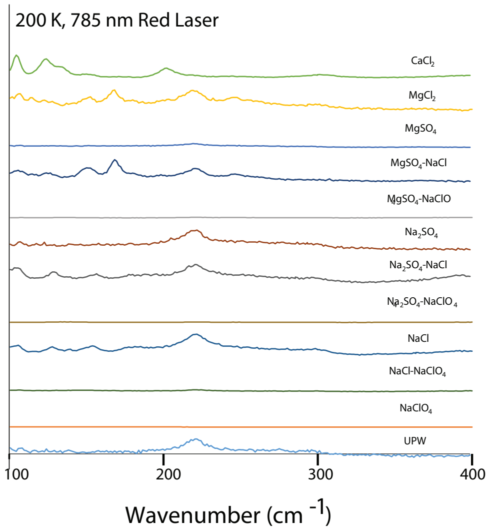

200 K, 785 nm Red Laser
CaCl2
MgCl2
MgSO4
MgSO4-NaCl
MgSO4-NaClO
Na2SO4
Na2SO4-NaCl
Na2SO4-NaClO4
NaCl
NaCl-NaClO4
NaClO4
UPW
100
200
300
400
Wavenumber (cm -1)

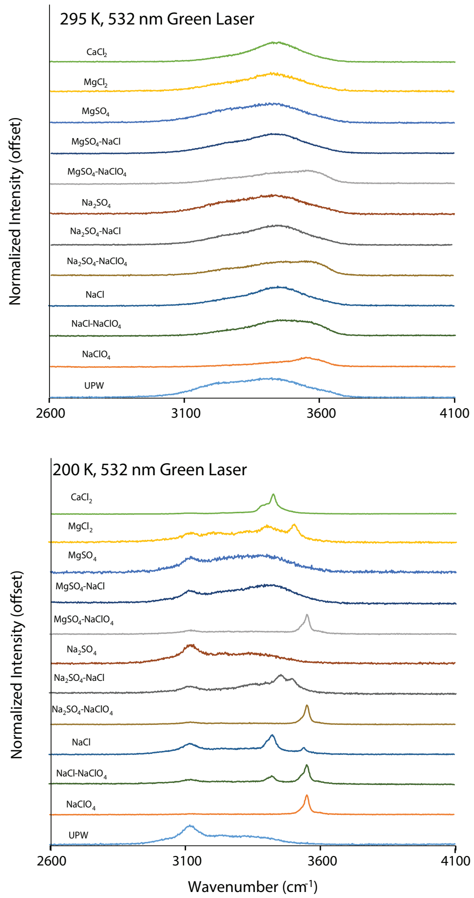
295 K, 532 nm Green Laser
CaCl2
MgCl2
MgSO4
MgSO4-NaCl
MgSO4-NaClO4
Na2SO4
Na2SO4-NaCl
Na2SO4-NaClO4
NaCl
NaCl-NaClO4
NaClO4
UPW
Normalized Intensity (offset)
2600
3100
3600
4100
200 K, 532 nm Green Laser
CaCl2
MgCl2
MgSO4
MgSO4-NaCl
MgSO4-NaClO4
Na2SO4
Na2SO4-NaCl
Na2SO4-NaClO4
NaCl
NaCl-NaClO4
NaClO4
UPW
Normalized Intensity (offset)
2600
3100
3600
4100
Wavenumber (cm-1)

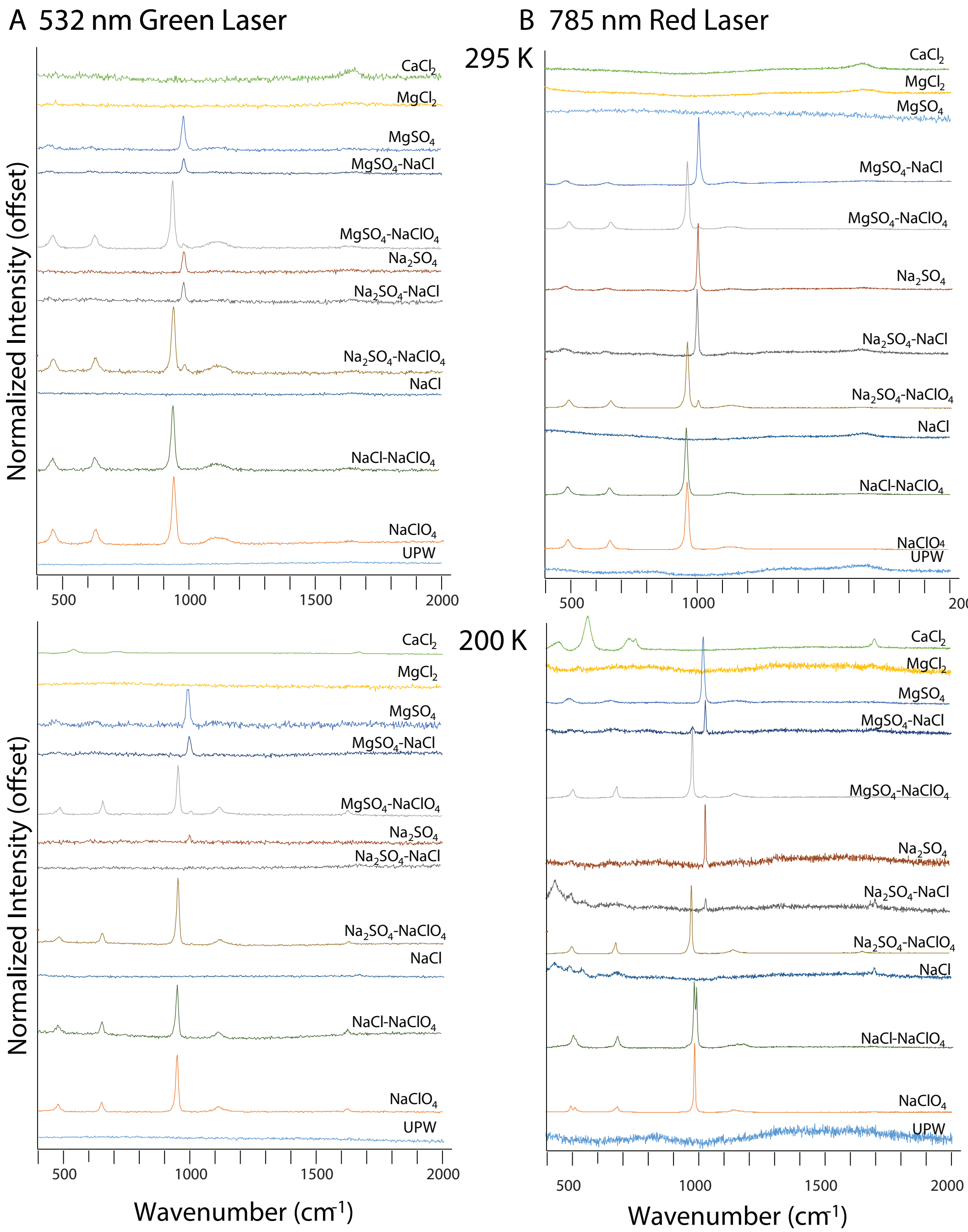

A 532 nm Green Laser
B 785 nm Red Laser
295 K
200 K
CaCl2
MgCl2
MgSO4
MgSO4-NaCl
MgSO4-NaClO4
Na2SO4
Na2SO4-NaCl
Na2SO4-NaClO4
NaCl
NaCl-NaClO4
NaClO4
UPW
Normalized Intensity (offset)
500
1000
1500
2000
Wavenumber (cm-1)

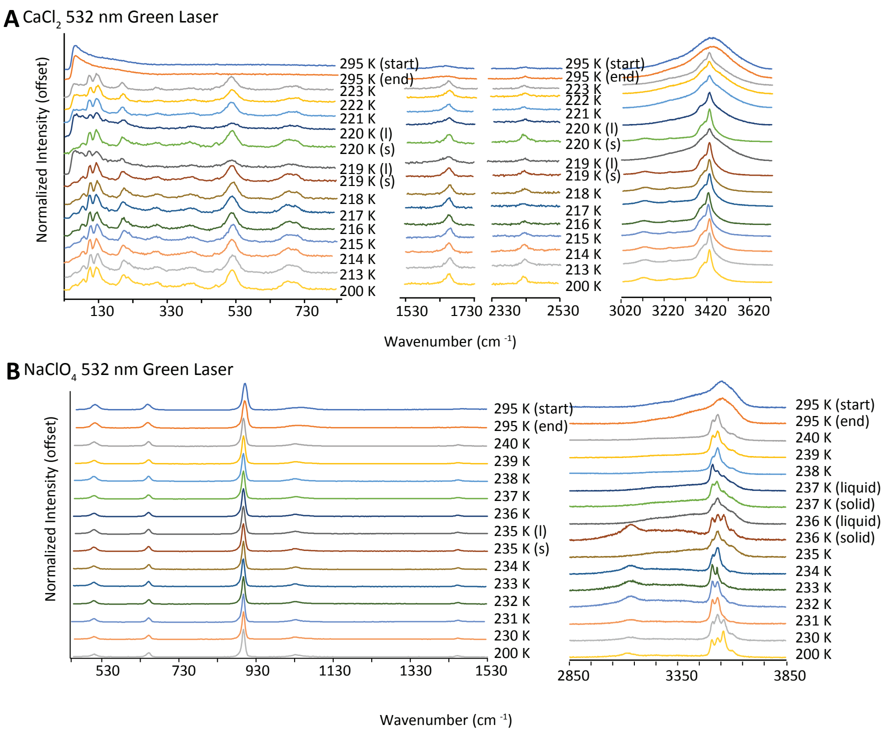
A
CaCl2 532 nm Green Laser
Normalized Intensity (offset)
295 K (start)
295 K (end)
223 K
222 K
221 K
220 K (l)
220 K (s)
219 K (l)
219 K (s)
218 K
217 K
216 K
215 K
214 K
213 K
200 K
130
330
530
730
1530
1730
2330
2530
3020
3220
3420
3620
Wavenumber (cm -1)
B
NaClO4 532 nm Green Laser
Normalized Intensity (offset)
295 K (start)
295 K (end)
240 K
239 K
238 K
237 K
236 K
235 K (l)
235 K (s)
234 K
233 K
232 K
231 K
230 K
200 K
237 K (liquid)
237 K (solid)
236 K (liquid)
236 K (solid)
235 K
530
730
930
1130
1330
1530
2850
3350
3850
Wavenumber (cm -1)

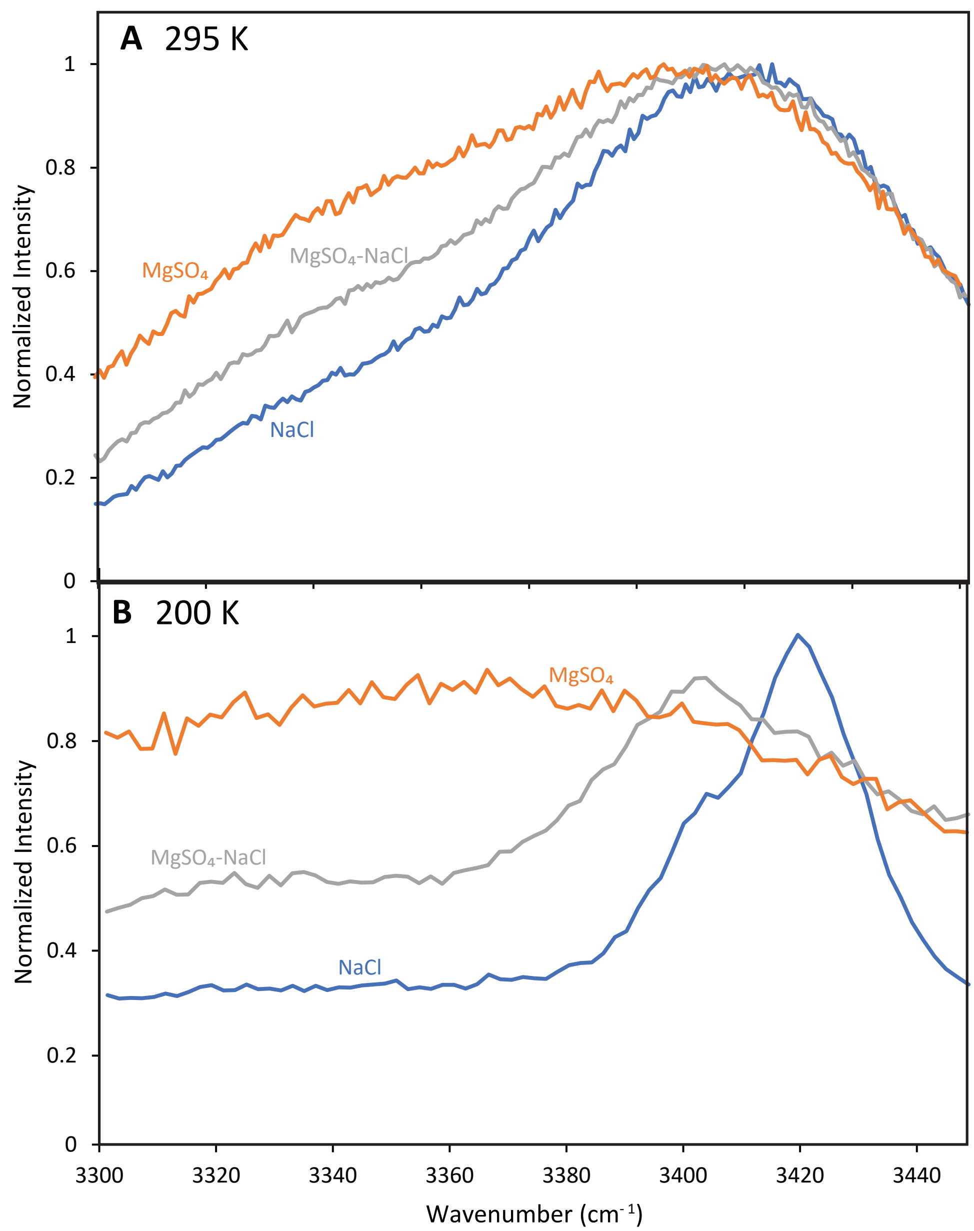

A 295 K
B 200 K
MgSO4
MgSO4-NaCl
NaCl
Normalized Intensity
Wavenumber (cm-1)
1
0.8
0.6
0.4
0.2
0
3300
3320
3340
3360
3380
3400
3420
3440

A $MgSO_4$- $NaClO_4$ 532 nm Green Laser

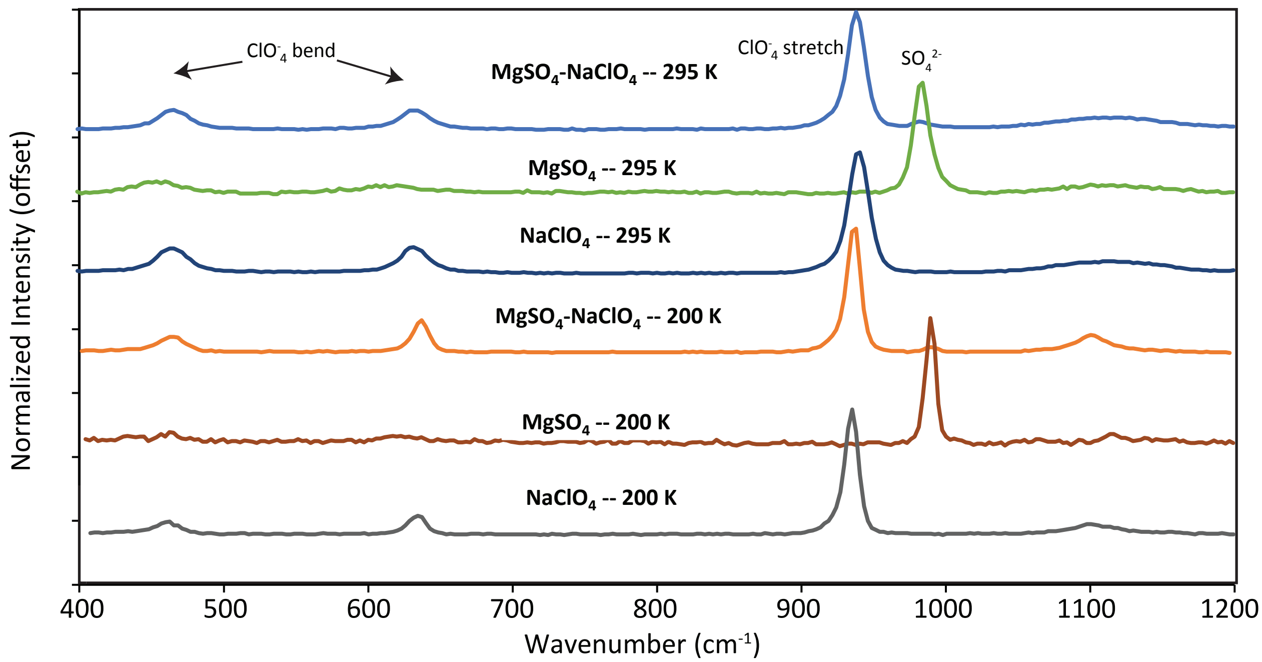

B $MgSO_4$- $NaClO_4$ 785 nm Red Laser

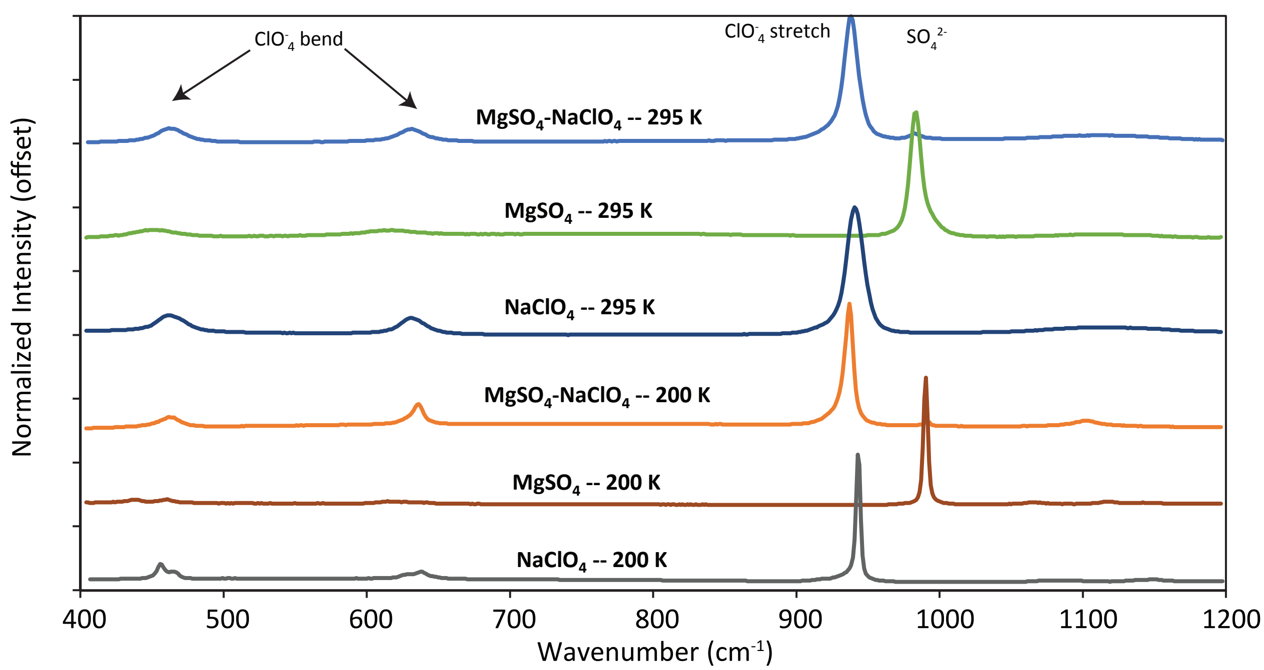

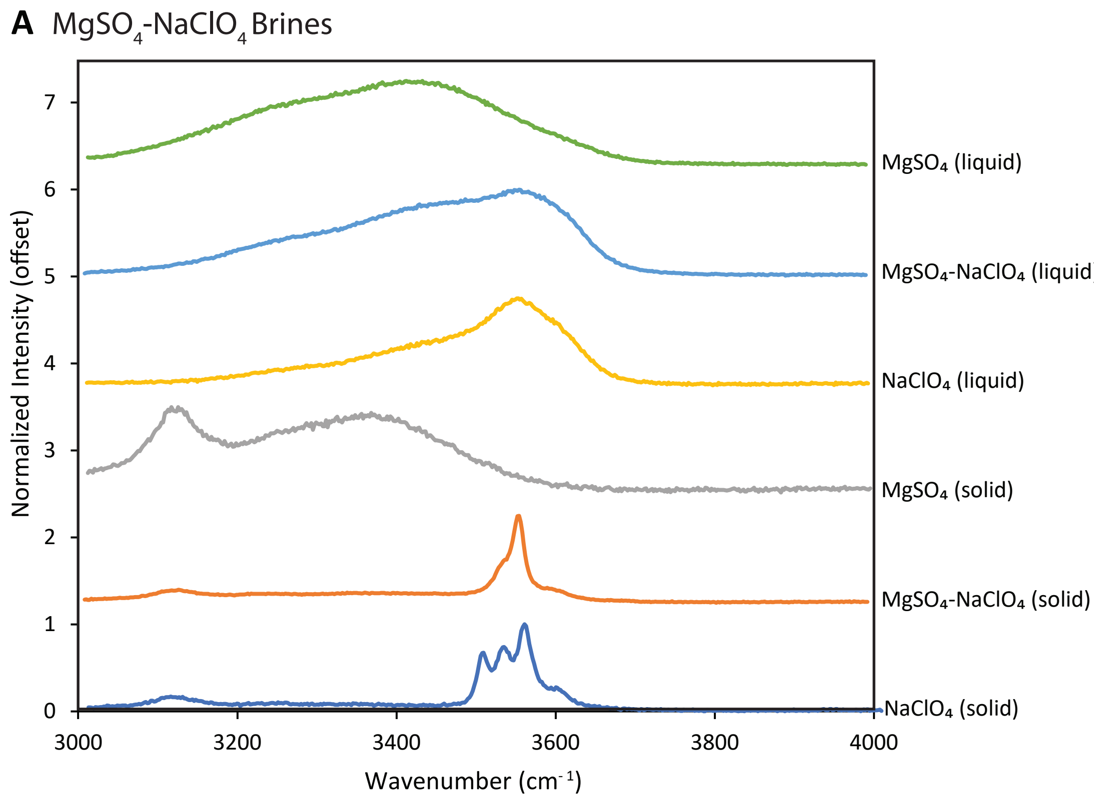

A MgSO4-NaClO4 Brines
Normalized Intensity (offset)
Wavenumber (cm-1)
MgSO4 (liquid)
MgSO4-NaClO4 (liquid)
NaClO4 (liquid)
MgSO4 (solid)
MgSO4-NaClO4 (solid)
NaClO4 (solid)

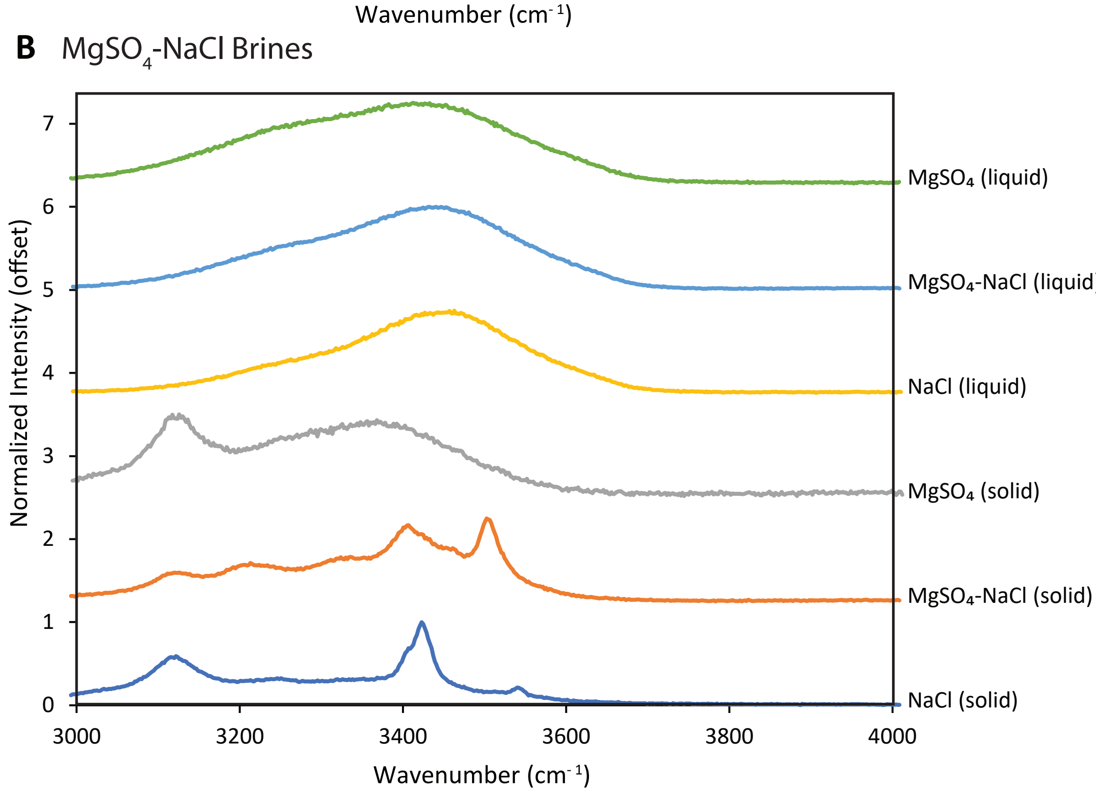

B MgSO4-NaCl Brines
Normalized Intensity (offset)
Wavenumber (cm-1)
MgSO4 (liquid)
MgSO4-NaCl (liquid)
NaCl (liquid)
MgSO4 (solid)
MgSO4-NaCl (solid)
NaCl (solid)

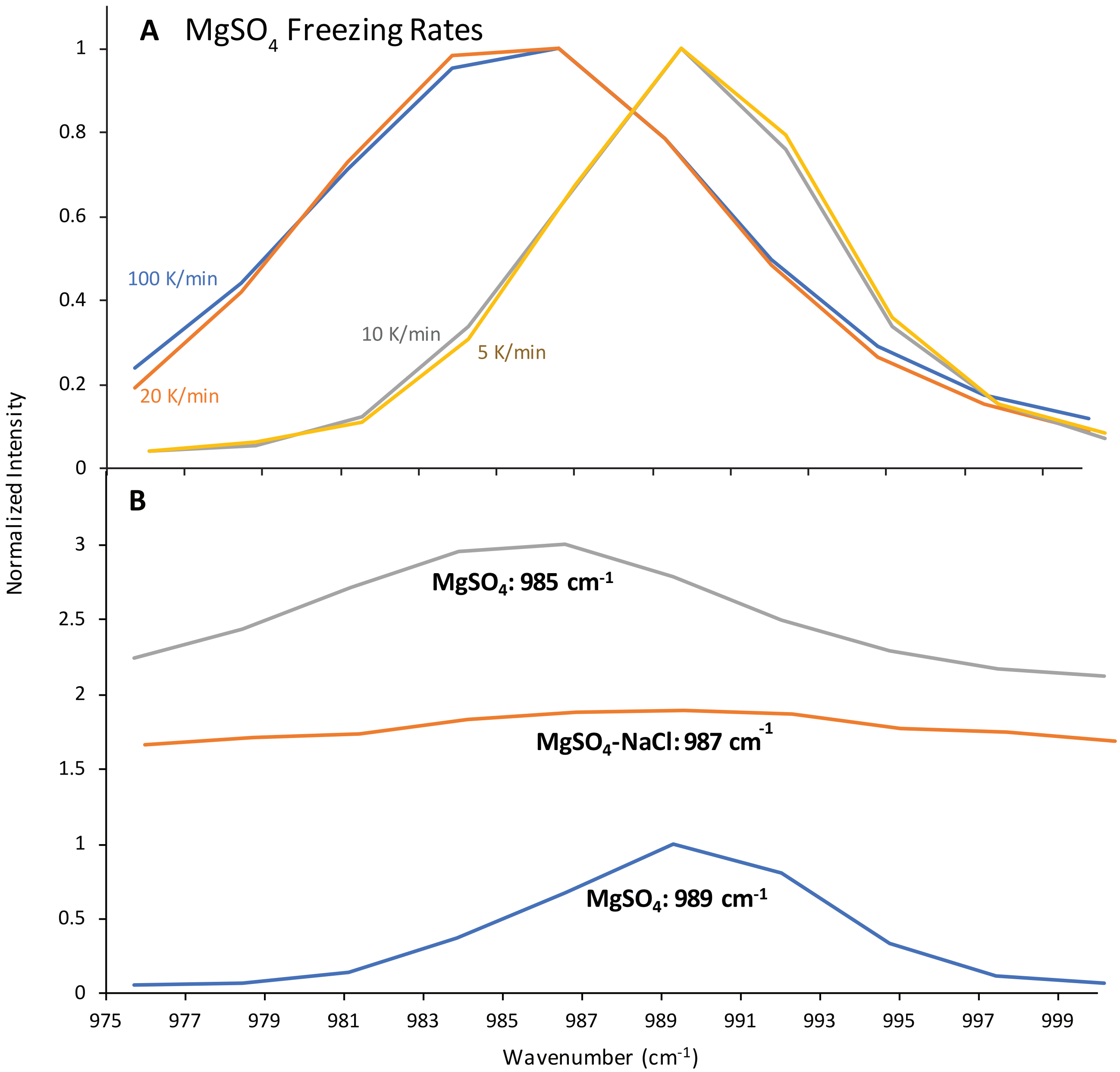

A MgSO4 Freezing Rates
100 K/min
20 K/min
10 K/min
5 K/min
B
MgSO4: 985 cm-1
MgSO4-NaCl: 987 cm-1
MgSO4: 989 cm-1
Normalized Intensity
Wavenumber (cm-1)

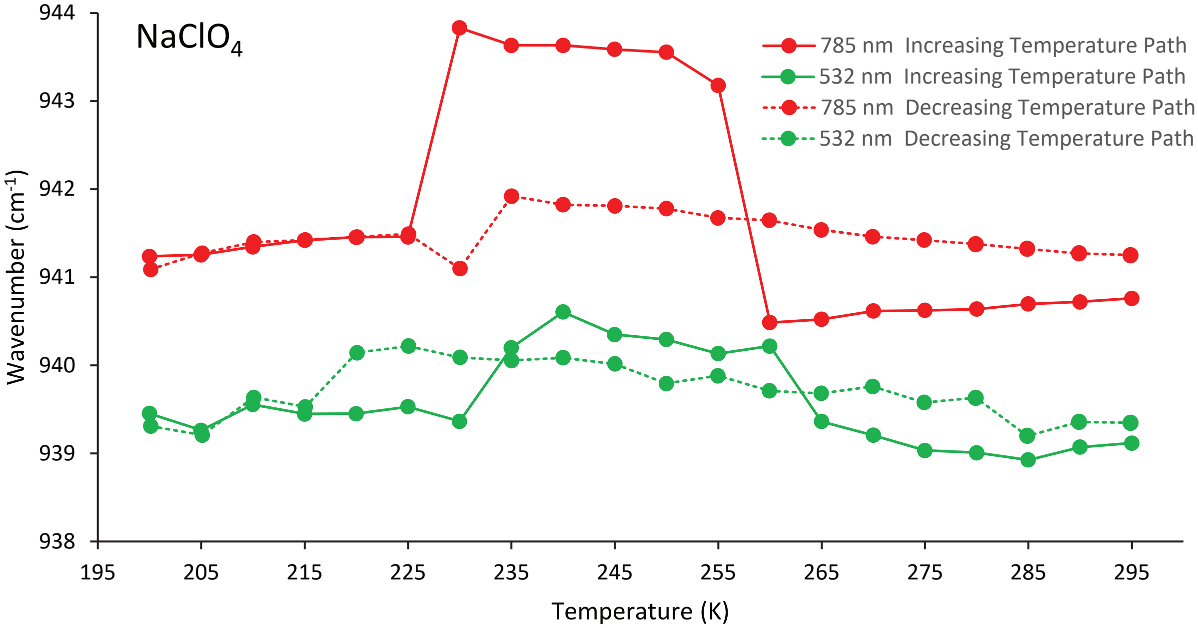

NaClO4
785 nm Increasing Temperature Path
532 nm Increasing Temperature Path
785 nm Decreasing Temperature Path
532 nm Decreasing Temperature Path
944
943
942
941
940
939
938
Wavenumber (cm-1)
195
205
215
225
235
245
255
265
275
285
295
Temperature (K)

Table 1
Curve fits of specific bands/peaks for each of the spectra in Fig. 2.

OH-bend Peak 532 nm (~1644 cm^{-1})					OH-bend Peak 785 nm (~1644 cm^{-1})				
	Centre	*Width*	*Height*	*Area*		*Centre*	*Width*	*Height*	*Area*
$CaCl_2$, 295 K	1644.7	78.0	0.04	4.62	*$CaCl_2$, 295 K*	1641.3	150.0	0.09	19.06
$MgCl_2$, 295 K	1649.6	163.2	0.03	4.41	*$MgCl_2$, 295 K*	1630.8	187.6	0.06	16.80
NaCl, 295 K	1647.9	81.4	0.02	1.96	*NaCl, 295 K*	1637.5	119.0	0.06	8.96
UPW, 295 K	1682.5	779.1	0.05	37.69	*UPW, 295 K*	1615.0	250.0	0.10	39.15
OH-stretch Peak 532 nm (~3200 cm^{-1})					**OH-stretch Peak 785 nm (~3200 cm^{-1})**				
	Centre	*Width*	*Height*	*Area*		*Centre*	*Width*	*Height*	*Area*
$CaCl_2$, 295 K	3233.1	158.3	0.17	37.14	*$CaCl_2$, 295 K*	3249.9	250.0	0.02	5.49
$MgCl_2$, 295 K	3221.3	203.4	0.26	82.97	*$MgCl_2$, 295 K*	3245.0	250.0	0.04	14.90
NaCl, 295 K	3255.8	189.3	0.21	51.65	*NaCl, 295 K*	3250.0	247.7	0.02	7.23
UPW, 295 K	3204.9	218.0	0.48	139.39	*UPW, 295 K*	3215.0	250.0	0.09	33.70
OH-stretch Peak 532 nm (~3400 cm^{-1})					**OH-stretch Peak 785 nm (~3400 cm^{-1})**				
	Centre	*Width*	*Height*	*Area*		*Centre*	*Width*	*Height*	*Area*
$CaCl_2$, 295 K	3442.1	217.6	0.91	223.87	*$CaCl_2$, 295 K*	3424.3	160.3	0.02	5.18
$MgCl_2$, 295 K	3434.3	247.8	0.80	232.75	*$MgCl_2$, 295 K*	3431.9	258.7	0.07	19.11
NaCl, 295 K	3451.8	227.8	0.91	271.07	*NaCl, 295 K*	3431.9	200.0	0.02	6.39
UPW, 295 K	3430.6	299.0	0.85	269.38	*UPW, 295 K*	3417.3	224.9	0.03	8.90

Table 2

Melting points of brines.

Brine	Observed Melting T (K) [this study]	Eutectic T (K) [from literature]	Weight % salt in saturated brine	Moles of salt/kg H_2O
$CaCl_2$	218–219	223[c]	30.50	3.95
$NaCl$-$NaClO_4$	232–233	–	–	–
$MgSO_4$-$NaClO_4$	234	–	–	–
Na_2SO_4-$NaClO_4$	235–236	–	–	–
$NaClO_4$	235–237	238.9[d]	52.00	8.85
$MgSO_4$-$NaCl$	236–237	–	–	–
$MgCl_2$	239–240	240.2[d]	21.00	2.79
Na_2SO_4-$NaCl$	250–251	251[c]	–	–
$NaCl$	251–252	251[c] 251.9[d]	23.30	5.20
$MgSO_4$	270–271	269[c];269.4[d] *	16.50	1.64
Na_2SO_4	271–272	271[b];271.8[b] *	4.15	0.30
Ultrapure water	274	273.2[a]	0.00	0.00

[a]Chevrier and Rivera-Valentin 2012; [b]Lewis et al., 2010; [c]Möhlmann and Thomsen, 2011; [d]Toner et al., 2014

*hydrated salt phase present.

Table 3

532 nm green and 785 nm red wavelength curve fit data for $MgSO_4$, $MgSO_4$-$NaClO_4$, and $NaClO_4$ spectra between 400 cm^{-1} and 1200 cm^{-1} at both 200 K and 295 K (Fig. 9).

		SO_4/ClO_4 bend (−450 cm^{-1}), 532 nm				SO_4/ClO_4 bend (−450 cm^{-1}), 785 nm			
Brine	T (K)	*Centre*	*Width*	*Height*	*Area*	*Centre*	*Width*	*Height*	*Area*
$MgSO_4$	200	457.73	0.95	0.69	0.87	437.37	25.37	0.03	1.16
$MgSO_4$	200	–	–	–	–	460.00	16.52	0.02	0.45
$MgSO_4$	295	453.42	40.73	0.08	3.62	451.48	32.22	0.05	2.05
$MgSO_4$-$NaClO_4$	200	464.09	31.55	0.14	6.91	462.53	20.00	0.13	4.24
$MgSO_4$-$NaClO_4$	295	464.59	27.91	0.16	6.42	462.72	32.57	0.11	5.82
$NaClO_4$	200	460.27	20.40	0.09	3.00	456.15	10.02	0.10	1.31
$NaClO_4$	200	–	–	–	–	466.17	14.02	0.06	1.20
$NaClO_4$	295	463.91	26.90	0.20	8.41	462.60	24.21	0.14	5.25
		SO_4/ClO_4bend (−620 cm^{-1}), 532 nm				SO_4/ClO_4bend (−620 cm^{-1}), 785 nm			
Brine	T (K)	*Centre*	*Width*	*Height*	*Area*	*Centre*	*Width*	*Height*	*Area*
$MgSO_4$	200	623.14	28.64	0.04	1.66	620.00	54.12	0.02	1.80
$MgSO_4$	295	615.58	51.84	0.06	4.65	632.36	140.58	0.04	9.29
$MgSO_4$-$NaClO_4$	200	636.15	18.11	0.26	7.39	622.00	20.00	0.09	2.77
$MgSO_4$-$NaClO_4$	200	–	–	–	–	636.84	10.00	0.19	3.04
$MgSO_4$-$NaClO_4$	295	631.91	21.66	0.15	5.24	631.36	40.00	0.10	6.27
$NaClO_4$	200	633.58	15.13	0.14	2.69	629.08	14.69	0.04	0.80
$NaClO_4$	200	–	–	–	–	640.10	22.03	0.05	1.43
$NaClO_4$	295	631.56	22.30	0.21	6.89	631.66	18.32	0.12	3.01
		ClO_4symmetric stretch (−940 cm^{-1}), 532 nm				ClO_4symmetric stretch (−940 cm^{-1}), 785 nm			
Brine	T (K)	*Centre*	*Width*	*Height*	*Area*	*Centre*	*Width*	*Height*	*Area*
$MgSO_4$-$NaClO_4$	200	936.03	11.48	1.03	17.54	936.54	8.65	0.95	12.89
$MgSO_4$-$NaClO_4$	295	937.87	14.51	0.91	17.79	937.99	12.16	1.01	19.20
$NaClO_4$	200	934.61	11.38	0.98	15.15	921.20	14.69	0.02	0.44
$NaClO_4$	200	–	–	–	–	943.90	1.34	1.00	1.76
$NaClO_4$	295	939.52	16.77	0.95	20.40	940.89	14.18	1.00	19.36
		SO_4symmetric stretch (−990 cm^{-1}), 532 nm				SO_4symmetric stretch (−990 cm^{-1}), 785 nm			
Brine	T (K)	*Centre*	*Width*	*Height*	*Area*	*Centre*	*Width*	*Height*	*Area*
$MgSO_4$	200	989.48	8.38	0.98	10.12	990.22	3.71	1.01	5.05
$MgSO_4$	295	983.10	13.17	0.87	15.45	983.46	10.13	0.96	13.09
$MgSO_4$-$NaClO_4$	200	990.91	1.18	0.37	0.63	991.11	15.00	0.08	1.86
$MgSO_4$-$NaClO_4$	295	983.18	8.66	0.03	0.27	984.43	10.00	0.07	1.16
		SO_4/ClO_4asymmetric stretch (−1100 cm^{-1}), 532 nm				SO_4/ClO_4asymmetric stretch (−1100 cm^{-1}), 785 nm			
Brine	T (K)	*Centre*	*Width*	*Height*	*Area*	*Centre*	*Width*	*Height*	*Area*
$MgSO_4$	200	1120.48	42.50	0.05	2.89	1065.34	12.30	0.01	0.27
$MgSO_4$	200	–	–	–	–	1118.42	16.69	0.02	0.41
$MgSO_4$	200	–	–	–	–	1145.00	273.90	0.01	4.48
$MgSO_4$	295	1114.78	79.69	0.05	4.57	1110.19	53.01	0.03	2.54
$MgSO_4$-$NaClO_4$	200	1100.90	35.86	0.16	8.99	1102.46	40.00	0.10	6.33
$MgSO_4$-$NaClO_4$	295	1113.49	66.38	0.07	6.21	1115.38	83.97	0.06	8.56
$NaClO_4$	200	1103.03	41.10	0.08	4.98	1082.11	61.19	0.01	0.97
$NaClO_4$	200	–	–	–	–	1119.80	60.00	0.07	6.31
$NaClO_4$	295	1113.84	78.79	0.08	6.77	1148.21	61.19	0.02	1.85

Appendix:

Raman Peak Positions:

The peak positions associated with both the solid and liquid phase associated with each solution tested are outlined below in Table A1.

Table A1: Raman Peak Positions

Solution	Wavenumber (cm^{-1})	Mode	Notes	Reference
UPW	212; 213	Translatory mode/libration		*Berg 2018; Narayanaswamy 1948*
UPW	450	H_2O libration bands	Peaks around 400 cm^{-1} - 500 cm^{-1}	*Martinez-Uriartem et al. 2014*
UPW	1616-1665	OH-bending	Generally at 1644 cm^{-1}; varies depending on composition/hydration state of brine	*Martinez-Uriartem et al. 2014*
UPW	1644	H_2O bending vibration		*Wang et al. 2006*
UPW	3090; 3138; 3216	OH-stretching (ice)	The 3216 cm^{-1} peak also seems to appear when sample is liquid	*Yang et al. 2019; Duričković et al. 2011; Yang et al. 2019*
UPW	3150	OH-stretching	Denoted in literature as a “strong ice band”	*Berg 2018*
UPW	3385; 3420, 3423	OH-stretching (water)		*Duričković et al. 2011; Duričković et al. 2011, Wang et al. 2006*
$CaCl_2$	520	H_2O libration	Specific to $CaCl_2$	*Martinez-Uriartem et al. 2014*
$CaCl_2$	3407, 3430	Indicative of antarcticite ($CaCl_2$*$6H_2O$)	Peaks occur in OH-stretching band region	Thomas et al. 2017; Baumgartner and Bakker 2010
$MgCl_2$	3344, 3394, 3504	$MgCl_2$ hexahydrate (bischofite)	Slight shifting of peaks when thawed and then cooled again	Thomas et al. 2017
$MgSO_4$	451, 617, 1113	SO_4 (aq.) vibrational modes	The former two peaks are a result of SO_4 bending; the latter a result of asymmetric stretching	*Wang et al. 2006; Ben Mabrouk et al. 2013*
$MgSO_4$	444; 460	SO_4 bending vibrational mode in meridianiite		*Elif Genceli et al. 2009; Wang et al. 2006; Ben Mabrouk et al. 2013*

Solution	Wavenumber (cm^{-1})	Mode	Notes	Reference
$MgSO_4$	611; 619	SO_4 vibrational bending mode in meridianiite		*Wang et al. 2006; Elif Genceli et al. 2009; Ben Mabrouk et al. 2013*
$MgSO_4$	982	Main sulfate peak (aq.), symmetric SO_4 stretching		*Wang et al. 2006; Ben Mabrouk et al 2013*
$MgSO_4$	984.3; 990	Main meridianiite peak from symmetric SO_4 stretching	Hydrated $MgSO_4$: $MgSO_4$*11H_2O	*Wang et al. 2006; Elif Genceli et al. 2009; Ben Mabrouk et al. 2013*
$MgSO_4$	1059; 1095; 1116; 1133	SO_4 asymmetric stretching in meridianiite		*Wang et al. 2006; Elif Genceli et al. 2009; Ben Mabrouk et al. 2013*
Na_2SO_4	456	SO_4 bending vibrational mode in mirabilite		*Elif Genceli et al. 2009; Ben Mabrouk et al. 2013*
Na_2SO_4	613	SO_4 bending vibrational mode in mirabilite		*Elif Genceli et al. 2009; Ben Mabrouk et al. 2013*
Na_2SO_4	982	Main sulfate peak (aq.), SO_4 symmetric stretching		*Wang et al. 2006; Ben Mabrouk et al. 2013*
Na_2SO_4	990; 992	Main mirabilite peak, SO_4 symmetric stretching	Hydrated Na_2SO_4: Na_2SO_4*10H_2O	*Elif Genceli et al. 2009; Ben Mabrouk et al. 2013*
Na_2SO_4	1112	SO_4 vibrational mode in mirabilite, asymmetric SO_4 stretching		*Elif Genceli et al. 2009; Ben Mabrouk et al. 2013*
NaCl	3403, 3420, 3434, 3535	Hydrohalite peaks	Indicative of NaCl*2H_2O; peaks occur in OH-stretching band region	*Thomas et al. 2017; Baumgartner and Bakker 2010*
$NaClO_4$	461	Symmetric ClO_4 bend		*Nebgen et al. 1965*
$NaClO_4$	626	Asymmetric ClO_4 bend		*Nebgen et al. 1965*
$NaClO_4$	938	Symmetric ClO_4 stretch		*Nebgen et al. 1965*
$NaClO_4$	1095, 1139	Asymmetric ClO_4 stretch		*Nebgen et al. 1965*
$NaClO_4$	3500	Chemically bound water of hydration	Peak 3540 cm^{-1} - 3550 cm^{-1} depending on brine; $MgClO_4$ in literature, but also in $NaClO_4$	Nikolakakos and Whiteway 2015

Raman Peak Positions (Minerals):

Table A2 showcases the mineral name, chemical formula, and relevant peak positions of ices formed from six of the different endmember brine compositions used, complete with external references for Raman excitation peaks.

Table A2: Mineral Compositions and Peak Positions

Mineral	*antarcticite*	*water ice*	*bischofite*	*meridianiite*	*epsomite*	*mirabilite*	*hydrohalite*	*sodium perchlorate dihydrate*
Composition	$CaCl_2*6H_2O$	H_2O	$MgCl_2*6H_2O$	$MgSO_4*11H_2O$	$MgSO_4*7H_2O$	$Na_2SO_4*10H_2O$	$NaCl*2H_2O$	$NaClO_4*2H_2O$
Reference	Thomas et al. 2017	Wang et al. 2006; Yang et al. 2019	Thomas et al. 2017	Elif Genceli et al. 2009; Wang et al. 2006	Genceli et al. 2007; Wang et al. 2006	Elif Genceli et al. 2009; Ben Mabrouk et al. 2013	Berg 2018; Thomas et al. 2017	Nebgen 1965; Nikolakakos and Whiteway 2015
Raman Excitation Peaks (1/cm)				460	447	456		461
				611	612	613		626
				984-990	984	990		938
								1095
					1134	1112		1139
		1644						
		3216						
			3344					
	3407		3394					
	3430	3420			3425		3420	
							3434	
			3504				3535	3500

Figures 4, 5 and 6 Supplementary Tables:

Tables A3 through A9 detail spectral information for the relevant peaks in Figures 4, 5, and 6 of the text.

Table A3: Curve fit data for spectra shown in Figure 4. 785 nm red laser peaks at 200 K.

		Peak ~ 100-120 cm^{-1}			**Peak ~ 120-130 cm^{-1}**			**Peak ~ 130-140 cm^{-1}**			**Peak ~ 140-160 cm^{-1}**		
Brine	*T (K)*	*Centre*	*Width*	*Height*	*Centre*	*Width*	*Height*	*Centre*	*Width*	*Height*	*Centre*	*Width*	*Height*
UPW	200	--	--	--	--	--	--	--	--	--	--	--	--
$CaCl_2$	200	104.7	5.8	0.9	123.9	9.5	0.7	133.4	7.9	0.3	148.9	5.7	0.1
$CaCl_2$	200	--	--	--	--	--	--	--	--	--	152.7	0.7	0.1
$CaCl_2$	200	--	--	--	--	--	--	--	--	--	154.6	0.3	0.0
$MgCl_2$	200	104.9	14.1	0.5	120.7	19.6	0.2	--	--	--	150.4	11.0	0.3
$MgSO_4$	200	--	--	--	--	--	--	--	--	--	--	--	--
$MgSO_4$-NaCl	200	105.1	12.5	0.3	125.2	8.7	0.2	--	--	--	150.5	9.3	0.4
$MgSO_4$-$NaClO_4$	200	107.7	3.3	0.0	--	--	--	136.0	23.1	0.0	--	--	--
Na_2SO_4	200	--	--	--	--	--	--	--	--	--	--	--	--
Na_2SO_4-NaCl	200	103.6	13.4	0.7	129.1	5.7	0.2	--	--	--	154.3	12.7	0.3
Na_2SO_4-$NaClO_4$	200	--	--	--	--	--	--	135.8	29.5	0.0	--	--	--
NaCl	200	103.8	12.3	0.4	128.0	10.3	0.3	138.6	5.1	0.1	152.0	11.9	0.3
NaCl-$NaClO_4$	200	103.7	14.5	0.0	--	--	--	140.0	96.4	0.1	--	--	--
$NaClO_4$	200	104.0	24.8	0.0	126.5	23.2	0.0	--	--	--	156.5	14.2	0.0

		Peak ~ 160-170 cm^{-1}			**Peak ~ 170-185 cm^{-1}**			**Peak ~ 185-215 cm^{-1}**			**Peak ~ 215-222 cm^{-1}**		
Brine	*T (K)*	*Centre*	*Width*	*Height*	*Centre*	*Width*	*Height*	*Centre*	*Width*	*Height*	*Centre*	*Width*	*Height*
UPW	200	--	--	--	--	--	--	--	--	--	219.7	19.8	0.6
$CaCl_2$	200	--	--	--	--	--	--	201.3	10.9	0.3	--	--	--
$CaCl_2$	200	--	--	--	--	--	--	213.6	16.9	0.1	--	--	--
$MgCl_2$	200	167.0	8.5	0.6	179.4	9.9	0.1	202.0	17.4	0.2	218.7	13.9	0.5
$MgCl_2$	200	--	--	--	--	--	--	210.4	298.8	0.3	--	--	--
$MgSO_4$	200	--	--	--	--	--	--	--	--	--	218.4	23.7	0.1
$MgSO_4$-NaCl	200	167.9	7.9	0.7	--	--	--	200.4	18.5	0.1	219.7	13.3	0.4
$MgSO_4$-$NaClO_4$	200	--	--	--	--	--	--	207.1	20.3	0.0	221.0	11.7	0.0
Na_2SO_4	200	--	--	--	--	--	--	--	--	--	218.5	18.0	0.5
Na_2SO_4-NaCl	200	--	--	--	183.2	39.5	0.3	--	--	--	219.5	19.4	0.6
Na_2SO_4-$NaClO_4$	200	--	--	--	--	--	--	--	--	--	221.3	14.3	0.0
NaCl	200	--	--	--	179.7	17.1	0.2	--	--	--	220.2	16.5	0.6
NaCl-$NaClO_4$	200	--	--	--	--	--	--	--	--	--	220.6	17.6	0.1
$NaClO_4$	200	--	--	--	184.6	84.3	0.0	--	--	--	--	--	--

		Peak ~ 222-240 cm^{-1}			**Peak ~ 240-250 cm^{-1}**			**Peak ~ 250-280 cm^{-1}**			**Peak ~ 280-300 cm^{-1}**		
Brine	*T (K)*	*Centre*	*Width*	*Height*	*Centre*	*Width*	*Height*	*Centre*	*Width*	*Height*	*Centre*	*Width*	*Height*
UPW	200	--	--	--	--	--	--	267.6	49.0	0.1	295.8	11.4	0.1
$CaCl_2$	200	--	--	--	--	--	--	--	--	--	--	--	--
$MgCl_2$	200	--	--	--	247.6	36.4	0.3	--	--	--	298.7	15.5	0.1
$MgSO_4$	200	--	--	--	--	--	--	260.3	46.5	0.0	--	--	--
$MgSO_4$-NaCl	200	224.6	0.3	4.9	247.9	21.2	0.2	--	--	--	--	--	--
$MgSO_4$-$NaClO_4$	200	--	--	--	244.8	36.7	0.0	--	--	--	295.1	30.5	0.0
Na_2SO_4	200	--	--	--	--	--	--	--	--	--	--	--	--
Na_2SO_4-NaCl	200	--	--	--	248.6	79.8	0.4	--	--	--	297.3	22.4	0.1
Na_2SO_4-$NaClO_4$	200	--	--	--	247.4	205.0	0.0	--	--	--	--	--	--
NaCl	200	233.3	143.7	0.4	--	--	--	--	--	--	297.0	18.2	0.1
NaCl-$NaClO_4$	200	233.7	4.7	0.0	--	--	--	268.5	173.4	0.0	--	--	--
$NaClO_4$	200	--	--	--	--	--	--	278.5	121.1	0.0	--	--	--

Table A4: Curve fit data for spectra shown in Figure 5. 532 nm green laser at 200 K.

		Peak < 3000 cm^{-1}			Peak ~ 3000-3100 cm^{-1}			Peak ~3100-3120 cm^{-1}			Peak ~3120-3200 cm^{-1}		
Brine	*T (K)*	*Centre*	*Width*	*Height*	*Centre*	*Width*	*Height*	*Centre*	*Width*	*Height*	*Centre*	*Width*	*Height*
UPW	200	--	--	--	3025.6	95.7	0.1	--	--	--	3121.1	80.7	0.9
$CaCl_2$	200	--	--	--	--	--	--	3119.8	88.9	0.0	--	--	--
$MgCl_2$	200	--	--	--	--	--	--	--	--	--	3128.3	144.0	0.4
$MgSO_4$	200	2972.1	30.2	0.0	--	--	--	3118.9	60.1	0.4	3142.8	401.6	0.0
$MgSO_4$-NaCl	200	2899.6	126.1	0.0	--	--	--	3117.5	53.3	0.3	--	--	--
$MgSO_4$-$NaClO_4$	200	--	--	--	--	--	--	--	--	--	3120.5	65.1	0.1
Na_2SO_4	200	--	--	--	3007.1	120.9	0.1	--	--	--	3121.9	74.9	0.8
Na_2SO_4	200	--	--	--	3042.0	62.0	0.1	--	--	--	3126.0	122.9	0.3
Na_2SO_4-NaCl	200	2931.7	1618.5	0.0	--	--	--	--	--	--	3122.0	67.0	0.1
Na_2SO_4-$NaClO_4$	200	--	--	--	--	--	--	--	--	--	3121.8	65.7	0.4
NaCl	200	--	--	--	3064.8	151.4	0.1	--	--	--	3120.3	226.5	0.1
NaCl-$NaClO_4$	200	--	--	--	--	--	--	3119.2	51.8	0.1	3198.8	325.9	0.0
$NaClO_4$	200	--	--	--	--	--	--						

		Peak ~3200-3260 cm^{-1}			Peak ~3260-3300 cm^{-1}			Peak ~3300-3340 cm^{-1}			Peak ~3340-3400 cm^{-1}		
Brine	*T (K)*	*Centre*	*Width*	*Height*	*Centre*	*Width*	*Height*	*Centre*	*Width*	*Height*	*Centre*	*Width*	*Height*
UPW	200	3225.6	108.2	0.2	--	--	--	--	--	--	3351.8	212.3	0.4
$CaCl_2$	200	3239.6	20.9	0.0	--	--	--	3324.8	163.9	0.1	3385.5	26.3	0.3
$MgCl_2$	200	3212.1	53.2	0.2	3269.5	101.7	0.3	3325.8	53.0	0.2	--	--	--
$MgSO_4$	200	--	--	--	3269.1	325.6	0.6	--	--	--	--	--	--
$MgSO_4$-NaCl	200	3256.3	325.8	0.5	--	--	--	--	--	--	--	--	--
$MgSO_4$-$NaClO_4$	200	--	--	--	--	--	--	3322.4	431.8	0.1	--	--	--
Na_2SO_4	200	3235.4	154.8	0.4	--	--	--	3338.6	62.3	0.1	3399.8	185.2	0.4
Na_2SO_4-NaCl	200	--	--	--	--	--	--	--	--	--	3349.4	150.0	0.4
Na_2SO_4-$NaClO_4$	200	--	--	--	--	--	--	--	--	--	3345.9	449.0	0.1
NaCl	200	3221.0	131.0	0.2	--	--	--	3318.7	30.5	0.0	3373.0	245.6	0.3
NaCl-$NaClO_4$	200	--	--	--	--	--	--	--	--	--	3383.3	337.2	0.1
$NaClO_4$	200	--	--	--	--	--	--	--	--	--	--	--	--

		Peak ~3400-3420 cm^{-1}			Peak ~3420-3430 cm^{-1}			Peak ~3430-3480 cm^{-1}			Peak ~3480-3530 cm^{-1}		
Brine	*T (K)*	*Centre*	*Width*	*Height*	*Centre*	*Width*	*Height*	*Centre*	*Width*	*Height*	*Centre*	*Width*	*Height*
UPW	200	--	--	--	--	--	--	--	--	--	--	--	--
$CaCl_2$	200	3404.9	17.8	0.2	3428.6	19.0	0.7	3436.1	67.8	0.3	3483.9	100.5	0.1
$MgCl_2$	200	3410.8	109.5	0.7	--	--	--	--	--	--	3507.1	43.1	0.7
$MgSO_4$	200	--	--	--	3423.7	210.6	0.4	--	--	--	--	--	--
$MgSO_4$-NaCl	200	--	--	--	--	--	--	3431.8	195.3	0.7	--	--	--
$MgSO_4$-$NaClO_4$	200	--	--	--	--	--	--	--	--	--	--	--	--
Na_2SO_4	200	--	--	--	--	--	--	--	--	--	--	--	--
Na_2SO_4-NaCl	200	3403.2	27.1	0.1	--	--	--	3453.9	40.7	0.5	3483.9	120.1	0.3
Na_2SO_4-NaCl	200	--	--	--	--	--	--	--	--	--	3500.2	27.5	0.3
Na_2SO_4-$NaClO_4$	200	--	--	--	--	--	--	--	--	--	--	--	--
NaCl	200	--	--	--	3422.5	36.8	0.7	--	--	--	--	--	--
NaCl-$NaClO_4$	200	--	--	--	3420.6	34.5	0.2	--	--	--	--	--	--
$NaClO_4$	200	--	--	--	--	--	--	--	--	--	--	--	--

		Peak ~3530-3544 cm^{-1}			Peak ~3544-3550 cm^{-1}			Peak ~3550-3570 cm^{-1}			Peak ~3570-3610 cm^{-1}		
Brine	*T (K)*	*Centre*	*Width*	*Height*	*Centre*	*Width*	*Height*	*Centre*	*Width*	*Height*	*Centre*	*Width*	*Height*
UPW	200	--	--	--	--	--	--	--	--	--	--	--	--
$CaCl_2$	200	--	--	--	--	--	--	--	--	--	--	--	--
$MgCl_2$	200	--	--	--	--	--	--	--	--	--	--	--	--
$MgSO_4$	200	--	--	--	--	--	--	--	--	--	--	--	--
$MgSO_4$-NaCl	200	--	--	--	--	--	--	--	--	--	--	--	--
$MgSO_4$-$NaClO_4$	200	3543.7	0.6	-0.8	3545.4	40.4	0.5	3554.9	13.8	0.5	3597.9	38.1	0.1
Na_2SO_4	200	--	--	--	--	--	--	--	--	--	--	--	--
Na_2SO_4-NaCl	200	--	--	--	--	--	--	--	--	--	--	--	--
Na_2SO_4-$NaClO_4$	200	3534.0	27.1	0.1	--	--	--	3553.5	18.3	0.9	--	--	--
NaCl	200	3541.5	22.5	0.2	--	--	--	--	--	--	--	--	--
NaCl-$NaClO_4$	200	3534.8	30.3	0.2	--	--	--	3553.2	19.2	0.8	3597.7	33.4	0.1
$NaClO_4$	200	--	--	--	3546.5	41.1	0.5	3553.5	13.9	0.5	3601.5	31.5	0.0

Table A5. Curve fit data for spectra shown in Figure 5. 532 nm green laser at 295 K.

		Peak < 3250 cm^{-1}			Peak ~3250-3300 cm^{-1}			Peak ~3300-3350 cm^{-1}			Peak ~3350-3440 cm^{-1}		
Brine	*T (K)*	*Centre*	*Width*	*Height*	*Centre*	*Width*	*Height*	*Centre*	*Width*	*Height*	*Centre*	*Width*	*Height*
UPW	295	3218.7	229.0	0.6	--	--	--	--	--	--	3438.1	263.0	0.9
$CaCl_2$	295	--	--	--	--	--	--	3338.0	274.0	0.4	3432.8	140.5	0.5
$MgCl_2$	295	2427.6	34.3	0.2	3258.7	232.6	0.4	--	--	--	3408.6	166.4	0.5
$MgSO_4$	295	--	--	--	3265.8	270.4	0.6	--	--	--	--	--	--
$MgSO_4$-NaCl	295	--	--	--	3273.5	254.5	0.5	--	--	--	--	--	--
$MgSO_4$-$NaClO_4$	295	--	--	--	3264.7	218.8	0.2	--	--	--	--	--	--
Na_2SO_4	295	3248.2	242.8	0.5	--	--	--	--	--	--	--	--	--
Na_2SO_4-NaCl	295	--	--	--	3254.5	220.7	0.4	--	--	--	--	--	--
Na_2SO_4-$NaClO_4$	295	--	--	--	3275.4	225.2	0.3	--	--	--	--	--	--
NaCl	295	--	--	--	3276.3	227.9	0.3	--	--	--	--	--	--
NaCl-$NaClO_4$	295	--	--	--	3288.5	218.9	0.2	--	--	--	--	--	--
$NaClO_4$	295	--	--	--	--	--	--	3314.8	196.9	0.1	3410.5	98.2	0.1

		Peak ~3440-3550 cm^{-1}			Peak ~3550-3600 cm^{-1}			Peak ~3600-3650 cm^{-1}		
Brine	*T (K)*	*Centre*	*Width*	*Height*	*Centre*	*Width*	*Height*	*Centre*	*Width*	*Height*
UPW	295	--	--	--	--	--	--	3621.6	89.9	0.1
$CaCl_2$	295	3519.4	184.9	0.3	--	--	--	--	--	--
$MgCl_2$	295	3498.0	202.9	0.4	--	--	--	--	--	--
$MgSO_4$	295	3443.6	196.7	0.7	3575.1	142.6	0.2	--	--	--
$MgSO_4$-NaCl	295	3453.8	196.6	0.8	--	--	--	3603.3	127.0	0.1
$MgSO_4$-$NaClO_4$	295	3455.6	214.4	0.5	3579.5	120.0	0.4	--	--	--
Na_2SO_4	295	3450.3	236.0	0.8	--	--	--	3613.0	99.3	0.1
Na_2SO_4-NaCl	295	3453.7	220.2	0.9	--	--	--	3620.1	93.1	0.1
Na_2SO_4-$NaClO_4$	295	3459.9	203.1	0.6	3584.6	115.3	0.4	--	--	--
NaCl	295	3456.4	195.1	0.8	--	--	--	3608.3	122.8	0.1
NaCl-$NaClO_4$	295	3455.3	188.0	0.7	3578.2	123.5	0.4	--	--	--
$NaClO_4$	295	3474.3	85.3	0.1	3551.1	91.1	0.4	3610.4	72.2	0.2

Table A6: Curve fit data for spectra shown Figure 6. 785 nm red laser peaks at 200 K

		Peaks 450-470 cm^{-1}			**Peaks 470-550 cm^{-1}**			**Peaks 600-635 cm^{-1}**			**Peaks 635-700 cm^{-1}**		
Brine	*T (K)*	*Centre*	*Width*	*Height*	*Centre*	*Width*	*Height*	*Centre*	*Width*	*Height*	*Centre*	*Width*	*Height*
UPW	200	--	--	--	--	--	--	--	--	--	--	--	--
$CaCl_2$	200	--	--	--	519.9	31.4	0.5	--	--	--	683.6	33.2	0.1
$MgCl_2$	200	--	--	--	--	--	--	--	--	--	--	--	--
$MgSO_4$	200	--	--	--	--	--	--	--	--	--	--	--	--
$MgSO_4$-NaCl	200	460.9	171.6	0.1	--	--	--	622.0	83.2	0.1	--	--	--
$MgSO_4$-$NaClO_4$	200	460.7	16.8	0.1	--	--	--	628.2	10.7	0.1	636.4	9.0	0.1
Na_2SO_4	200	--	--	--	--	--	--	610.2	25.4	0.0	--	--	--
Na_2SO_4-NaCl	200	455.3	13.1	0.1	503.9	30.8	0.0	--	--	--	635.4	55.2	0.0
Na_2SO_4-NaCl	200	--	--	--	576.3	17.1	0.0	--	--	--	--	--	--
Na_2SO_4-$NaClO_4$	200	460.2	25.5	0.1	--	--	--	--	--	--	635.3	13.2	0.2
NaCl	200	--	--	--	568.0	95.3	0.1	--	--	--	642.9	53.9	0.1
NaCl-$NaClO_4$	200	460.5	19.0	0.1	--	--	--	--	--	--	635.4	11.5	0.2
$NaClO_4$	200	453.9	6.8	0.1	470.7	19.5	0.1	632.7	24.9	0.0	639.0	8.9	0.0

		Peaks 700-800 cm^{-1}			**Peaks 800-930 cm^{-1}**			**Peaks 930-950 cm^{-1}**			**Peaks 950-1050 cm^{-1}**		
Brine	*T (K)*	*Centre*	*Width*	*Height*	*Centre*	*Width*	*Height*	*Centre*	*Width*	*Height*	*Centre*	*Width*	*Height*
UPW	200	--	--	--	--	--	--	--	--	--	--	--	--
$CaCl_2$	200	711.9	19.6	0.1	--	--	--	--	--	--	--	--	--
$MgCl_2$	200	--	--	--	--	--	--	--	--	--	--	--	--
$MgSO_4$	200	--	--	--	--	--	--	--	--	--	--	--	--
$MgSO_4$-NaCl	200	750.8	184.7	0.1	--	--	--	940.9	13.3	0.1	991.7	5.5	0.5
$MgSO_4$-$NaClO_4$	200	--	--	--	--	--	--	931.8	18.0	0.2	986.5	11.0	0.0
$MgSO_4$-$NaClO_4$	200	--	--	--	--	--	--	937.3	6.6	0.9	--	--	--
Na_2SO_4	200	796.8	22.4	0.0	859.4	0.3	0.0	--	--	--	991.4	4.5	0.9
Na_2SO_4-NaCl	200	--	--	--	819.6	94.7	0.0	--	--	--	983.3	7.3	0.0
Na_2SO_4-NaCl	200	--	--	--	--	--	--	--	--	--	991.8	5.5	0.2
Na_2SO_4-$NaClO_4$	200	--	--	--	--	--	--	937.1	7.1	1.0	--	--	--
NaCl	200	785.2	267.6	0.1	--	--	--	--	--	--	--	--	--
NaCl-$NaClO_4$	200	--	--	--	--	--	--	937.1	6.9	1.0	--	--	--
$NaClO_4$	200	--	--	--	--	--	--	946.6	5.7	1.0	--	--	--

		Peaks 1050-1200 cm^{-1}			**Peaks 1200-1550 cm^{-1}**			**Peaks 1550-1650 cm^{-1}**			**Peaks 1650-1700 cm^{-1}**		
Brine	*T (K)*	*Centre*	*Width*	*Height*	*Centre*	*Width*	*Height*	*Centre*	*Width*	*Height*	*Centre*	*Width*	*Height*
UPW	200	--	--	--	--	--	--	--	--	--	--	--	--
$CaCl_2$	200	--	--	--	--	--	--	--	--	--	1661.6	15.5	0.1
$MgCl_2$	200	--	--	--	--	--	--	1579.1	718.9	0.2	--	--	--
$MgSO_4$	200	--	--	--	--	--	--	--	--	--	--	--	--
$MgSO_4$-NaCl	200	--	--	--	--	--	--	1625.8	749.1	0.1	--	--	--
$MgSO_4$-$NaClO_4$	200	1106.1	36.8	0.1	--	--	--	1618.6	15.0	0.0	--	--	--
Na_2SO_4	200	1090.3	85.1	0.0	1349.9	489.4	0.0	--	--	--	--	--	--
Na_2SO_4-NaCl	200	1095.1	79.7	0.0	1285.0	81.6	0.0	1646.9	8.6	0.1	1666.0	10.7	0.1
Na_2SO_4-$NaClO_4$	200	1108.5	80.0	0.1	--	--	--	1617.8	40.0	0.1	--	--	--
NaCl	200	1075.9	108.1	0.0	--	--	--	--	--	--	1665.3	8.2	0.1
NaCl-$NaClO_4$	200	1104.7	35.0	0.1	--	--	--	1617.4	14.0	0.0	--	--	--
$NaClO_4$	200	1107.3	43.6	0.0	--	--	--	--	--	--	--	--	--

Table A7: Curve fit data for spectra shown in Figure 6. 785 nm red laser at 295 K.

		Peaks 400-500 cm^{-1}			Peaks 500-640 cm^{-1}			Peaks 640-900 cm^{-1}			Peaks 900-950 cm^{-1}		
Brine	*T (K)*	*Centre*	*Width*	*Height*	*Centre*	*Width*	*Height*	*Centre*	*Width*	*Height*	*Centre*	*Width*	*Height*
UPW	295	--	--	--	--	--	--	764.8	175.8	0.0	--	--	--
$CaCl_2$	295	--	--	--	--	--	--	--	--	--	--	--	--
$MgCl_2$	295	--	--	--	--	--	--	--	--	--	--	--	--
$MgSO_4$	295	449.2	41.5	0.1	615.1	47.2	0.0	--	--	--	--	--	--
$MgSO_4$-NaCl	295	447.5	62.9	0.1	623.0	137.8	0.0	--	--	--	936.0	8.2	0.0
$MgSO_4$-$NaClO_4$	295	463.0	25.5	0.1	631.2	22.0	0.1	--	--	--	938.2	12.1	1.0
Na_2SO_4	295	447.7	51.7	0.1	618.3	97.1	0.0	--	--	--	--	--	--
Na_2SO_4-NaCl	295	445.4	111.6	0.1	615.2	135.0	0.1	778.0	145.9	0.0	--	--	--
Na_2SO_4-$NaClO_4$	295	462.1	35.9	0.1	630.8	29.0	0.1	--	--	--	938.3	12.0	1.0
NaCl	295	--	--	--	--	--	--	--	--	--	--	--	--
NaCl-$NaClO_4$	295	462.6	28.6	0.1	631.2	23.0	0.1	--	--	--	939.0	12.7	1.0
$NaClO_4$	295	463.0	28.0	0.1	632.0	21.9	0.1	--	--	--	941.1	14.5	1.0
		Peaks 950-1000 cm^{-1}			**Peaks 1000-1300 cm^{-1}**			**Peaks 1300-1600 cm^{-1}**			**Peaks 1600-1700 cm^{-1}**		
Brine	*T (K)*	*Centre*	*Width*	*Height*	*Centre*	*Width*	*Height*	*Centre*	*Width*	*Height*	*Centre*	*Width*	*Height*
UPW	295	--	--	--	--	--	--	1302.0	182.8	0.0	1619.1	597.7	0.1
$CaCl_2$	295	--	--	--	--	--	--	--	--	--	1649.0	151.8	0.1
$MgCl_2$	295	--	--	--	--	--	--	--	--	--	1645.7	149.3	0.1
$MgSO_4$	295	983.6	9.8	1.0	1116.6	66.6	0.0	--	--	--	--	--	--
$MgSO_4$-NaCl	295	983.4	9.4	1.0	1120.2	63.4	0.0	--	--	--	--	--	--
$MgSO_4$-$NaClO_4$	295	983.5	7.0	0.0	1111.9	95.1	0.0	--	--	--	--	--	--
Na_2SO_4	295	982.2	8.0	1.0	1116.3	63.3	0.0	1309.3	165.0	0.0	--	--	--
Na_2SO_4-NaCl	295	982.7	8.5	1.0	1120.0	80.5	0.0	--	--	--	1613.0	691.6	0.1
Na_2SO_4-$NaClO_4$	295	982.7	8.8	0.1	1113.3	75.2	0.0	--	--	--	--	--	--
NaCl	295	--	--	--	1046.1	34.9	0.0	--	--	--	1642.3	136.5	0.1
NaCl-$NaClO_4$	295	--	--	--	1115.6	75.6	0.0	--	--	--	--	--	--
$NaClO_4$	295	--	--	--	1113.8	109.0	0.1	--	--	--	--	--	--

Table A8: Curve fit data for spectra shown in Figure 6. 532 nm green laser at 200 K.

		Peaks 400-600 cm^{-1}			Peaks 600-800 cm^{-1}			Peaks 800-950 cm^{-1}		
Brine	*T (K)*	*Centre*	*Width*	*Height*	*Centre*	*Width*	*Height*	*Centre*	*Width*	*Height*
UPW	200	--	--	--	--	--	--	--	--	--
$CaCl_2$	200	518.5	48.7	0.1	692.0	68.7	0.0	--	--	--
$MgCl_2$	200	--	--	--	--	--	--	--	--	--
$MgSO_4$	200	--	--	--	--	--	--	--	--	--
$MgSO_4$-NaCl	200	--	--	--	--	--	--	--	--	--
$MgSO_4$-$NaClO_4$	200	461.1	26.7	0.1	634.9	14.4	0.2	935.5	13.0	0.7
Na_2SO_4	200	--	--	--	--	--	--	--	--	--
Na_2SO_4-NaCl	200	--	--	--	--	--	--	--	--	--
Na_2SO_4-$NaClO_4$	200	459.1	21.4	0.1	632.4	15.6	0.1	896.1	9.2	0.0
NaCl	200	--	--	--	--	--	--	--	--	--
NaCl-$NaClO_4$	200	458.5	60.0	0.2	633.7	20.0	0.2	934.1	12.7	0.8
$NaClO_4$	200	457.1	31.9	0.1	632.6	15.1	0.1	934.0	12.6	0.8
		Peaks 950-1000 cm^{-1}			**Peaks 1000-1150 cm^{-1}**			**Peaks 1150-1700 cm^{-1}**		
Brine	*T (K)*	*Centre*	*Width*	*Height*	*Centre*	*Width*	*Height*	*Centre*	*Width*	*Height*
UPW	200	--	--	--	--	--	--	--	--	--
$CaCl_2$	200	--	--	--	--	--	--	1658.3	31.0	0.0
$MgCl_2$	200	--	--	--	--	--	--	--	--	--
$MgSO_4$	200	983.9	20.4	0.6	--	--	--	--	--	--
$MgSO_4$-NaCl	200	981.7	15.7	0.3	--	--	--	--	--	--
$MgSO_4$-$NaClO_4$	200	986.0	10.0	0.0	1100.6	27.7	0.1	1614.5	26.4	0.1
Na_2SO_4	200	990.2	9.0	0.1	--	--	--	--	--	--
Na_2SO_4-NaCl	200	--	--	--	--	--	--	1665.0	61.5	0.0
Na_2SO_4-$NaClO_4$	200	989.0	8.4	0.0	1104.8	46.8	0.1	1617.4	18.7	0.0
NaCl	200	--	--	--	--	--	--	1660.9	23.4	0.0
NaCl-$NaClO_4$	200	--	--	--	1099.0	27.4	0.1	1615.3	17.3	0.1
$NaClO_4$	200	--	--	--	1100.6	35.5	0.1	1614.7	18.5	0.0

Table A9: Curve fit data for spectra shown in Figure 6. 532 nm green laser at 295 K.

		Peaks 400-600 cm^{-1}			**Peaks 600-800 cm^{-1}**			**Peaks 800-950 cm^{-1}**		
Brine	*T (K)*	*Centre*	*Width*	*Height*	*Centre*	*Width*	*Height*	*Centre*	*Width*	*Height*
UPW	295	--	--	--	--	--	--	--	--	--
$CaCl_2$	295	--	--	--	--	--	--	--	--	--
$MgCl_2$	295	471.7	5.1	0.1	--	--	--	--	--	--
$MgSO_4$	295	449.2	43.2	0.1	615.6	27.2	0.0	--	--	--
$MgSO_4$-NaCl	295	--	--	--	612.4	32.3	0.0	--	--	--
$MgSO_4$-$NaClO_4$	295	463.1	31.9	0.2	630.7	26.2	0.2	937.4	16.2	1.0
Na_2SO_4	295	--	--	--	--	--	--	--	--	--
Na_2SO_4-NaCl	295	--	--	--	--	--	--	--	--	--
Na_2SO_4-$NaClO_4$	295	461.4	46.3	0.2	629.7	51.0	0.2	936.6	16.3	1.0
NaCl	295	--	--	--	--	--	--	--	--	--
NaCl-$NaClO_4$	295	461.6	35.5	0.2	630.4	33.2	0.2	937.0	16.6	0.9
$NaClO_4$	295	457.1	31.9	0.1	630.0	24.7	0.2	938.7	17.8	1.0

		Peaks 950-1000 cm^{-1}			**Peaks 1000-1150 cm^{-1}**			**Peaks 1150-1700 cm^{-1}**		
Brine	*T (K)*	*Centre*	*Width*	*Height*	*Centre*	*Width*	*Height*	*Centre*	*Width*	*Height*
UPW	295	--	--	--	--	--	--	1639.6	124.5	0.0
$CaCl_2$	295	--	--	--	--	--	--	1642.8	68.5	0.0
$MgCl_2$	295	--	--	--	--	--	--	1662.3	342.8	0.1
$MgSO_4$	295	982.3	14.7	0.5	1116.7	106.6	0.0	--	--	--
$MgSO_4$-NaCl	295	981.6	13.6	0.2	1108.9	66.7	0.0	1658.0	191.3	0.0
$MgSO_4$-$NaClO_4$	295	991.3	0.9	0.1	1113.2	84.0	0.1	1638.2	68.3	0.0
Na_2SO_4	295	981.0	13.7	0.3	1119.3	113.8	0.0	--	--	--
Na_2SO_4-NaCl	295	981.0	13.2	0.1	1112.1	114.2	0.0	1643.9	75.2	0.0
Na_2SO_4-$NaClO_4$	295	981.7	13.3	0.1	1112.5	83.4	0.1	1641.8	50.9	0.0
NaCl	295	--	--	--	--	--	--	1651.2	116.5	0.0
NaCl-$NaClO_4$	295	--	--	--	1110.1	69.8	0.1	1646.3	94.8	0.0
$NaClO_4$	295	--	--	--	1114.0	89.0	0.1	1632.3	45.7	0.0

Ices:

The following twenty-four figures detail stacked plots showcasing the effects of temperature on seven endmember and five mixed-composition Mars-analogue brines using both 532 nm (green) and 785 nm (red) laser wavelengths. Each brine has one figure with lines and labels denoting important peak positions (see Table A1), and a second figure of the same spectra with no lines or labels included. Lines have been color-coded as noted in figure captions on the former figures to denote the responsible brine.

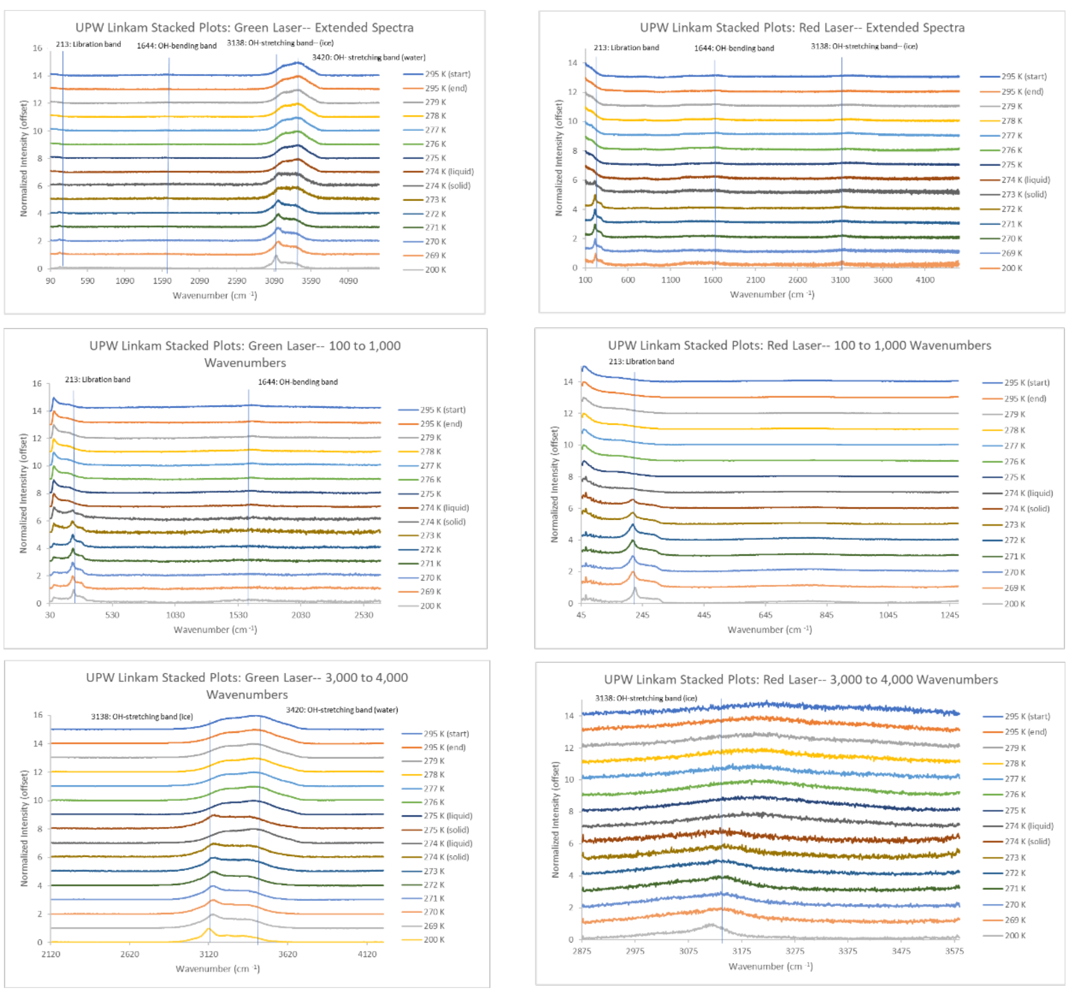

Figure A1: Ultrapure water stacked plots (532 nm and 785 nm lasers), lines and labels included to denote important peaks of ultrapure water (light blue).

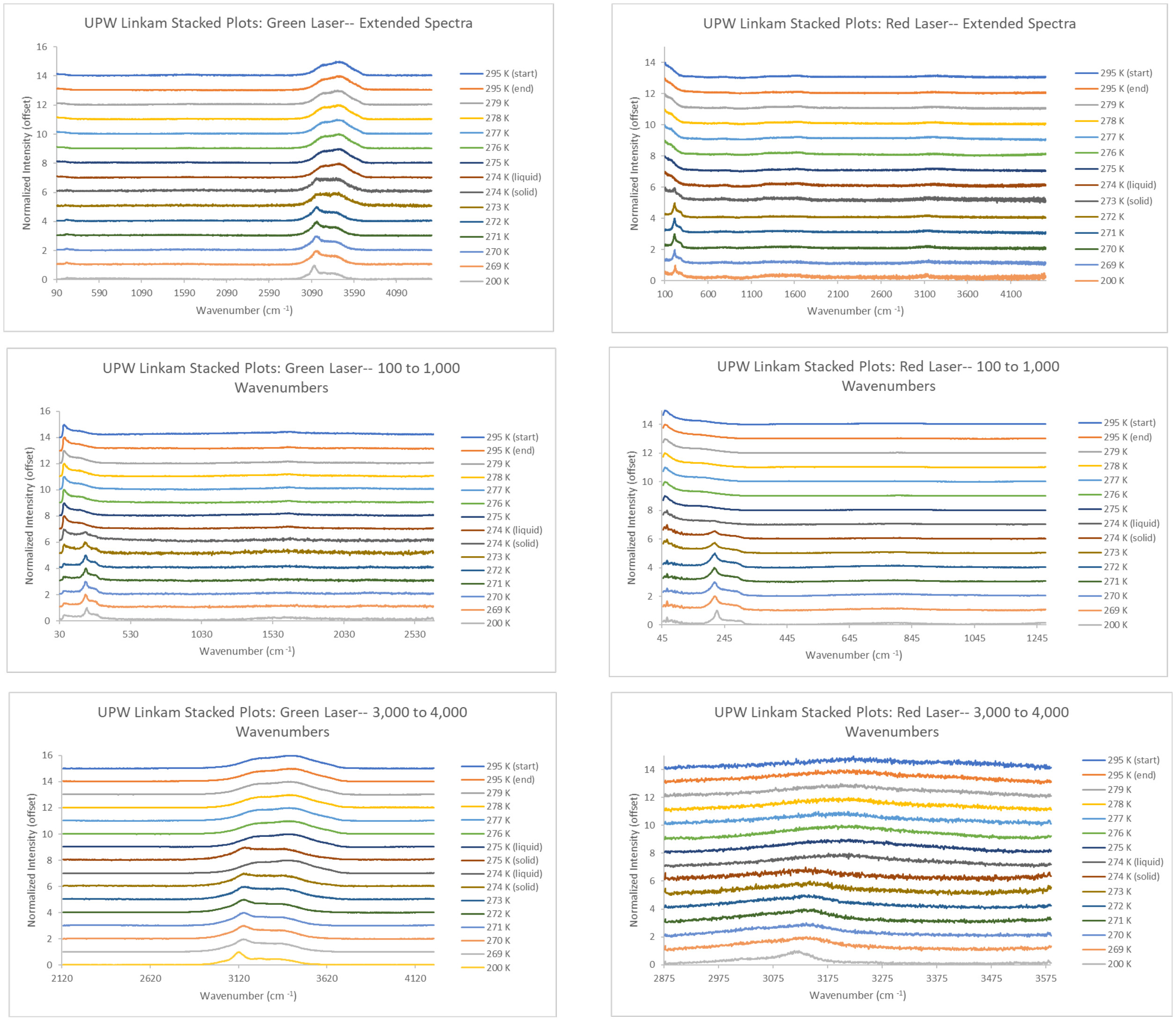

Figure A2: Ultrapure water stacked plots (532 nm and 785 nm lasers), lines and labels not included.

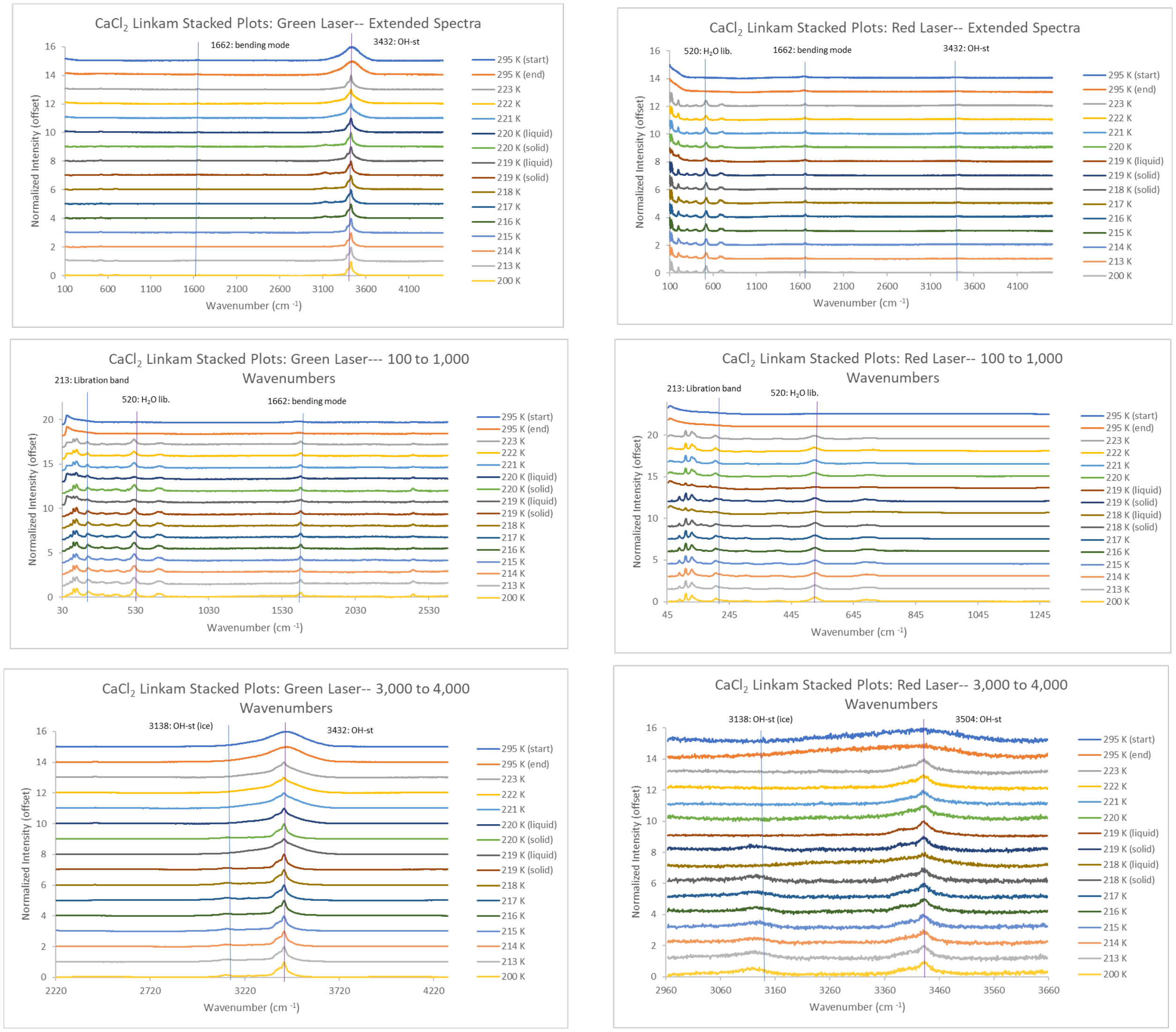

Figure A3: $CaCl_2$ stacked plots (532 nm and 785 nm lasers), lines and labels included to denote important peaks of ultrapure water (light blue) and $CaCl_2$ (purple).

Figure A4: $CaCl_2$ stacked plots (532 nm and 785 nm lasers), lines and labels not included.

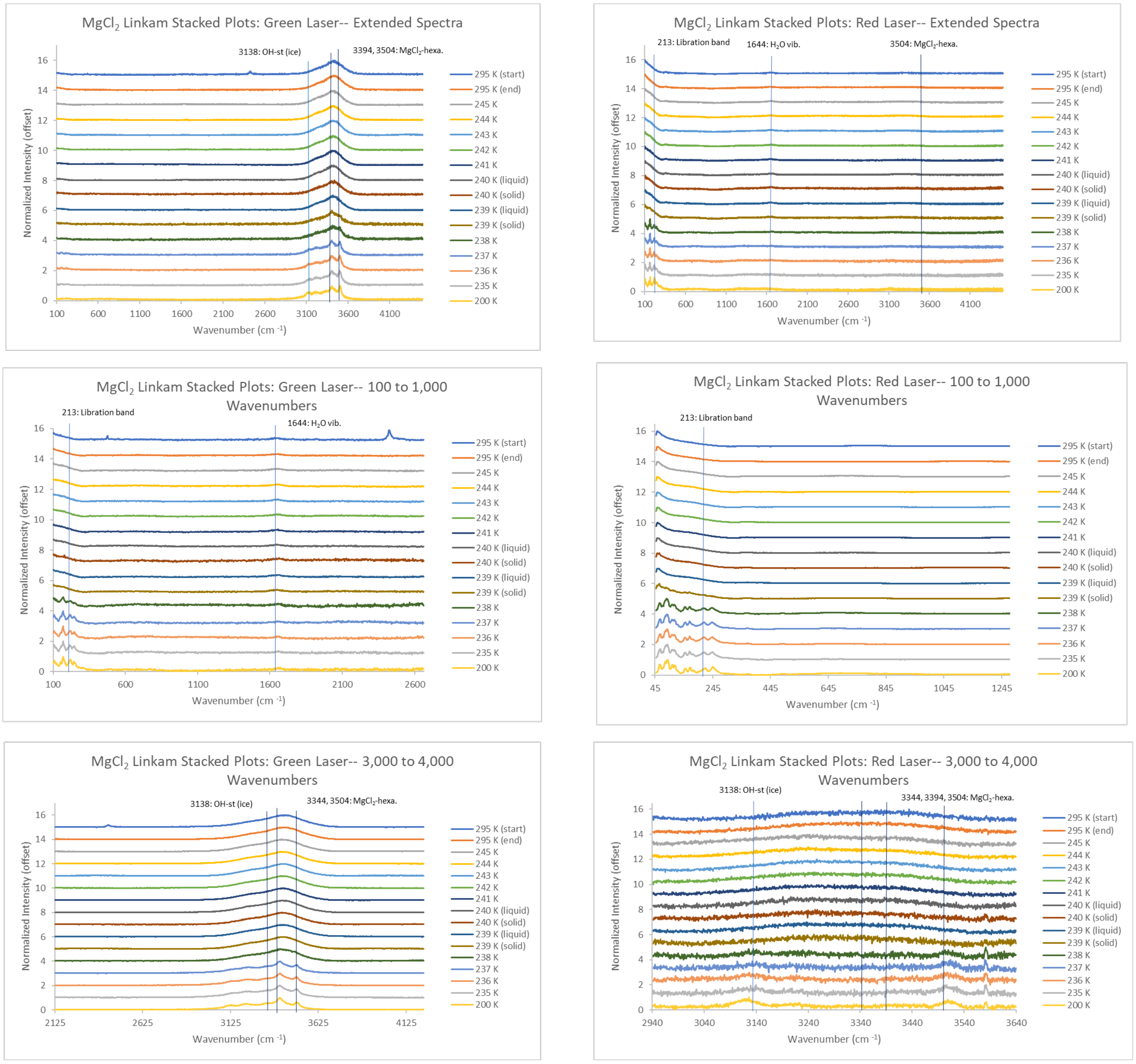

Figure A5: $MgCl_2$ stacked plots (532 nm and 785 nm lasers), lines and labels included to denote important peaks of ultrapure water (light blue) and $MgCl_2$ (navy blue).

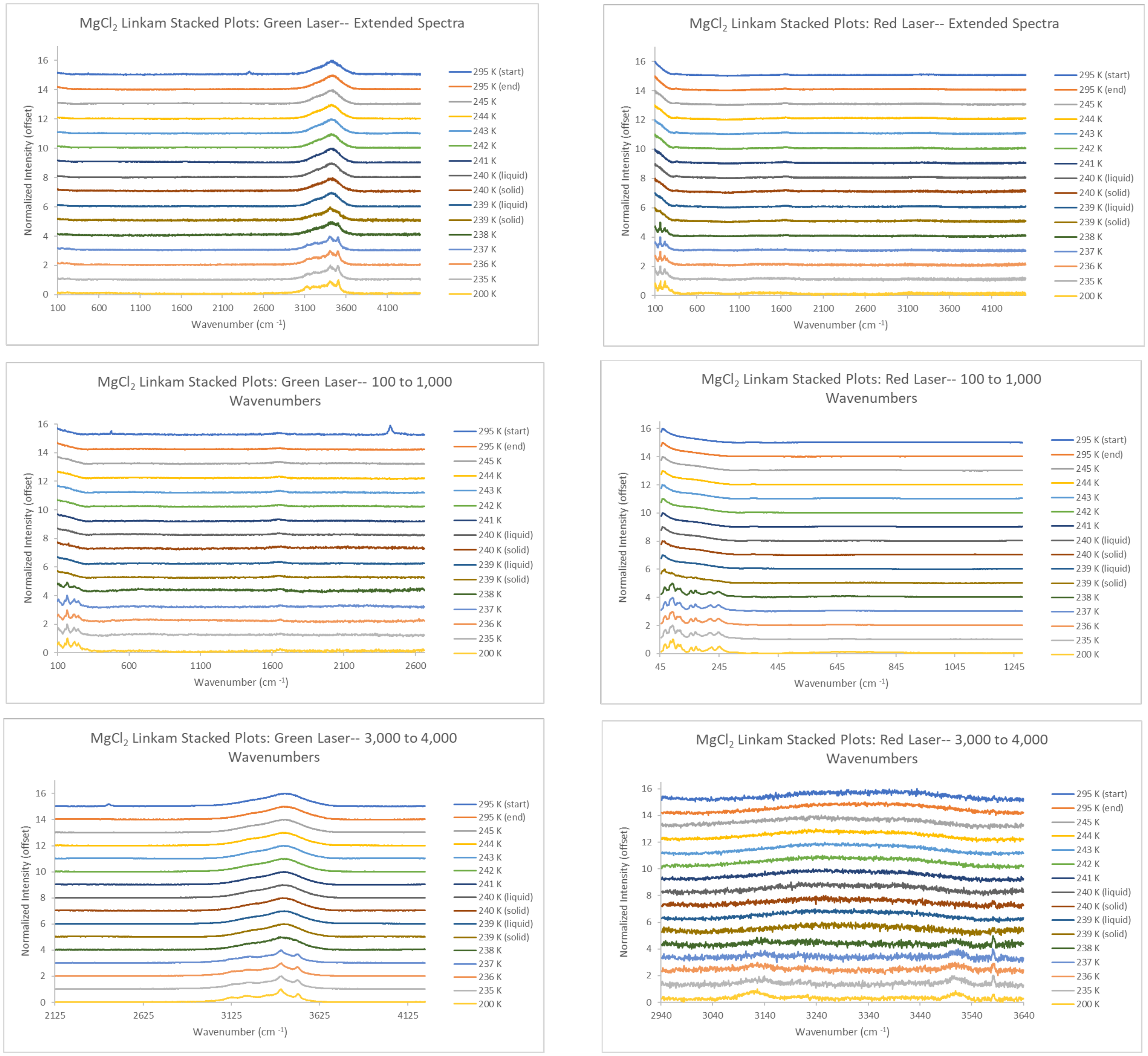

Figure A6: $MgCl_2$ stacked plots (532 nm and 785 nm lasers), lines and labels not included.

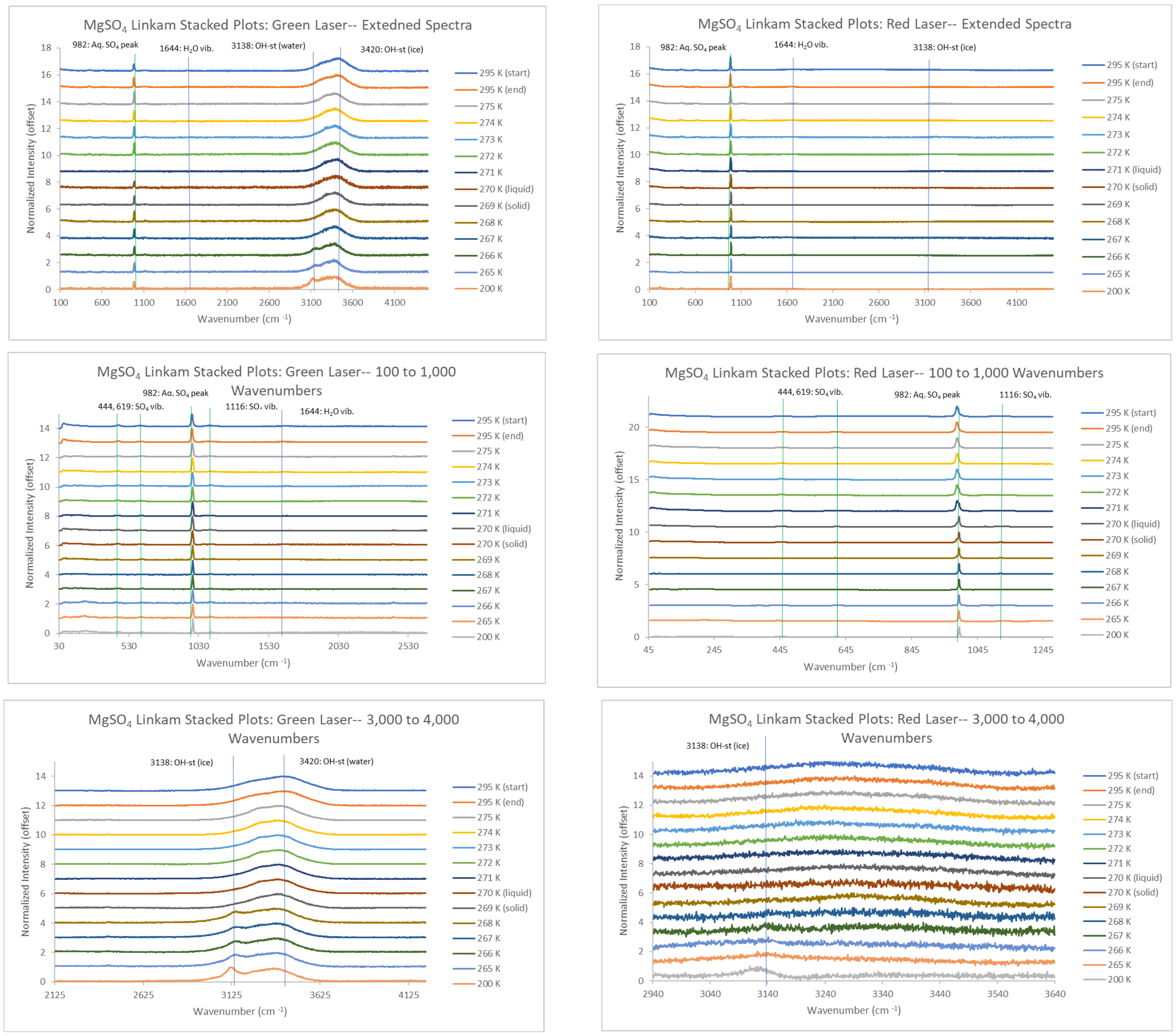

Figure A7: $MgSO_4$ stacked plots (532 nm and 785 nm lasers), lines and labels included to denote important peaks of ultrapure water (light blue) and $MgSO_4$ (dark green).

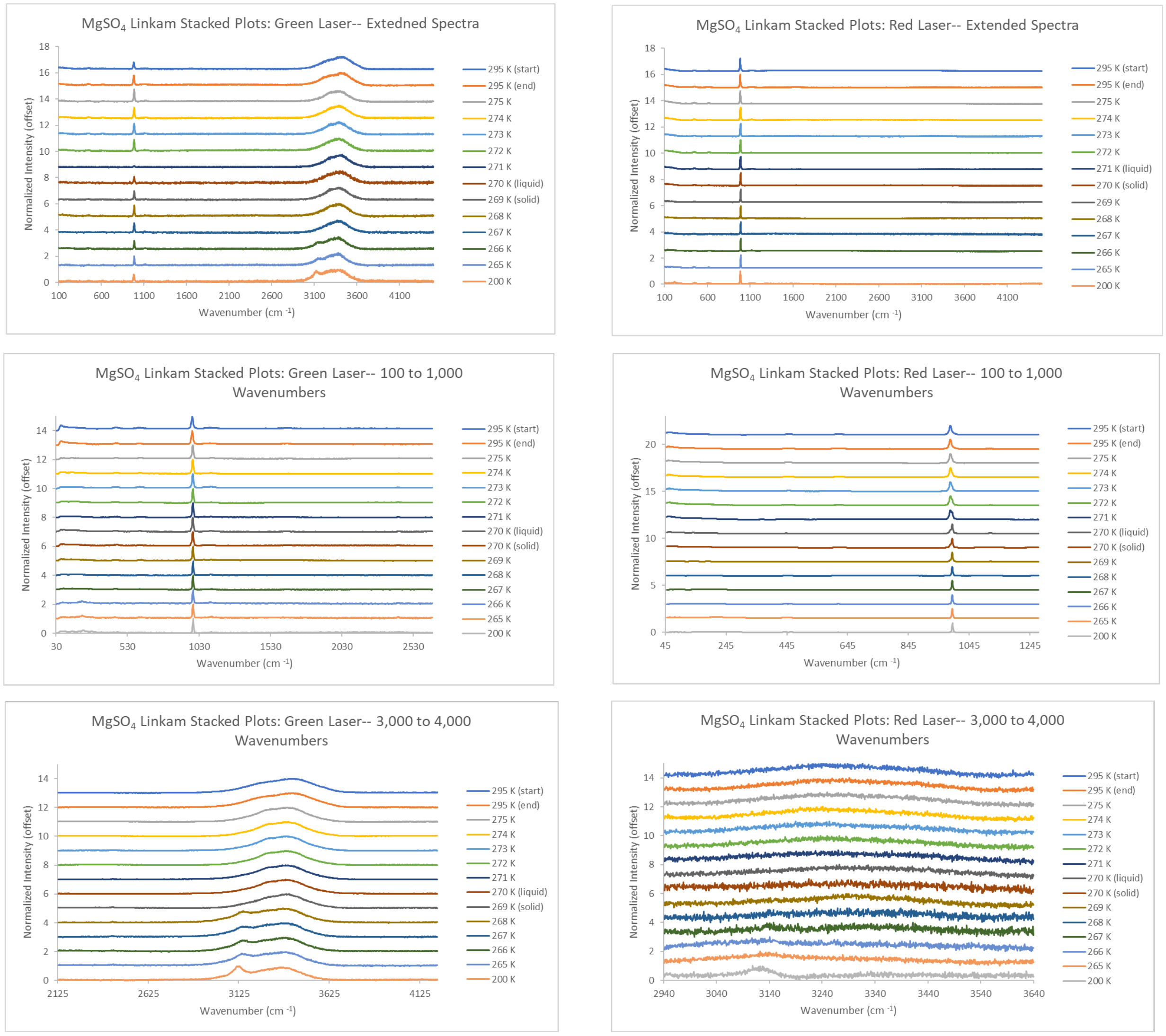

Figure A8: $MgSO_4$ stacked plots (532 nm and 785 nm lasers), lines and labels not included.

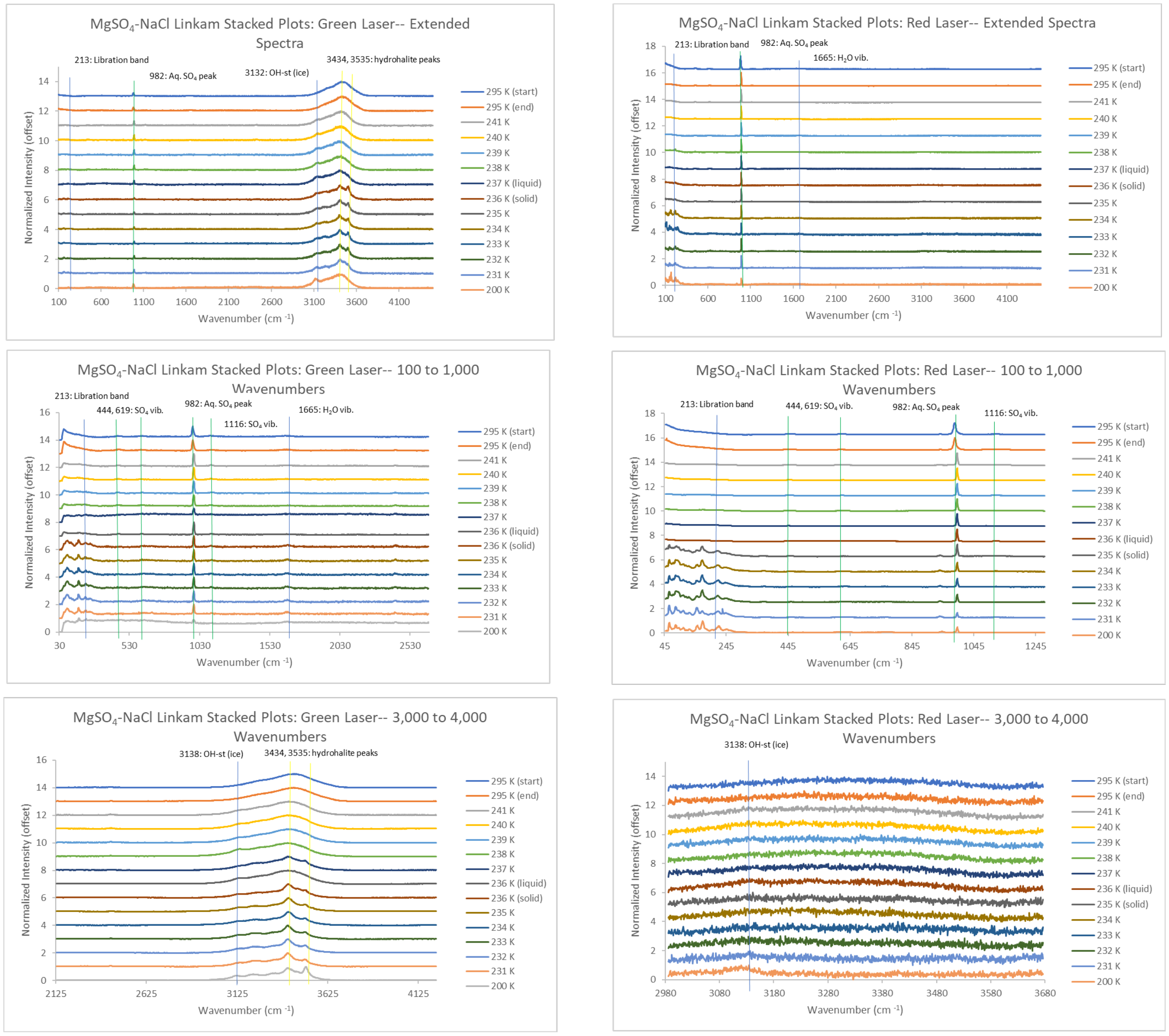

Figure A9: $MgSO_4$-NaCl stacked plots (532 nm and 785 nm lasers), lines and labels included to denote important peaks of ultrapure water (light blue), $MgSO_4$ (dark green), and NaCl (yellow).

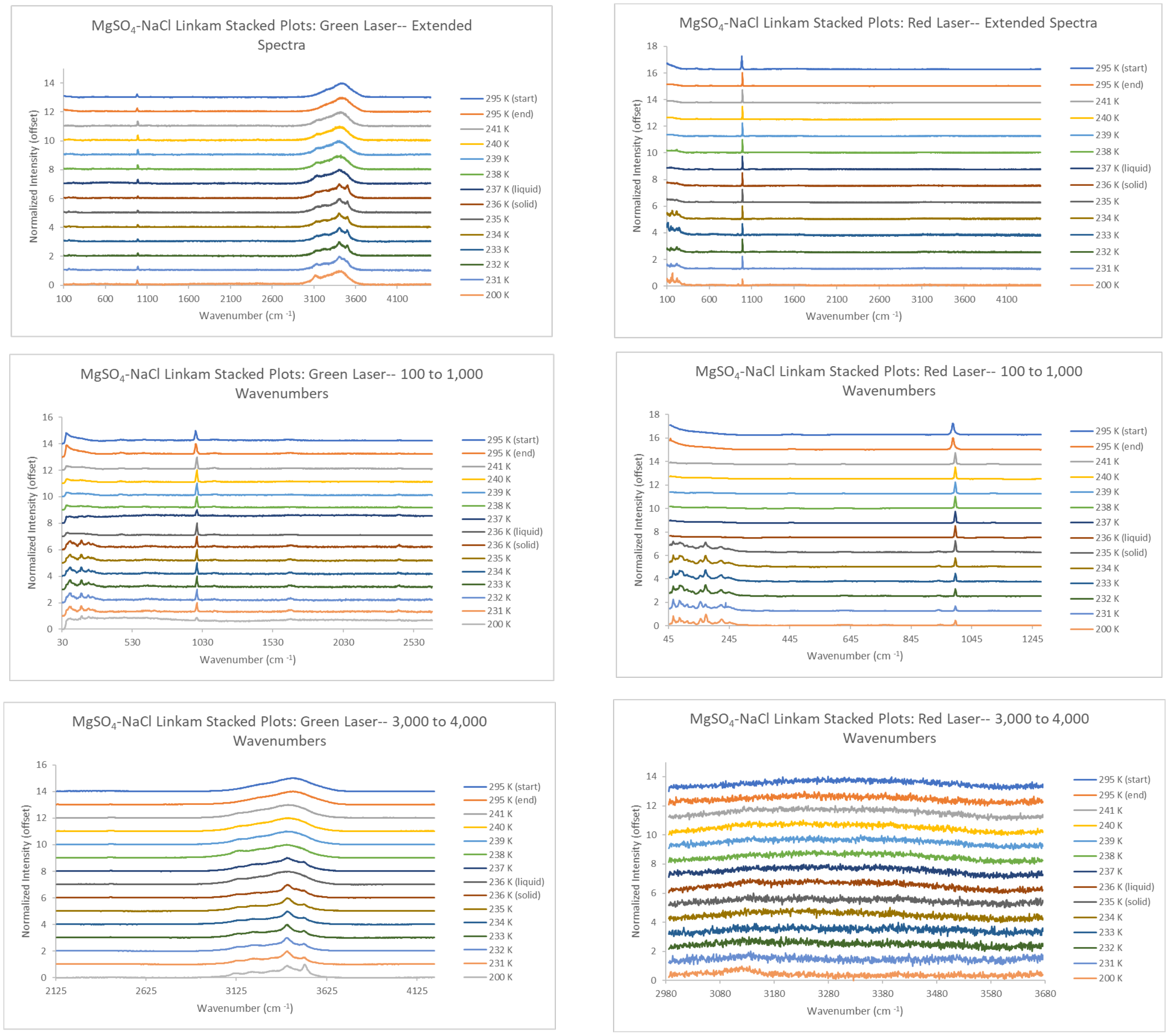

Figure A10: $MgSO_4$-NaCl stacked plots (532 nm and 785 nm lasers), lines and labels not included.

Figure A11: $MgSO_4$-$NaClO_4$ stacked plots (532 nm and 785 nm lasers), lines and labels included to denote important peaks of ultrapure water (light blue), $MgSO_4$ (dark green), and $NaClO_4$ (red).

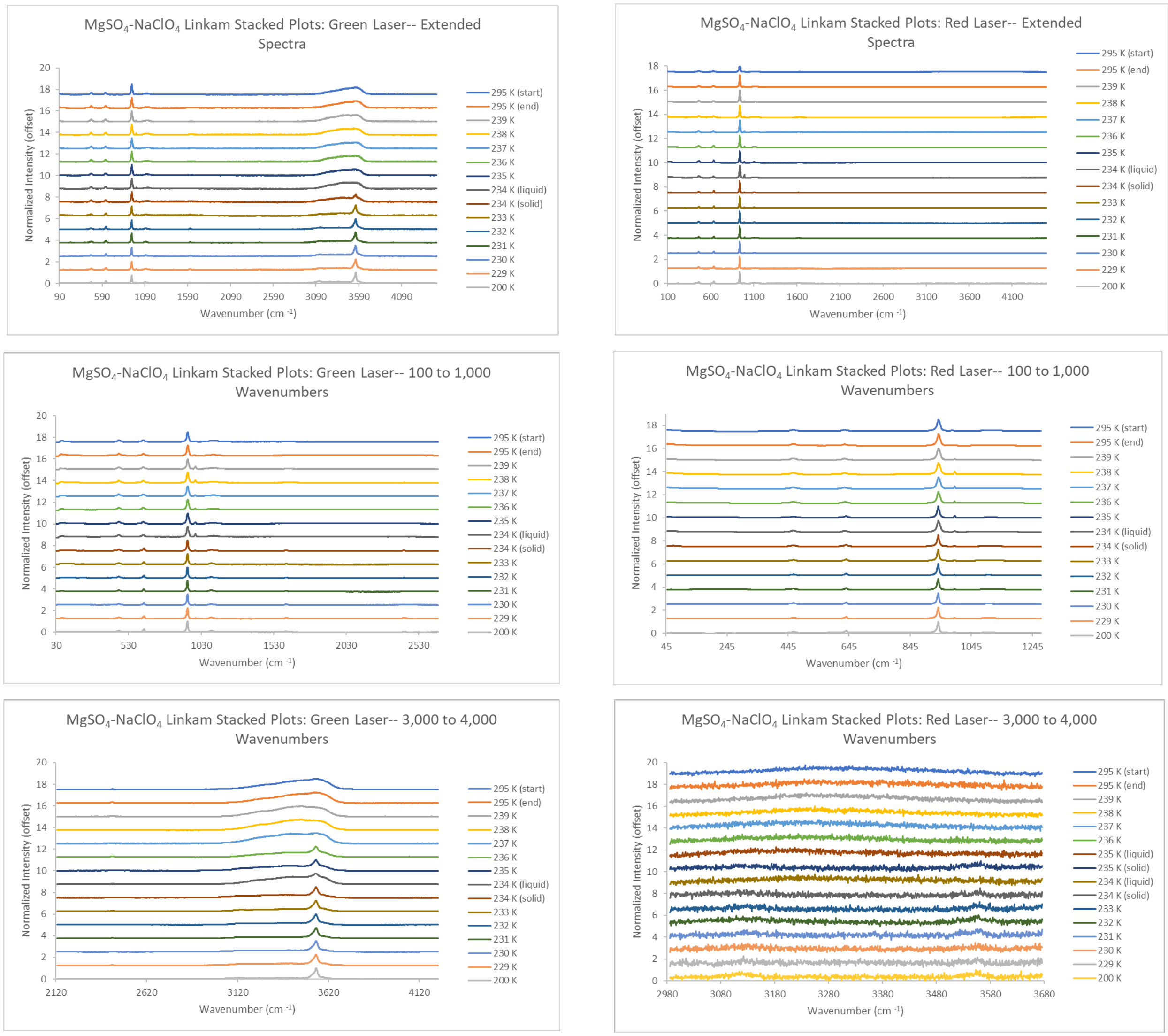

Figure A12: $MgSO_4$-$NaClO_4$ stacked plots (532 nm and 785 nm lasers), lines and labels not included.

Figure A13: Na_2SO_4 stacked plots (532 nm and 785 nm lasers), lines and labels included to denote important peaks of ultrapure water (light blue) and Na_2SO_4 (light green).

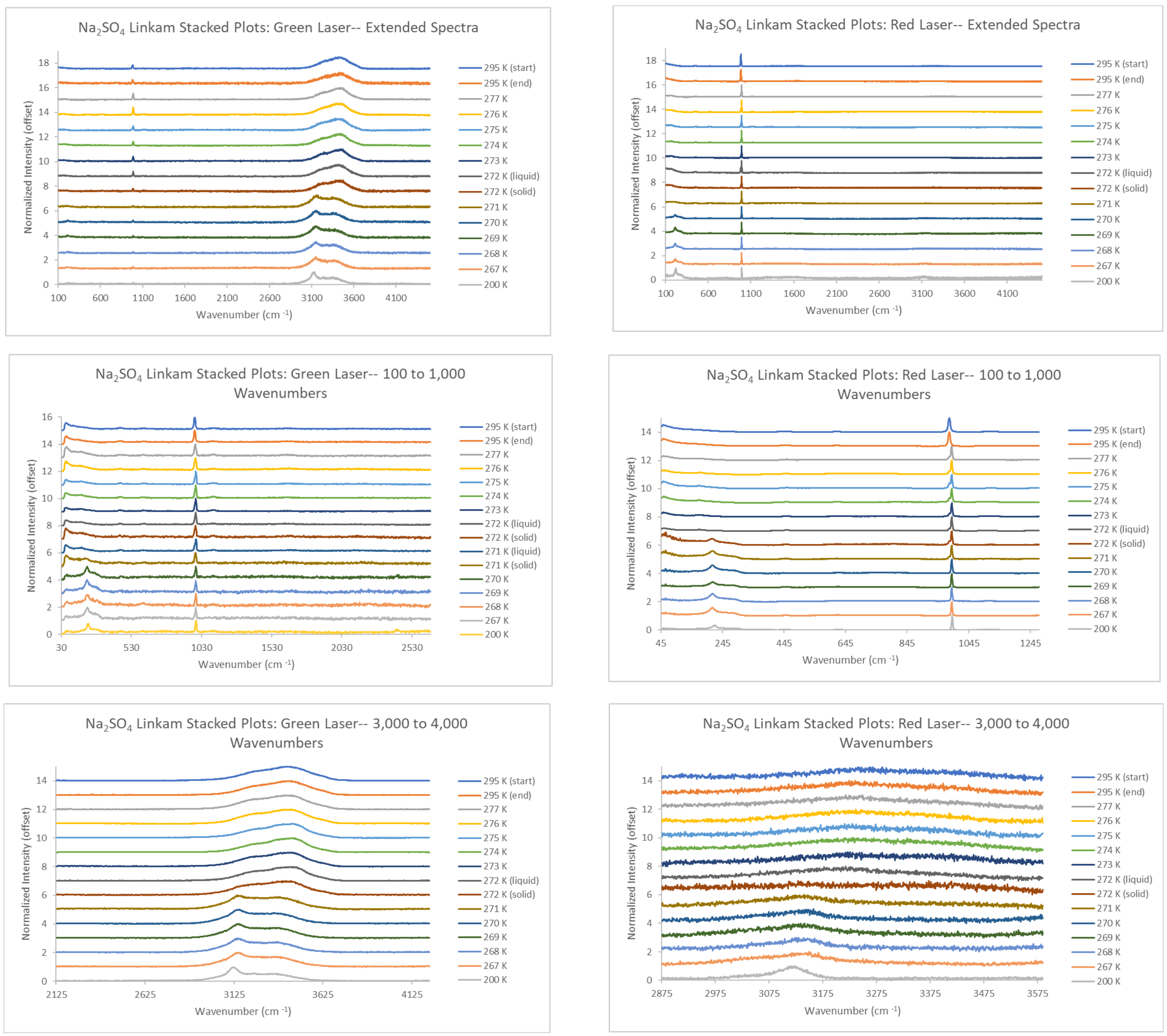

Figure A14: Na_2SO_4 stacked plots (532 nm and 785 nm lasers), lines and labels not included.

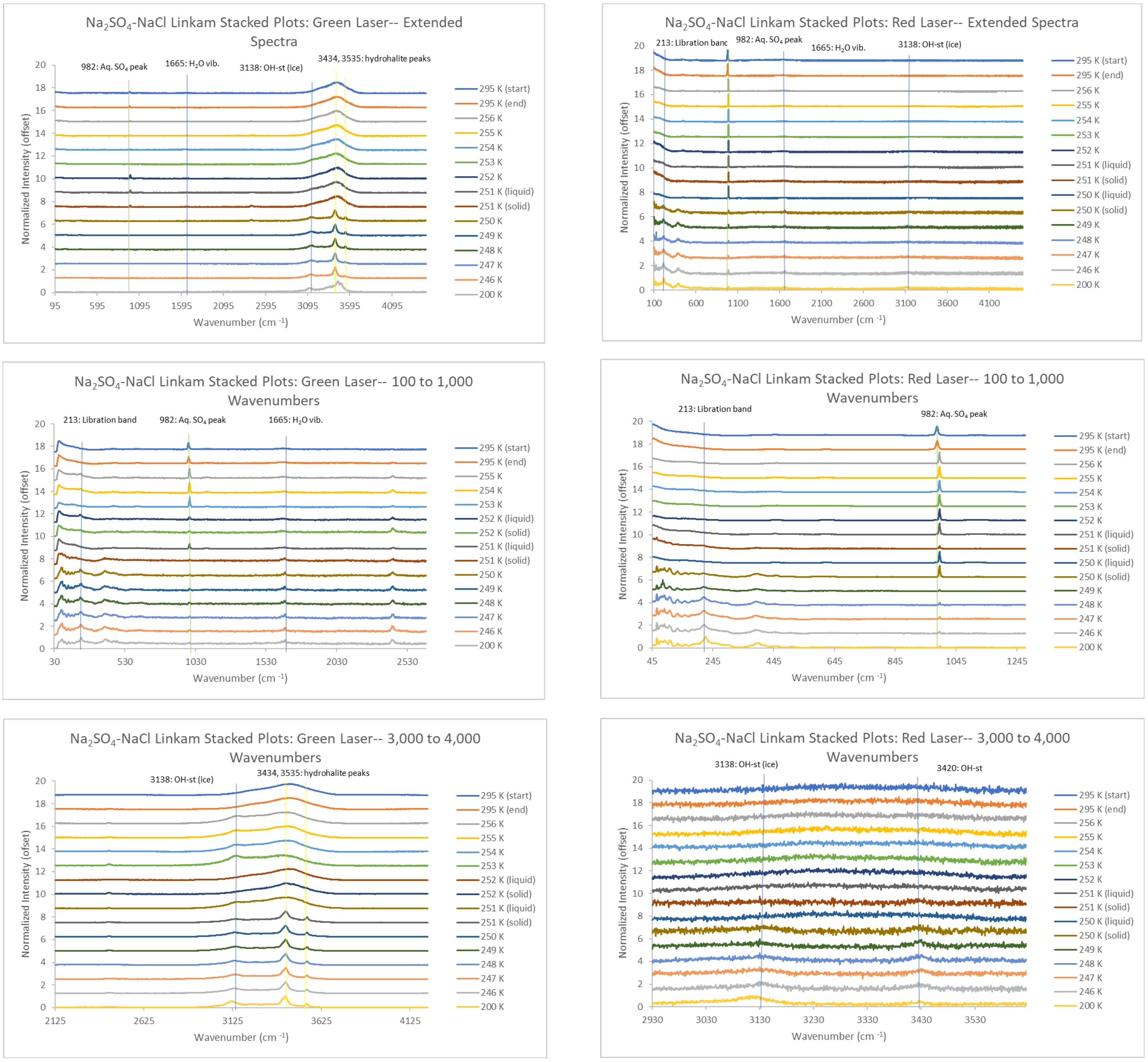

Figure A15: Na_2SO_4-NaCl stacked plots (532 nm and 785 nm lasers), lines and labels included to denote important peaks of ultrapure water (light blue), Na_2SO_4 (light green), and NaCl (yellow).

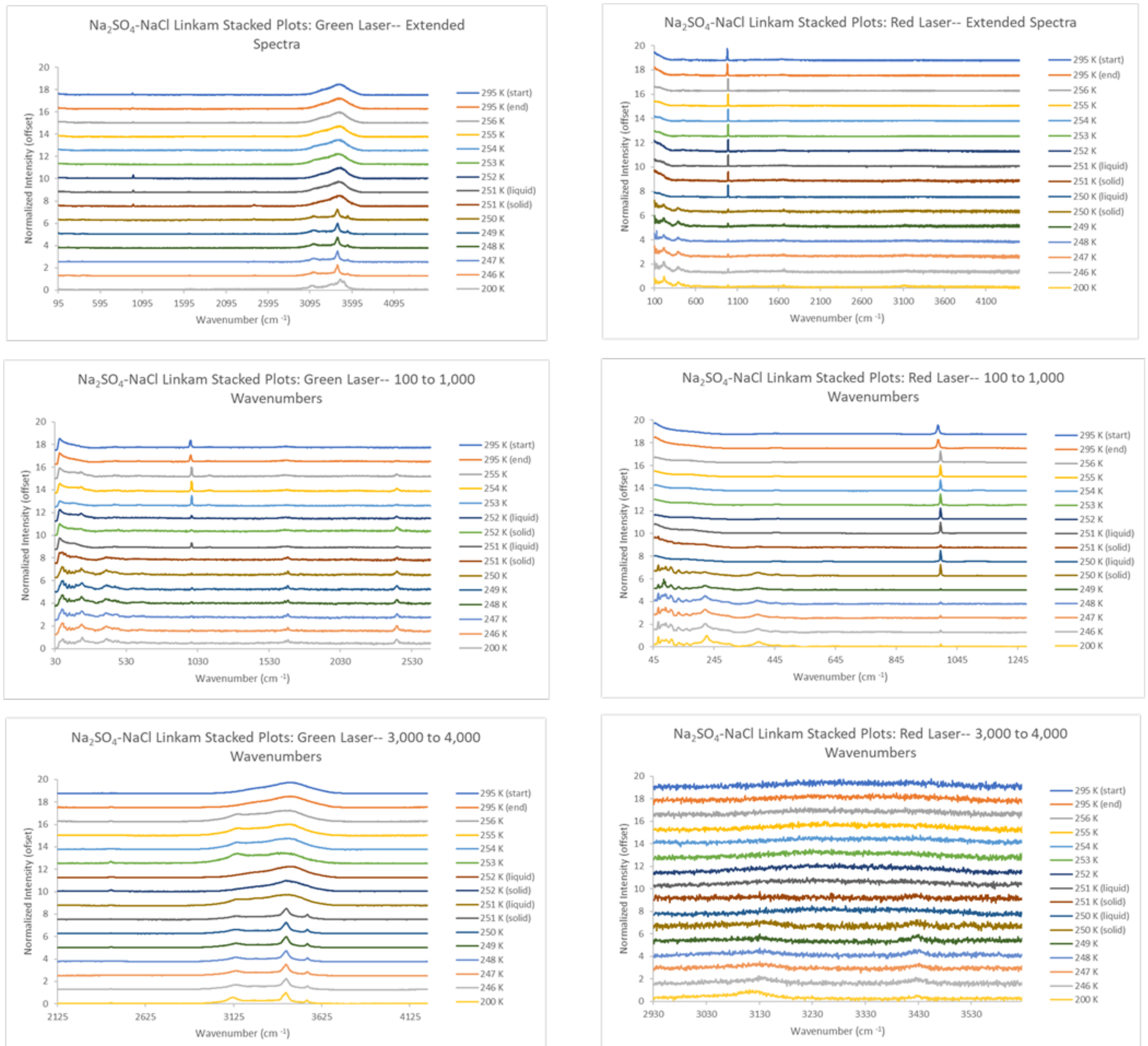

Figure A16: Na_2SO_4-NaCl stacked plots (532 nm and 785 nm lasers), lines and labels not included.

Figure A17: Na_2SO_4-$NaClO_4$ stacked plots (532 nm and 785 nm lasers), lines and labels included to denote important peaks of ultrapure water (light blue), Na_2SO_4 (light green) and $NaClO_4$ (red).

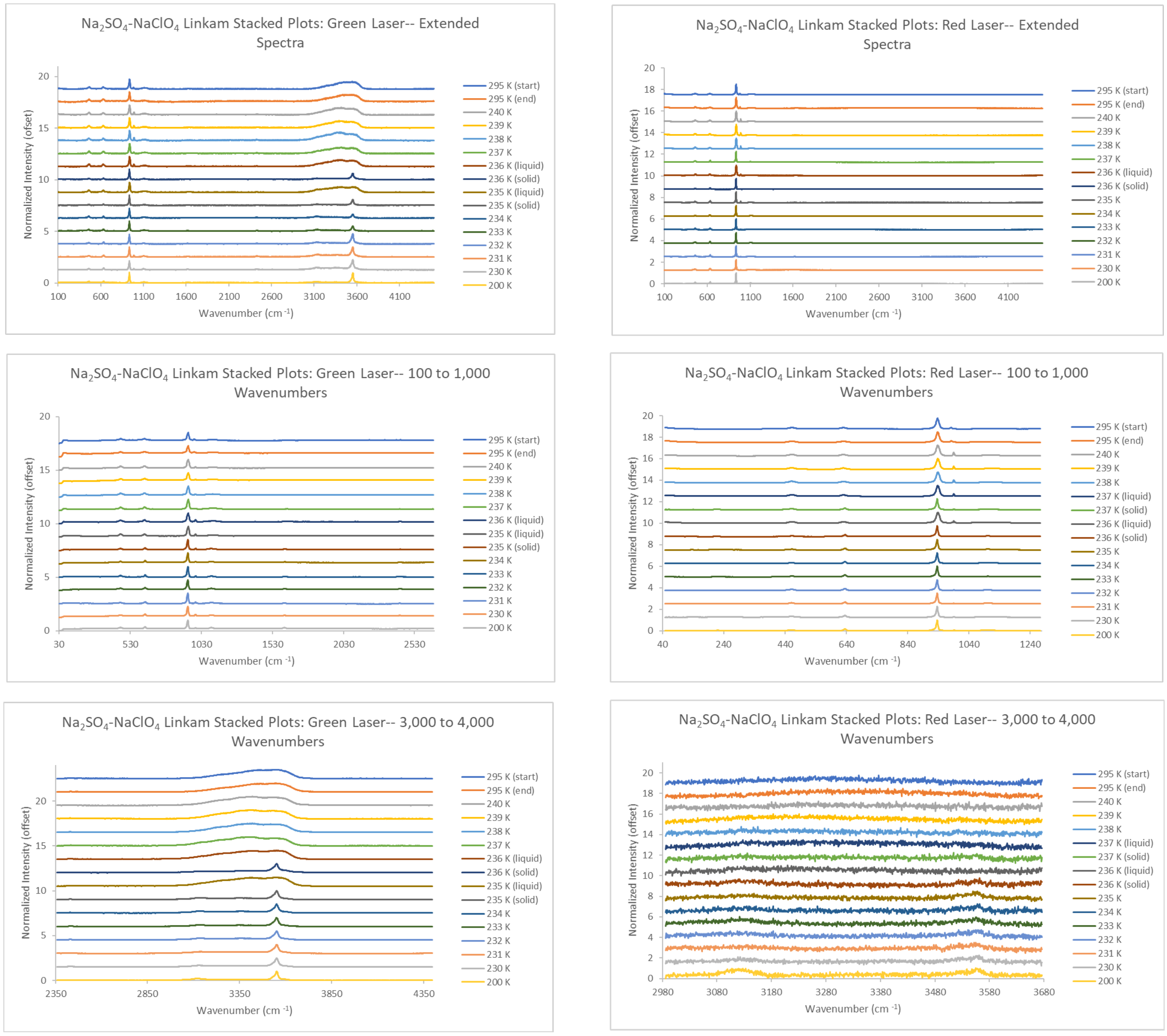

Figure A18: Na_2SO_4-$NaClO_4$ stacked plots (532 nm and 785 nm lasers), lines and labels not included.

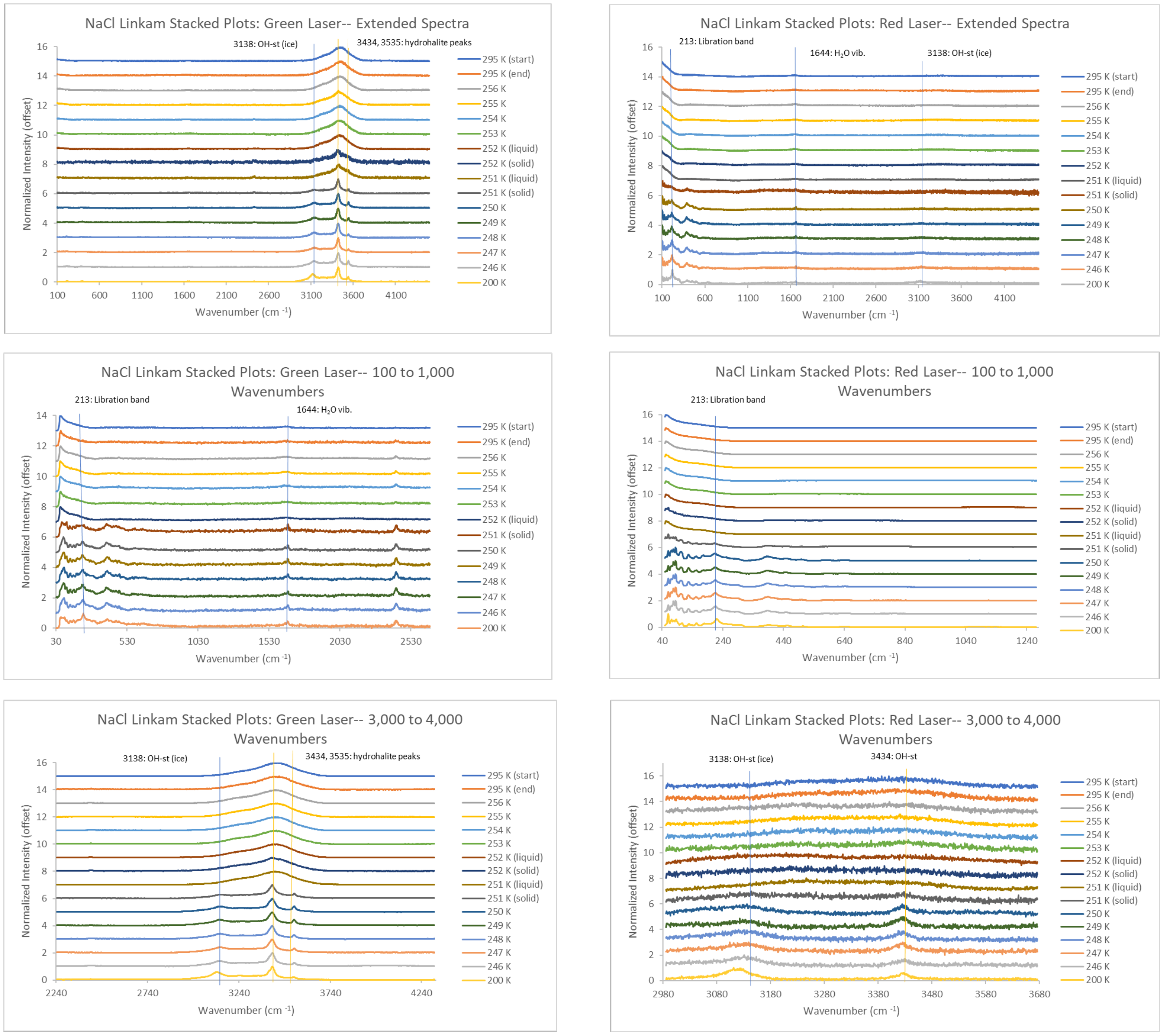

Figure A19: NaCl stacked plots (532 nm and 785 nm lasers), lines and labels included to denote important peaks of both ultrapure water (light blue) and NaCl (yellow).

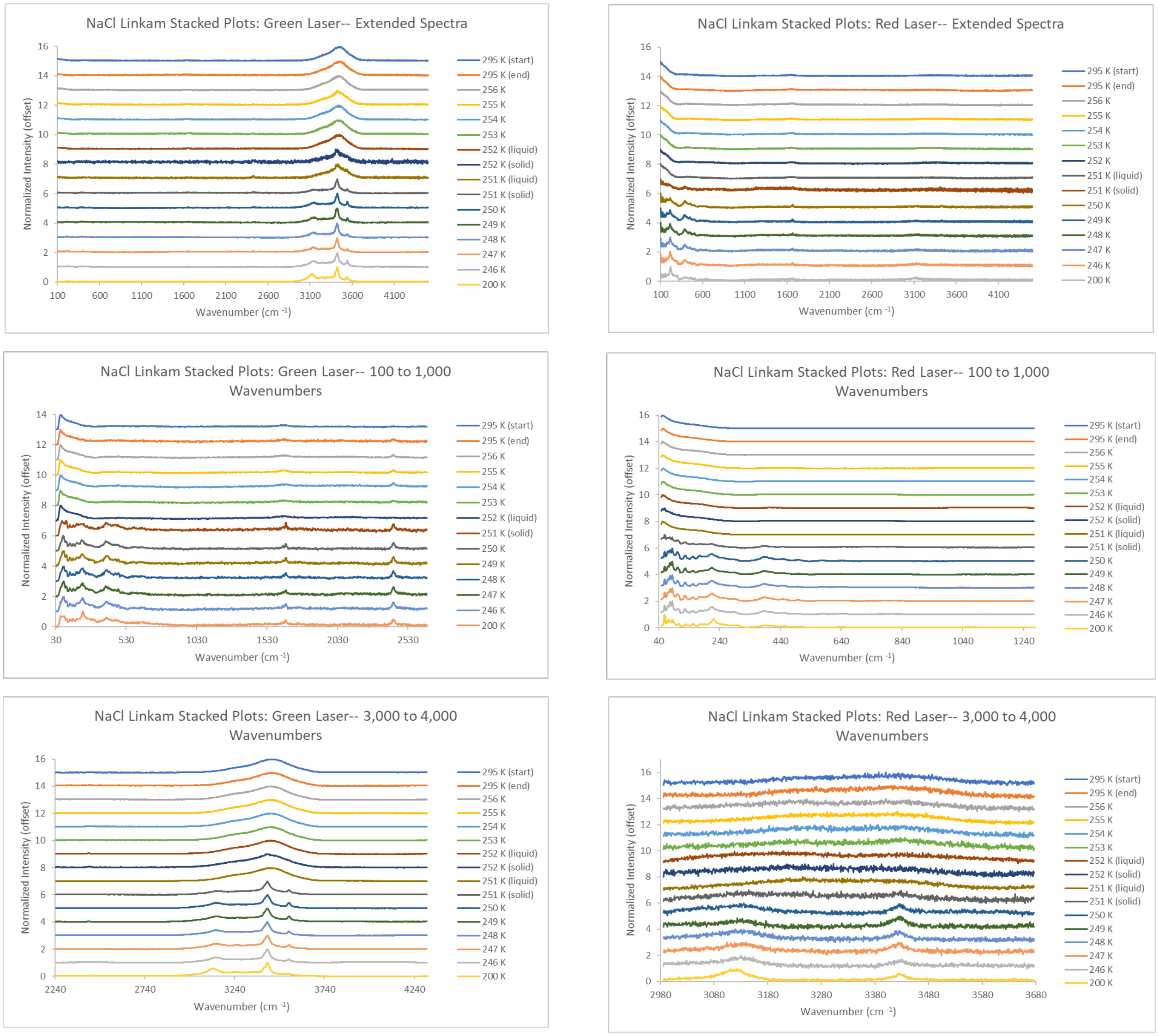

Figure A20: NaCl stacked plots (532 nm and 785 nm lasers), lines and labels not included.

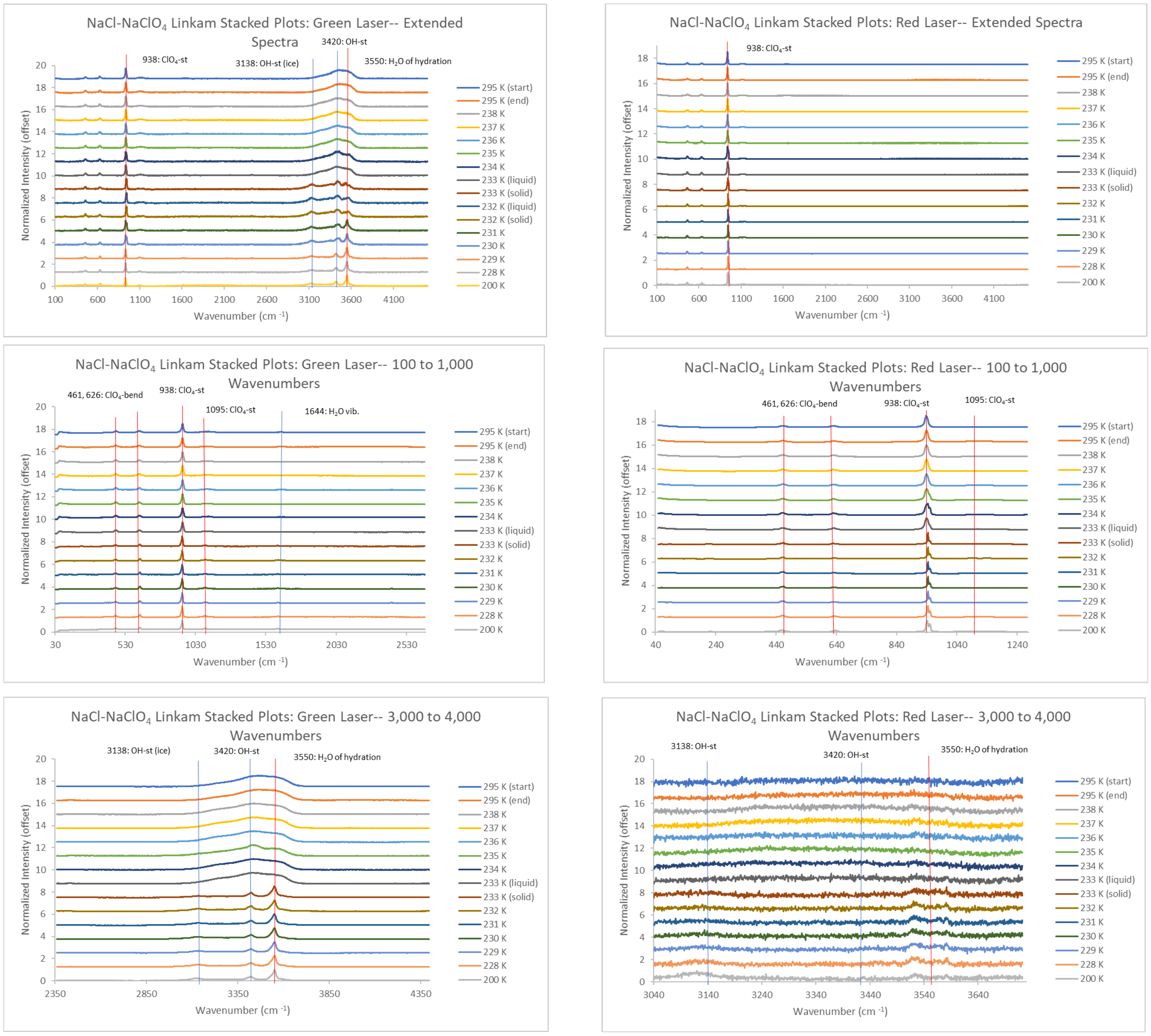

Figure A21: NaCl-NaClO$_4$ stacked plots (532 nm and 785 nm lasers), lines and labels included to denote important peaks of ultrapure water (light blue), NaCl (yellow), and NaClO$_4$ (red).

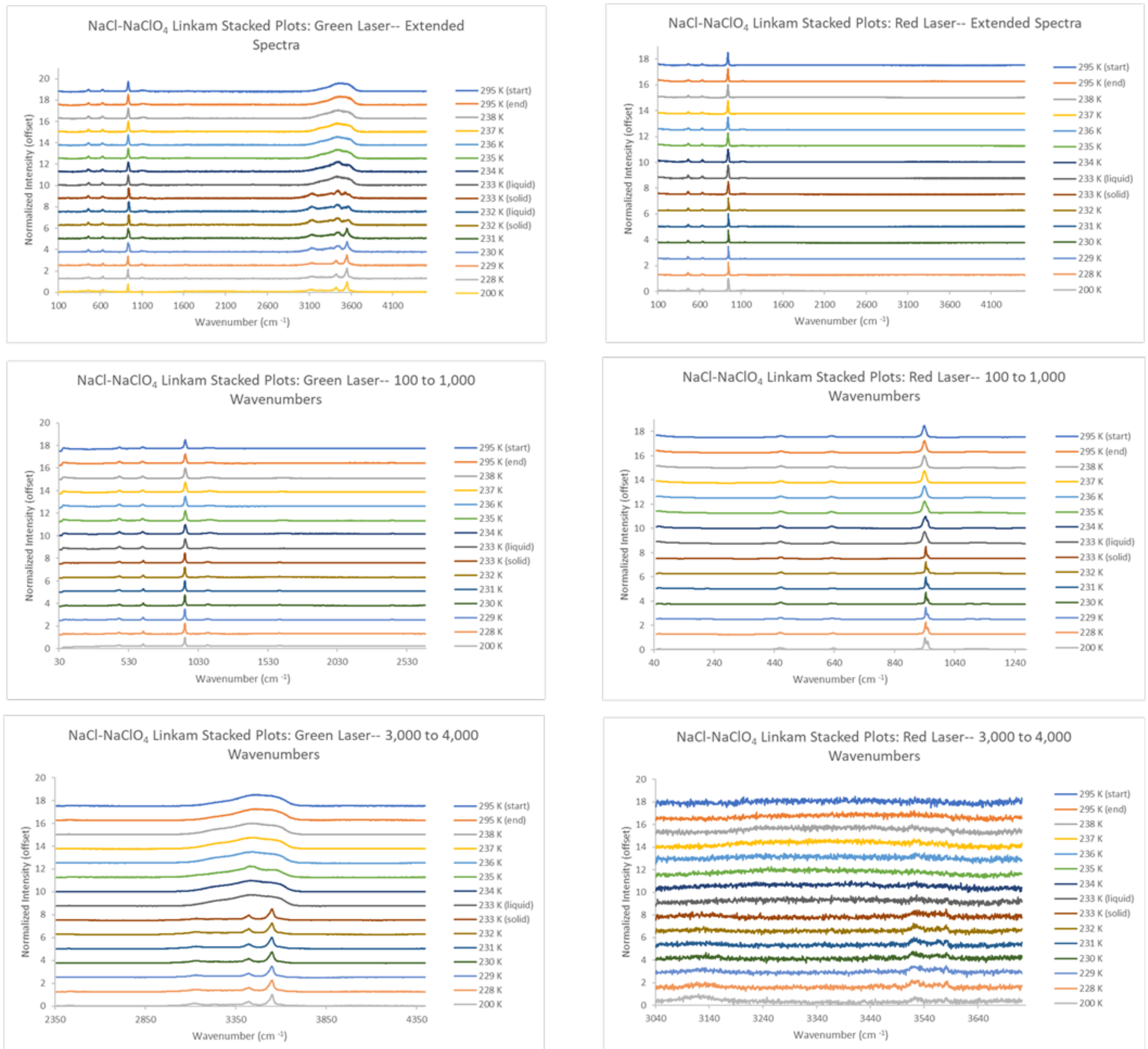

Figure A22: NaCl-NaClO$_4$ stacked plots (532 nm and 785 nm lasers), lines and labels not included.

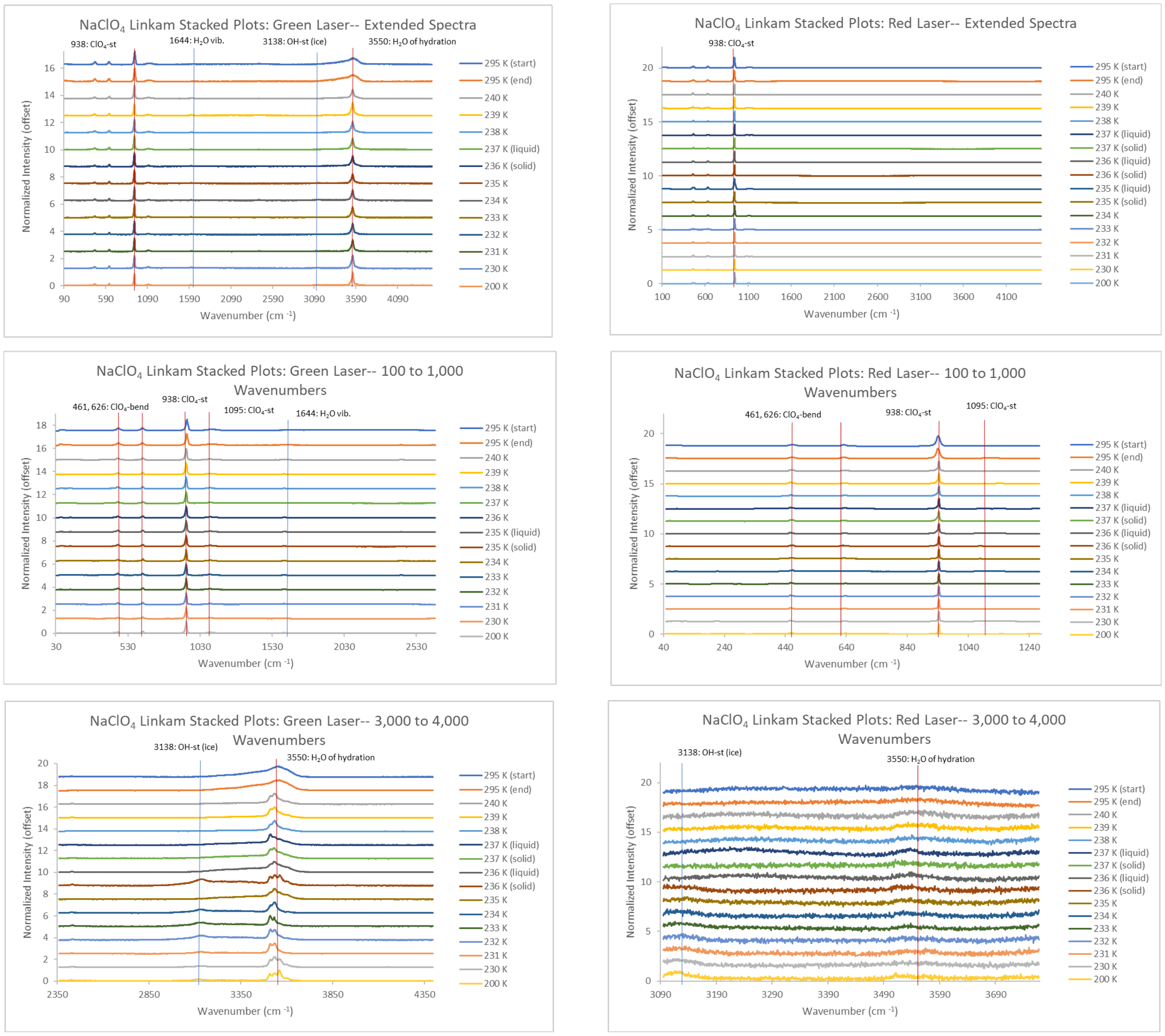

Figure A23: $NaClO_4$ stacked plots (532 nm and 785 nm lasers), lines and labels included to denote important peaks of ultrapure water (light blue) and $NaClO_4$ (red)

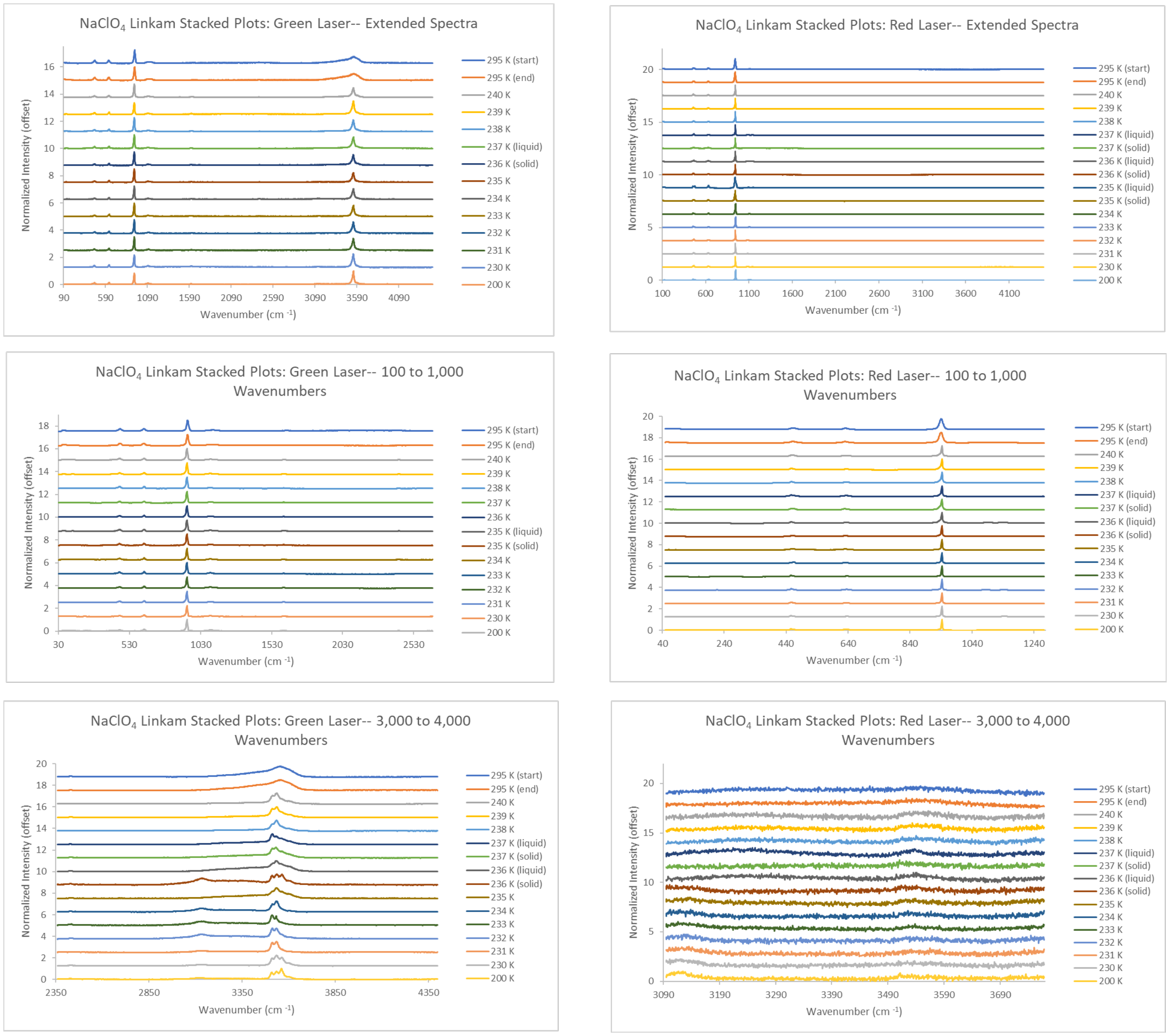

Figure A24: $NaClO_4$ stacked plots (532 nm and 785 nm lasers), lines and labels not included.

Component Comparison Graphs:

The following five figures showcase a comparison between the mixed brines and their respective endmembers, at both 295 K and 200 K.

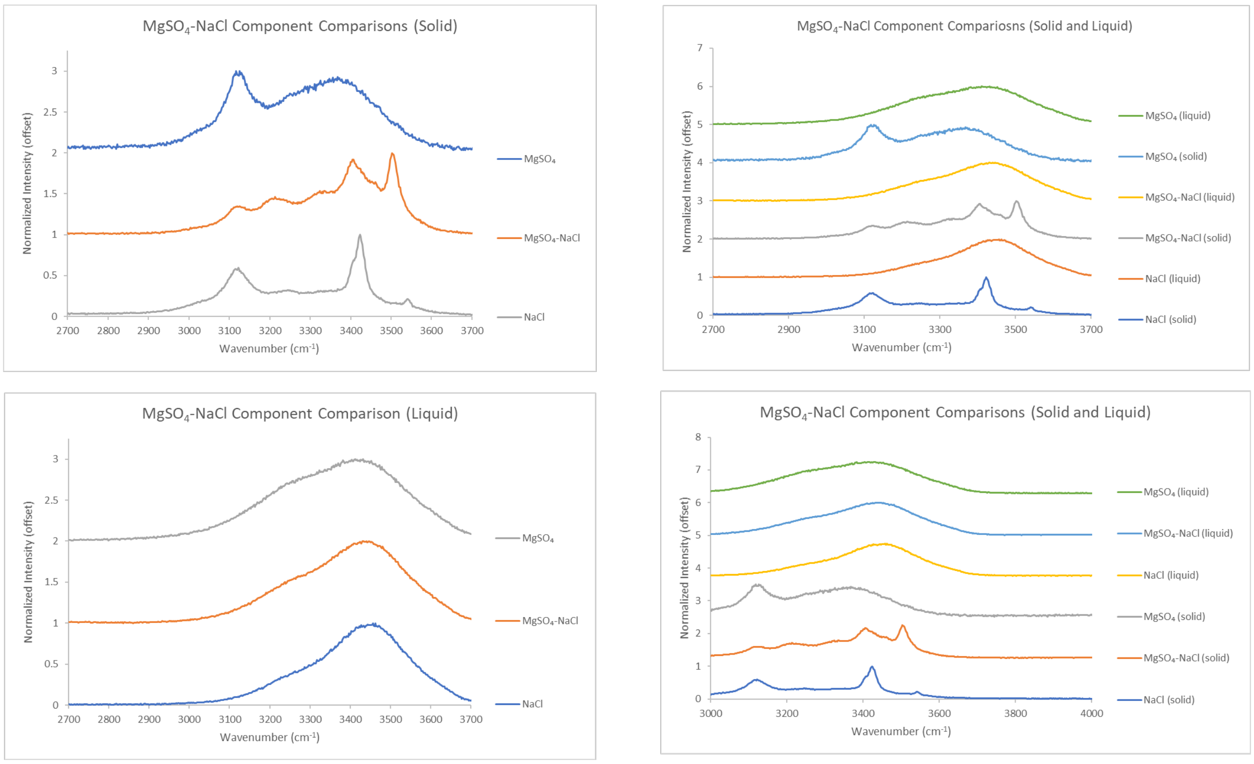

Figure A25: MgSO4-NaCl comparison stacked plots between solid (200 K) and liquid (295 K) components of both endmembers and their respective mixed brine using the 532 nm green laser.

Figure A26: $MgSO_4$-$NaClO_4$ comparison stacked plots between solid (200 K) and liquid (295 K) components of both endmembers and their respective mixed brine using the 532 nm green laser.

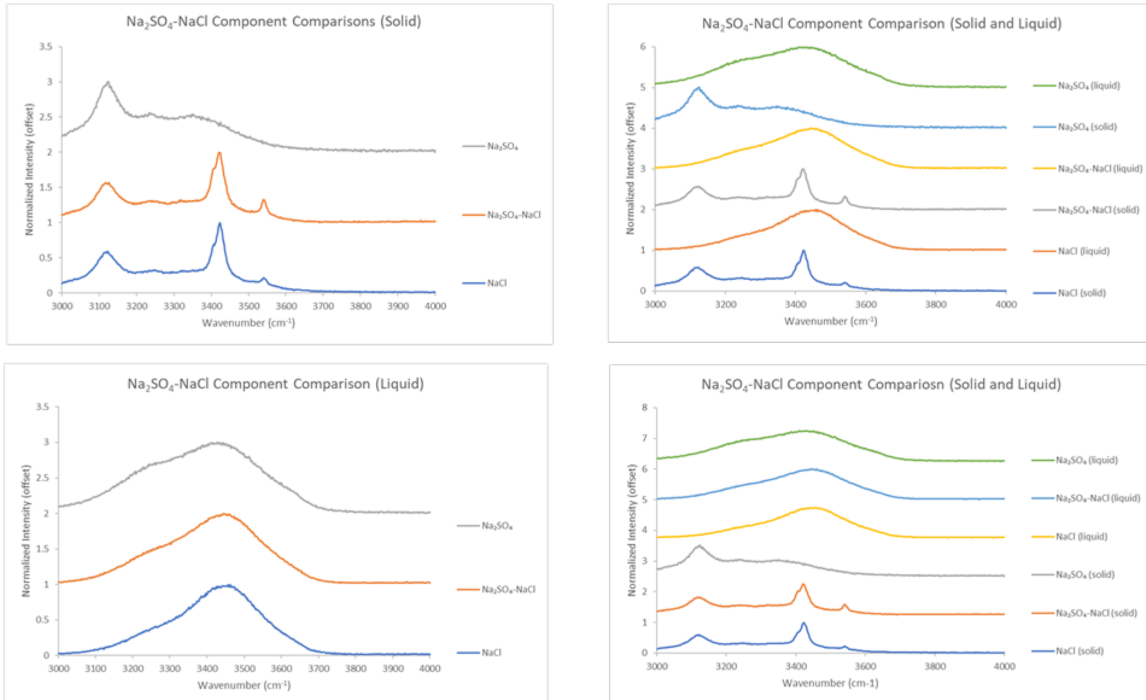

Figure A27: Na_2SO_4-NaCl comparison stacked plots between solid (200 K) and liquid (295 K) components of both endmembers and their respective mixed brine using the 532 nm green laser.

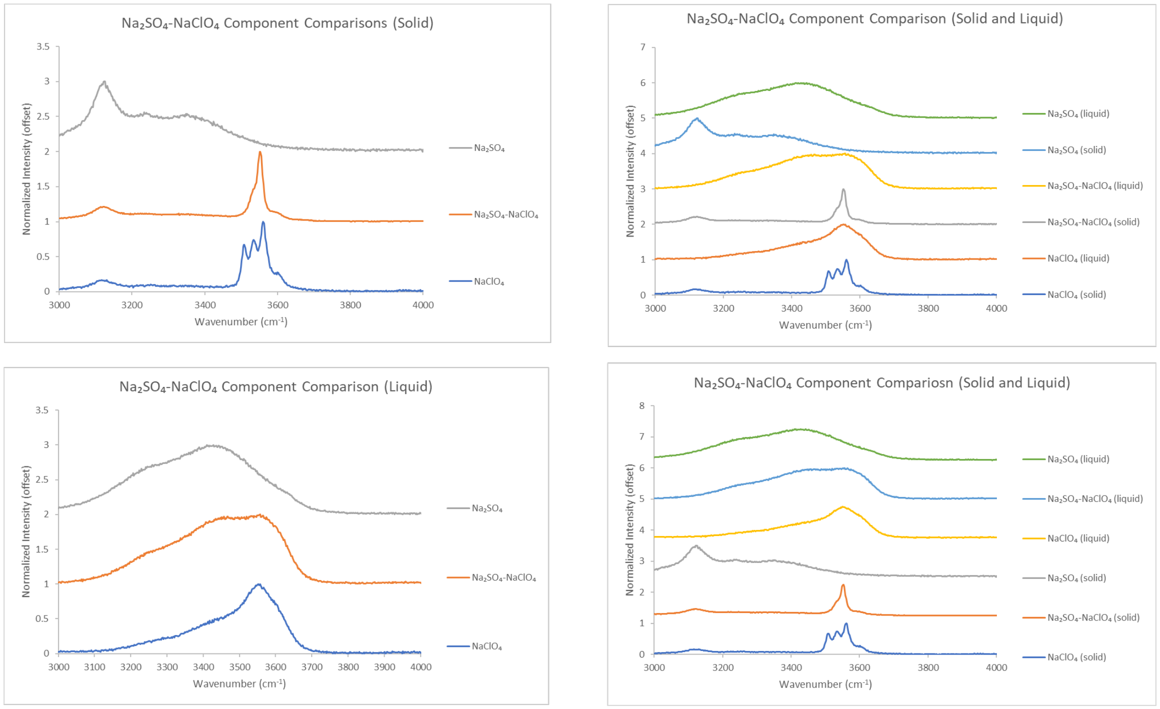

Figure A28: Na_2SO_4-$NaClO_4$ comparison stacked plots between solid (200 K) and liquid (295 K) components of both endmembers and their respective mixed brine using the 532 nm green laser.

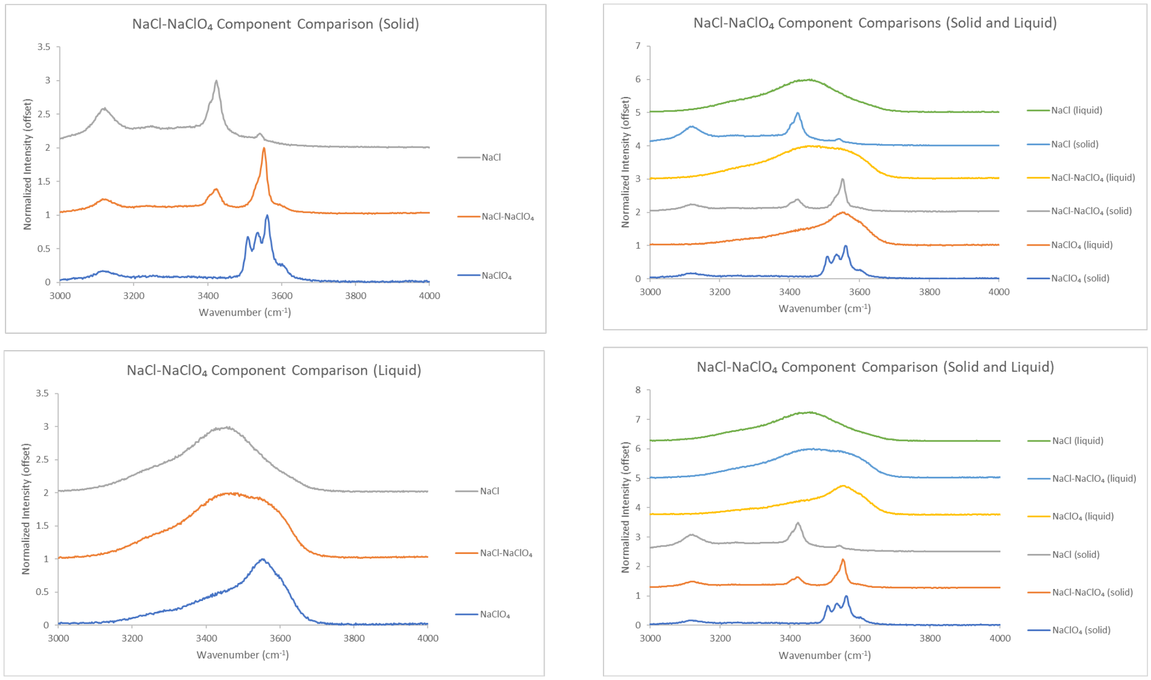

Figure A29: NaCl-NaClO$_4$ comparison stacked plots between solid (200 K) and liquid (295 K) components of both endmembers and their respective mixed brine using the 532 nm green laser.

Sulfate and Perchlorate Peak Centre Comparison:

The following nine figures denote changes in either the sulfate or perchlorate peak positions as a function of temperature using both the 532 nm (green) and 785 nm (red) lasers. Peak positions have been shown through experimentation to be repeatable.

Figure A30: The peak position of the main sulfate peak for magnesium sulfate using both the 532 nm and 785 nm lasers. Note that plots denoting falling temperatures are denoted by dashed lines, while rising temperatures are denoted by solid lines.

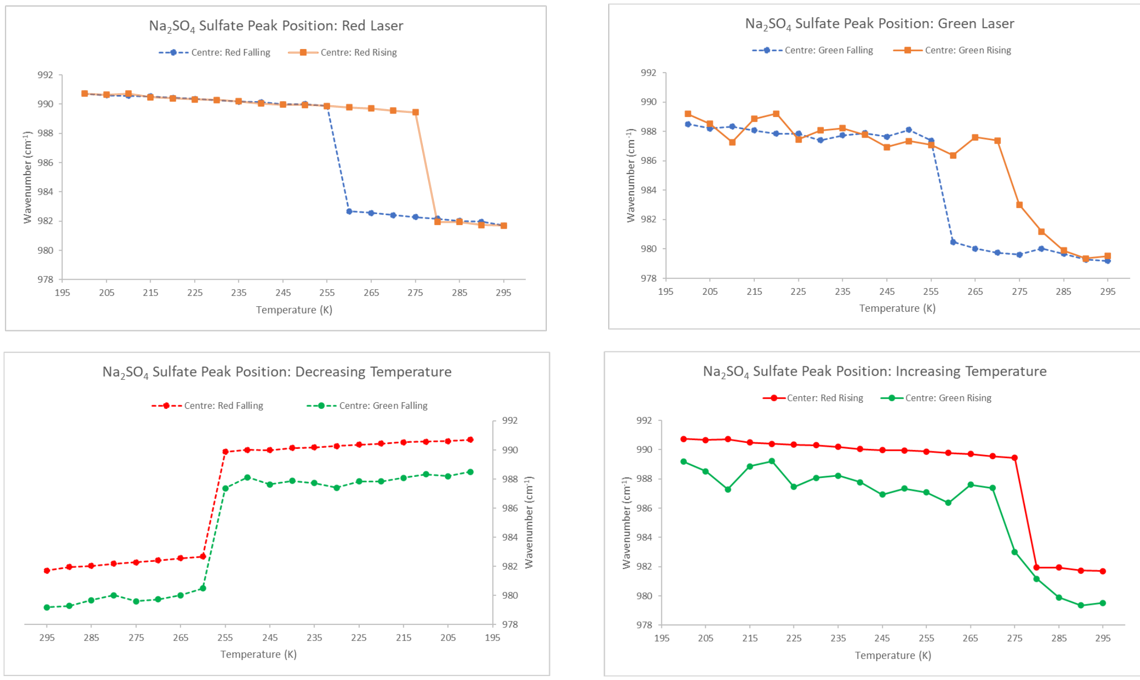

Figure A31: The peak position of the main sulfate peak for sodium sulfate using both the 532 nm and 785 nm lasers. Note that plots denoting falling temperatures are denoted by dashed lines, while rising temperatures are denoted by solid lines.

Figure A32: The peak position of the main perchlorate peak for sodium perchlorate using both the 532 nm and 785 nm lasers. Note that plots denoting falling temperatures are denoted by dashed lines, while rising temperatures are denoted by solid lines.

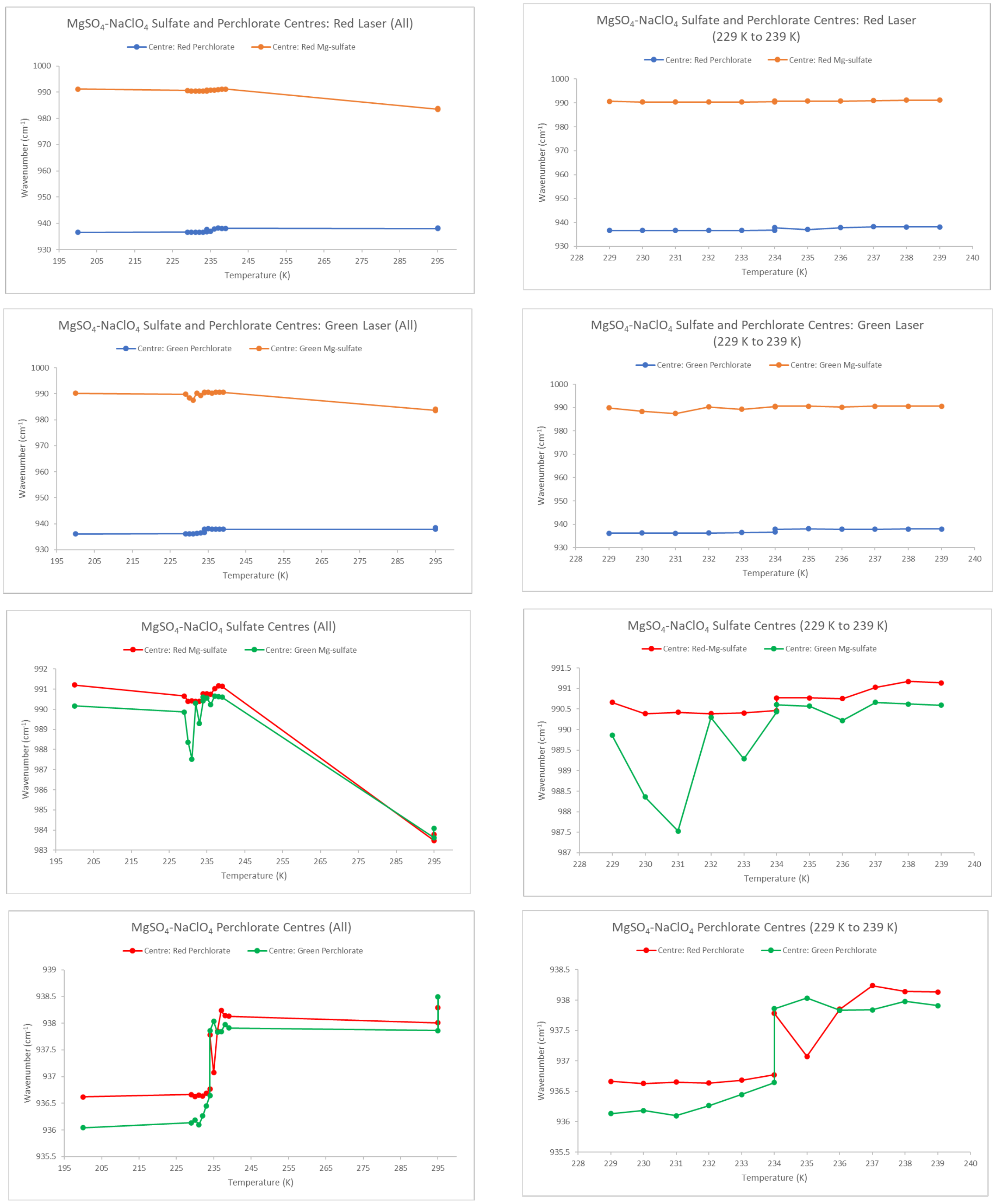

Figure A33: The peak positions of the main sulfate and perchlorate peaks for the $MgSO_4$-$NaClO_4$ brine using both the 532 nm and 785 nm lasers.

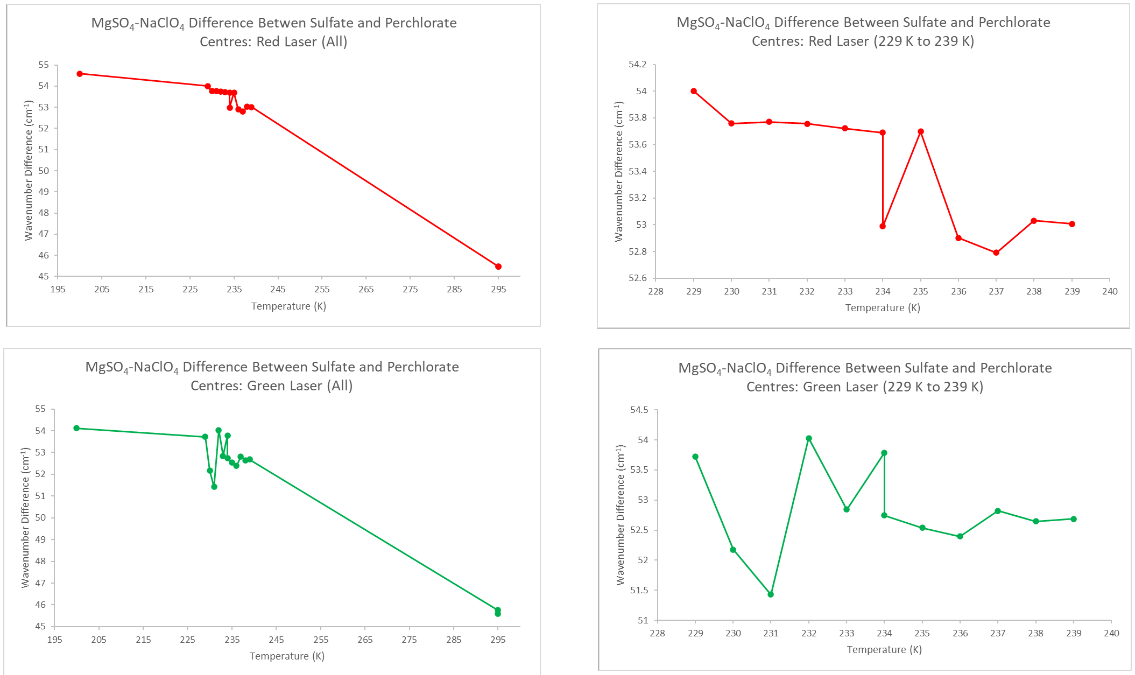

Figure A34: The difference in peak positions between the main sulfate and perchlorate peaks for the $MgSO_4$-$NaClO_4$ brine using both the 532 nm and 785 nm lasers.

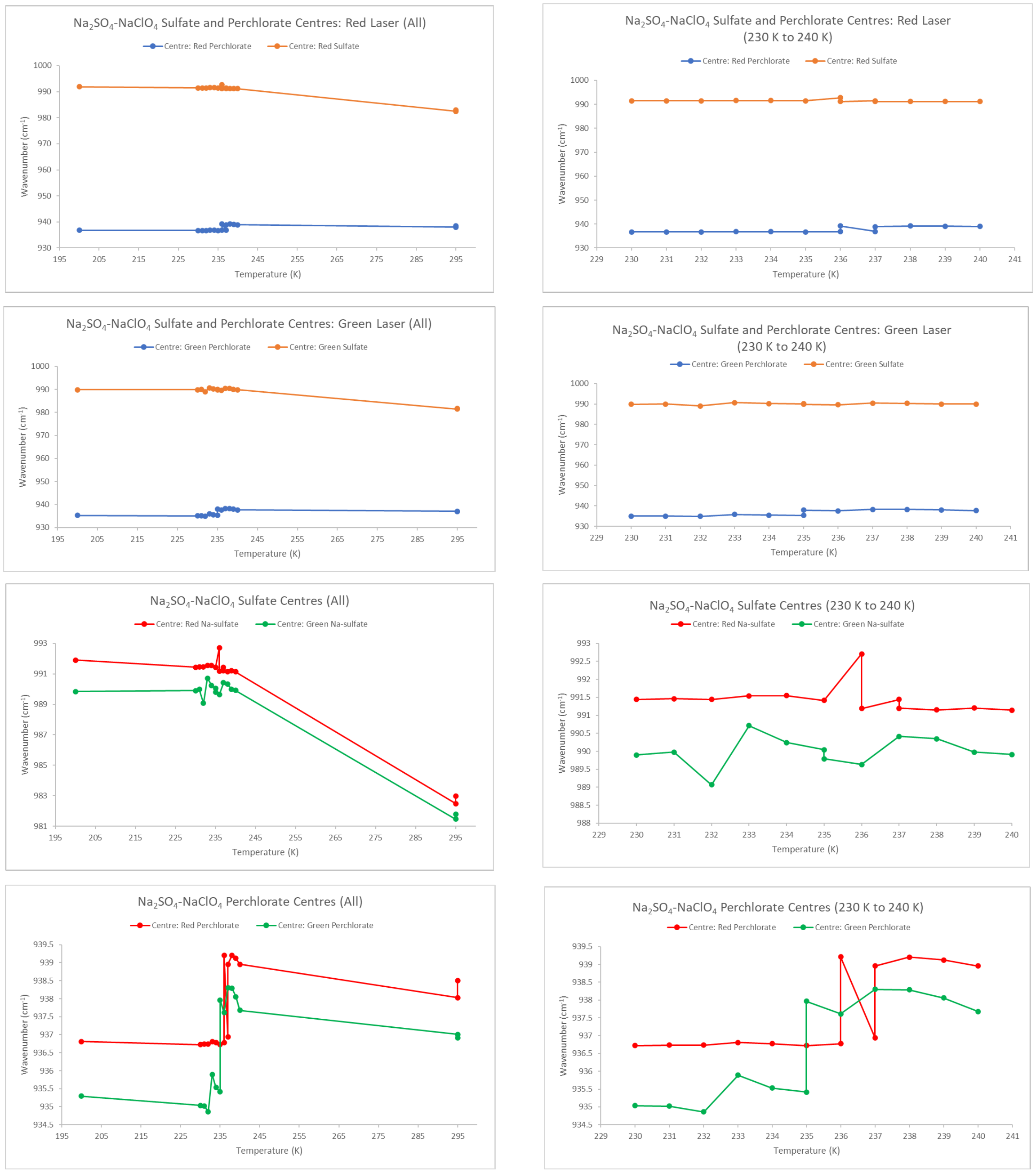

Figure A35: The peak positions of the main sulfate and perchlorate peaks for the Na_2SO_4-$NaClO_4$ brine using both the 532 nm and 785 nm lasers.

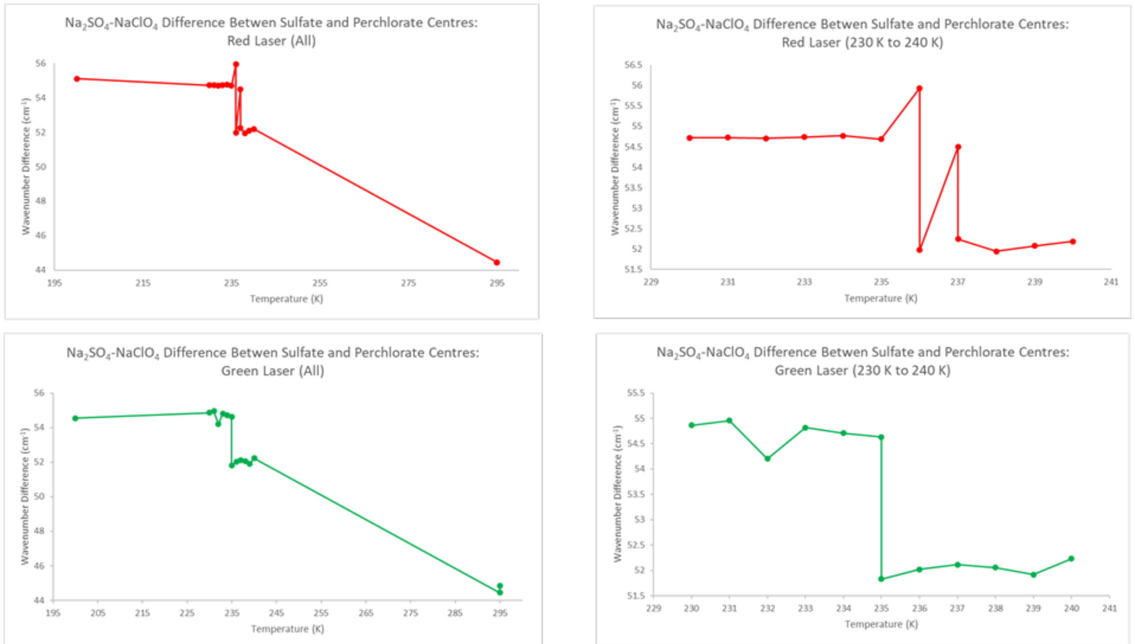

Figure A36: The difference in peak positions between the main sulfate and perchlorate peaks for the Na_2SO_4-$NaClO_4$ brine using both the 532 nm and 785 nm lasers.

Figure A37: The peak position of the main sulfate peak for four sulfate brines using both the 532 nm and 785 nm lasers. Note that plots denoting falling temperatures are denoted by dashed lines, while rising temperatures are denoted by solid lines.

Figure A38: The peak position of the main perchlorate peak for three perchlorate brines using both the 532 nm and 785 nm lasers. Note that plots denoting falling temperatures are denoted by dashed lines, while rising temperatures are denoted by solid lines.

Additional References Cited Only in Supplementary Materials:

Berg R.W., Raman detection of hydrohalite formation: avoiding accidents on icy roads by deicing where salt will not work Appl. Spectrosc. Rev. 2018 503-515

Narayanaswamy P.K., The Raman Spectra of water, 1948